

Doctoral Thesis

---

# **mechanics of epithelial tissue subjected to controlled pressure**



**Nimesh R. Chahare  
Barcelona, April 2023**



---

DOCTORAL PROGRAM IN APPLIED MATHEMATICS  
UNIVERSITAT POLITÈCNICA DE CATALUNYA

MECHANICS OF EPITHELIAL TISSUE SUBJECTED TO  
CONTROLLED PRESSURE

by

NIMESH RAMESH CHAHARE



LACÀN: LABORATORY OF MATHEMATICAL  
AND COMPUTATIONAL MODELING

ADVISORS: MARINO ARROYO AND XAVIER TREPAT  
BARCELONA, APRIL 03, 2023



Dedicated to the city of Barcelona,

A city that has captured my heart and soul with its vibrant culture, breathtaking architecture, and warm people. Barcelona has been the fertile ground in which my ideas have taken root and blossomed during my doctoral journey, as the world grapples with crises and chaos. I am deeply grateful for the opportunities and experiences this magnificent city has provided me.

In homage to Barcelona, I have chosen to adorn this thesis with a cover design that merges Gaudí's trencadís technique and epithelial domes, symbolizing not only my love for this city but also my fascination with the intricacies of nature and the wonders of biological systems.

Moltes Gràcies, Barcelona.



“You cannot carry out fundamental change without a certain amount of madness. In this case, it comes from nonconformity, the courage to turn your back on the old formulas, the courage to **invent the future**. It took the mad people of yesterday for us to be able to act with extreme clarity today. I want to be one of those people.”

Thomas Sankara



## ABSTRACT

Mechanics of epithelial tissue subjected to controlled pressure

Nimesh Ramesh Chahare

Epithelial sheets form specialized 3D structures suited to their physiological roles, such as branched alveoli in the lungs, tubes in the kidney, and villi in the intestine. To generate and maintain these structures, epithelia must undergo complex 3D deformations across length and time scales. How epithelial shape arises from active stresses, viscoelasticity, and luminal pressure remains poorly understood. To address this question, we developed a microfluidic chip and a computational framework to engineer 3D epithelial tissues with controlled shape and pressure. In the setup, an epithelial monolayer is grown on a porous surface with circular low adhesion zones. On applying hydrostatic pressure, the monolayer delaminates into a spherical cap from the circular zone. This simple shape allows us to calculate epithelial tension using Laplace's law. Through this approach, we subject the monolayer to a range of lumen pressures at different rates and hence probe the relation between strain and tension in different regimes while computationally tracking actin dynamics and their mechanical effect at the tissue scale. Slow pressure changes relative to the actin dynamics allow the tissue to accommodate large strain variations. However, under sudden pressure reductions, the tissue develops buckling patterns and folds with different degrees of symmetry-breaking to store excess tissue area. These insights allow us to pattern epithelial folds through rationally directed buckling. Our study establishes a new approach for engineering epithelial morphogenetic events.

*Keywords:* epithelial monolayers, actomyosin cytoskeleton, morphogenesis, mechanobiology, microfluidics



## RESUM

Mechanics of epithelial tissue subjected to controlled pressure

Nimesh Ramesh Chahare

Les làmines epiteliales formen estructures 3D especialitzades adequades als seus rols fisiològics, com ara alvèols ramificats als pulmons, tubs al ronyó i vellositats a l'intestí. Per generar i mantenir aquestes estructures, els epitelis han de patir deformacions 3D complexes en longitud i temps. La manera en què la forma epitelial sorgeix de tensions actives, viscoelàsticitat i pressió luminal encara és poc entesa. Per abordar aquesta qüestió, hem desenvolupat un xip microfluídic i un marc computacional per dissenyar teixits epiteliais 3D amb forma i pressió controlades. En aquest sistema, una monocapa epitelial es cultiva sobre una superfície porosa amb zones circulars de baixa adhesió. En aplicar pressió hidrostàtica, la monocapa es delamina i forma una estructura esfèrica a la zona circular. Aquesta forma simple ens permet calcular la tensió epitelial utilitzant la llei de Laplace. A través d'aquest enfocament, sotmetem la monocapa a una gamma de pressions luminals a diferents velocitats i, per tant, sondegem la relació entre deformació i tensió en diferents règims mentre seguim computacionalment la dinàmica de l'actina i el seu efecte mecànic a escala de teixit. Canvis de pressió lents en relació amb la dinàmica de l'actina permeten que el teixit acomodi grans variacions de deformació. No obstant això, sota reduccions subtades de pressió, el teixit desenvolupa patrons de vinclament i plecs amb diferents graus de trencament de simetria per emmagatzemar l'àrea de teixit sobrant. Aquestes idees ens permeten modelar plecs epiteliais a través d'uns plegaments dirigits racionalment. El nostre estudi estableix una nova estratègia per dissenyar esdeveniments morfogenètics epiteliais.



## ACKNOWLEDGMENTS

First and foremost, I express my profound gratitude to my esteemed supervisors, Prof. Marino Arroyo and Prof. Xavier Trepat, for providing me with the incredible opportunity to embark on this PhD journey and encouraging me to pursue unconventional and fascinating scientific endeavors. Their invaluable guidance, support, and inspiring mentorship have been instrumental in shaping my research and fostering a spirit of curiosity and innovation.

I am deeply grateful to my family for their love, encouragement, and belief in my capabilities. My heartfelt thanks go to my parents and sister for their endless support and sacrifices. Special thanks to Shubham Pudke for critical mental support and the thesis cover.

My appreciation extends to my closest labmates, the MOLI team, whose camaraderie, collaboration, and intellectual exchange have greatly enriched my experience. I am especially grateful to Tom Golde, Thomas Wilson, and Özge Özguç for their invaluable insights, stimulating discussions, and unwavering assistance during countless hours of experimentation and data analysis. Before Tom joined the project, many things were going wrong. Ideas were present, but the execution and efficiency of experiments improved after he joined. Thomas has been instrumental in trying out new experimental setups and discovering new phenomena. I am truly grateful for having Thomas to discuss new ideas with.

I would like to express my gratitude to Adam Ouzeri. We have been in the same boat, so to speak, throughout the project. He struggled with digital domes while I tackled real ones. Both were challenging, but our lengthy discussions kept me grounded. Thank you, Adam. As well as I thank all the lab of Marino Arroyo for developing computational resources greatly useful in this thesis.

I would like to express my gratitude to all the staff at the IBEC microfabrication facility for providing support with fabrication. Sandra Segura has been instrumental in fabricating new molds for our microfluidic devices. As well as, my gratitude to PRIMO team, a lot of this project would not be possible without them, Dr. Raimon Sunyer and Isabela Fortunato.

The experimental work requires many people, most importantly technicians. Special thanks to Susana Usieto, Natalia Castro, Anghara Mendez, Monica Purciolas, and Oriol Mañé (my Catalan bro).

The microscope and data management team, which keeps the engines of confocal

imaging running, includes Víctor González-Tarragó, Leone Rossetti, Ion Andreu, Ariadna Marin, Ernest Latorre, Raimon Sunyer, Anabelise Le Roux, Amy Beedle, Marija Matejcic, Manuel Gómez, Elena Dalaka, Pau Guillamat, Miquel Pardos, Nacho Viciano, Tom Golde, and Thomas Wilson.

The cell culture team, responsible for maintaining the conditions that keep my cells alive, consists of Miguel González, Marc Molina, Gerardo Ceada, Jorge Oliver De La Cruz, Sefora Conti, Alice Perucca, Xarxa Quiroga, Anna Labernadie, and Isabela Fortunato. The protocol team and the antibody plasmid team include Aina Albajar, Ignasi Granero Moya, Juanfra Abenza, Mamatha Nijaguna, Ona Baguer, and Meng Wang.

Lastly, the most important team, the pipette team, comprises Srivatsava Viswanadha, Marina Pavlova-Deb, Marilena Naoum, Clément Hallopeau, and Eva Jou. I would also like to thank Zarina Nauryzgaliyeva for handling the schedules.

Another group of individuals who have enriched my PhD experience are the fellow students around me: Alexandre Garcia-Duran, Joan Triadú, Alexandra Mittens, Gavin McQuarrie, Kandela Ballerini, and Eva Jou.

I would also like to thank Prof. Pere Roca-Cusachs for giving me opportunity to collaborate on number of projects in his lab.

Thesis writing is difficult; but the quality of this document improved with support of MOLI team, Pau Guillamat, Ignasi Granero Moya, and Elena Dalaka. Even more difficult to do are the experiments, this is where friendships out of lab mattered a lot. I want to thank Manu Bera, Mohit Bera, Rohit Kosti, Shikhar Nilabh, and Chetan Deshmukh for engaging conversations and great company.

I would like to extend my heartfelt gratitude to the reviewers, Dr. Raimon Sunyer and Dr. Alejandro Torres-Sánchez, for dedicating their time and providing valuable insights. Additionally, I am deeply appreciative of the examination committee members - Dr. Vikas Trivedi, Dr. José Muñoz, Dr. Magali Suzanne, Dr. David Oriola, and Dr. Raimon Sunyer - for graciously accepting the invitation to participate in my thesis defense.

I extend my gratitude to the Spanish and European governmental grant agencies for providing the funding that made this work possible. I am grateful to the staff at Universitat Politècnica de Catalunya and IBEC for their support. Additionally, I acknowledge the diverse contributions of working people worldwide, from Barcelona's bakers to Pakistani rice farmers, from Congolese miners to Chinese tech workers, their collective efforts have enabled the exchange of knowledge, goods, and services

essential for this work. I am grateful for these unsung heroes of labor, who remind us of the broader context of our academic pursuits and our responsibility to contribute to society and the global community.

Moreover, I acknowledge that this thesis would not have been possible without the support and encouragement of all the people mentioned above, as well as many others who have been part of my journey. I cannot possibly capture everything in these couple of pages. The people with whom I've had fun, engaged in discussions, and formed personal connections will remain with me forever.

Lastly, on a personal note, I extend my deepest appreciation to my partner, Judith Cantó, for her unwavering support, encouragement, and understanding throughout this journey. Her patience, care, and belief in me have been a source of strength and inspiration.

In conclusion, I am forever indebted to the people, and I hope that the knowledge gained through this research would be useful to somebody in the future.



# Contents

<b>Abstract</b>	i
<b>Acknowledgments</b>	v
<b>Contents</b>	ix
<b>List of Figures</b>	xiii
<b>I Introduction and motivation</b>	1
<b>1 Epithelial Layers</b>	3
1.1 Introduction . . . . .	3
1.2 Key components . . . . .	4
1.2.1 Cell structure . . . . .	4
1.2.2 Microenvironment . . . . .	6
1.2.3 Cell-Matrix interaction . . . . .	7
1.3 Forms of epithelia . . . . .	8
<b>2 The mechanical basis of Morphogenesis</b>	11
2.1 The complexity of the morphogenesis . . . . .	11
2.2 On growth and form . . . . .	12
2.3 Mechanobiology . . . . .	15
2.3.1 Synthetic substrates . . . . .	16
2.3.2 Geometric control . . . . .	17
2.3.3 Mechanical control . . . . .	18
2.3.4 3D systems . . . . .	20
<b>3 Active tissue mechanics</b>	23
3.1 Force generation with actin . . . . .	23
3.1.1 Actin filaments . . . . .	23
3.1.2 Actin networks . . . . .	24

3.1.3	Actin cortex . . . . .	26
3.2	Actin structures at a larger scale . . . . .	26
3.3	Timescales of the actin cytoskeleton . . . . .	29
3.4	Modeling active tissue dynamics . . . . .	30
3.4.1	Vertex models . . . . .	30
3.4.2	Continuum models . . . . .	32
3.4.3	Active surface models . . . . .	35
<b>4</b>	<b>Bottom up morphogenesis</b>	<b>39</b>
4.1	Learn by building . . . . .	39
4.2	How to build tissue structures? . . . . .	41
4.2.1	Controlling geometry and physical forces . . . . .	41
4.2.2	Manipulating biochemical signaling . . . . .	43
4.2.3	Exploiting mechanical instabilities . . . . .	44
4.3	Tissue hydraulics . . . . .	49
4.3.1	Hydraulic control of morphogenesis . . . . .	49
4.3.2	Mechanics of domes . . . . .	51
4.4	What is to be done? . . . . .	55
<b>5</b>	<b>Structure of the thesis</b>	<b>57</b>
5.1	Objectives . . . . .	57
5.2	Thesis outline . . . . .	57
<b>II</b>	<b>Results</b>	<b>59</b>
<b>6</b>	<b>A microfluidic device for generating 3D epithelia</b>	<b>61</b>
6.1	Introduction . . . . .	61
6.2	Monolayer Inflator . . . . .	62
6.3	Fabrication of the device . . . . .	63
6.4	Protein patterning and "upside-down" cell culture . . . . .	65
6.5	Pressure control . . . . .	67
6.6	Imaging the epithelial domes . . . . .	69
6.7	Light-sheet MOLI . . . . .	71
6.8	Summary and Discussion . . . . .	72
<b>7</b>	<b>Dynamic material response of epithelial domes</b>	<b>75</b>
7.1	Introduction . . . . .	75
7.2	Measurement of dome mechanics . . . . .	75
7.3	Epithelial domes at constant pressure . . . . .	77
7.4	Steady-state constitutive relation of epithelia . . . . .	80

7.5	Dynamics of the epithelial domes . . . . .	81
7.6	Active gel tissue model . . . . .	83
7.7	Active viscoelasticity of the epithelia . . . . .	86
7.8	Summary and Discussion . . . . .	90
<b>8</b>	<b>Epithelial Buckling: Transforming Domes into Folds</b>	<b>93</b>
8.1	Introduction . . . . .	93
8.2	Rapid deflation produces a buckling instability . . . . .	93
8.3	Multiscale buckling . . . . .	98
8.4	Generating epithelial folds . . . . .	100
8.5	Forming predictable folds . . . . .	102
8.6	Summary and Discussion . . . . .	104
<b>9</b>	<b>Conclusions and Future Perspectives</b>	<b>107</b>
9.1	Conclusions . . . . .	107
9.2	Future Perspectives . . . . .	109
<b>III</b>	<b>Appendices</b>	<b>111</b>
<b>A</b>	<b>Methods and Materials</b>	<b>113</b>
A.1	Fabrication of microfluidic devices . . . . .	113
A.2	Patterning protein on the device . . . . .	114
A.3	Cell culture in the device . . . . .	115
A.4	Staining actin with SPY-actin . . . . .	115
A.5	Fabrication method for the Light-Sheet MOLI device . . . . .	115
A.6	Device protein patterning and cell culture in Light-Sheet device . . . . .	116
A.7	Application and measurement of the pressure . . . . .	116
A.8	Confocal Microscopy . . . . .	117
A.9	Light-sheet microscopy . . . . .	117
A.10	Quantification of the dome areal strain and tension . . . . .	117
A.11	Analysis of the kymographs . . . . .	118
A.12	Qualitative analysis of the buckling event . . . . .	118
<b>B</b>	<b>MOLI Protocol</b>	<b>121</b>
B.1	Device Fabrication . . . . .	121
B.1.1	Main Block Fabrication . . . . .	121
B.1.2	Membrane Fabrication . . . . .	122
B.1.2.1	Silhouette Cutting Method . . . . .	122
B.2	Plasma Bonding . . . . .	123
B.2.1	First Bonding . . . . .	123

B.2.2	Second Bonding	124
B.3	PRIMO	125
B.3.1	PRIMO Preparation	125
B.3.2	PRIMO Protocol	125
B.4	Cell Seeding	126
B.5	Experiment	127

# List of Figures

1.1	<b>The Anatomy Lesson of Dr. Frederik Ruysch</b> , 1670 by Adriaen Backer. (Adriaen Backer Wikipedia, 1670) . . . . .	3
1.2	<b>Mechanics of cytoskeletal filaments</b> : Schematic and sizes of actin filaments, intermediate filaments and microtubules; along with the strain response to shear stress. <i>Adapted from (Leggett et al., 2021)</i> . . . . .	5
1.3	<b>Intercellular forces through actomyosin cables and cadherins</b> : Schematic showing mechanical connections between adhesions and tissue force transmission with actomyosin cytoskeleton and adhesion proteins. <i>Adapted from (Ladoux and Mège, 2017)</i> . . . . .	6
1.4	<b>Cell-matrix interaction with respect to matrix stiffness and cell density</b> : In higher tension condition, the nucleus is deformed triggering mechanotransduction and causing alterations in cytoskeleton and tractions. <i>Adapted from (Xi et al., 2018)</i> . . . . .	7
1.5	<b>Forms of epithelial tissues</b> : Simple squamous, cuboidal, columnar epithelia and pseudostratified epithelia. <i>Adapted from (zot)</i> . . . . .	8
2.1	<b>Multiscale imaging and tracking of embryo cell dynamics</b> : Top panels show <i>in toto</i> imaging of germlayer specification; red is mesendoderm, blue is epiblast, and yellow is endoderm. Bottom panel shows data analysis of long term pan embryo cell dynamics (Shah <i>et al.</i> , 2019) . . . . .	13
2.2	<b>D'Arcy Thompson's fishes</b> and his theory of transformation. (Thompson, 1979, Wolfram, 2017) . . . . .	14
2.3	<b>Mechanobiological strategies for studying morphogenesis</b> <i>Adapted from (Vianello and Lutolf, 2019)</i> . . . . .	18

3.1	<b>Actin and Myosin:</b> (A) Electron micrograph of Actin filament with zoomed in images of barbed and pointed end. (B) Same for Myosin II minifilament with clearly visible two globular heads and a long tail. (C-D) Actin network can apply pushing force through polymerization of single filaments or network expansion. (E,F) While myosin activity would lead to contraction of the networks. <i>Adapted from A-B (Alberts, 2015) and C-F (Clarke and Martin, 2021)</i>	24
3.2	<b>Forms of actin networks:</b> (A) Actin treadmilling: where highlighted actins move from positive end to negative end as the filament polymerizes and depolymerizes from both ends. (C) In an adherent cells, there are many different kinds of actin structures from contractile network to gel-like cortex. (B,D,E,F) Actin structures can be thought as meshwork of actin filaments (red) with crosslinkers(green). Different crosslinkers produce distinct form of actin network. <i>Adapted from (Alberts, 2015)</i>	25
3.3	<b>Morphogenesis driven by actin at tissue scale:</b> (A) Apical contraction or basal relaxation both results in the same curvature. (B) However, amount of deformation will depend on the contractility gradient. (C) Lateral surface of cells can also undergo expansion or contraction leading to cell rearrangements or tissue folding. (D-G) Supracellular actin cables plays vital role in creating boundaries or causing large scale deformations. <i>Adapted from (Clarke and Martin, 2021)</i>	27
3.4	<b>Actin organization at different scales:</b> (A) Electron micrograph of actin cortex of mitotic Hela cells (Kelkar <i>et al.</i> , 2020). (B) Different forms of actin organization in circular fibroblast cell (Jalal <i>et al.</i> , 2019) Scale= 10 $\mu m$ . (C) Supracellular actin ring during wound closure (Brugués <i>et al.</i> , 2014) Scale= 20 $\mu m$ . (D) Dorsal closure of amnioserosa with actin network (Ducuing and Vincent, 2016) Scale= 10 $\mu m$ . (E) Supra-cellular organization of actin for cellularization of coenocyte. Circle is 60 $\mu m$ (Dudin <i>et al.</i> , 2019). (F) Hydra with actin network, whose nematic defects determines morphogenesis (Maroudas-Sacks <i>et al.</i> , 2021) Scale= 100 $\mu m$ .	28
3.5	<b>Timescale of actin network related processes:</b> Timescales of different actin driven cellular processes, ranging from cytoskeletal fluid deformation to large-scale tissue deformations. <i>Adapted from (Kelkar <i>et al.</i>, 2020)</i>	29

3.6	<b>D'Arcy Thompson's forms of tissues:</b> (A-B) Thompson equates cell aggregates to coalescence of bubbles like in a froth. (C) A dragon fly wing is a clear example of this organization. <i>Adapted from (Thompson, 1979)</i>	31
3.7	<b>Vertex model for cells in a monolayer</b> <i>Adapted from (Gómez-González et al., 2020).</i>	31
3.8	<b>Stress strain behavior of materials:</b> (A) materials being stretched or compressed. (B) Quasistatic deformations yield stress-strain curves. (C) Creep test where strain response is characterized at constant stress.	34
3.9	<b>Active nematics:</b> Schematics of (A) nematic or polar particles, (B) extensile and contractile force dipoles, (C) Various types of defects and related motion of cells <i>Adapted from (Xi et al., 2018).</i>	36
3.10	<b>Active surface models:</b> (A) Tissues or cell surfaces can be modeled as surface with stresses and torques along the thickness. (B) Internal and external forces actin on a surface element. The kinematics of these surfaces, mathematical tools from differential geometry can be applied, using generalized coordinates ( $X$ ), metric tensor ( $g$ ), and curvature tensor ( $C$ ), where ( $dl$ ) is the length of the line element with tangential unit vector ( $v$ ). <i>Adapted from (Salbreux and Jülicher, 2017)</i>	37
4.1	<b>A conceptual representation of two approaches to understanding mechanics: reconstruction (bottom-up) and deconstruction (top-down).</b> In reality, they are not separate from each other. These methods inform each other, with past top-down research guiding new reconstruction, and new engineered cells or tissues furthering our understanding of the field in innovative directions.	40
4.2	<b>Controlling geometry and physical forces:</b> The concept of scaffolding can be divided into two categories: static and dynamic scaffolds. (A) Static scaffolds are microfabricated structures that cells can adapt to and respond to geometrical cues, leading to the formation of a specific tissue organization (Brassard <i>et al.</i> , 2021). (B) In contrast, dynamic scaffolds consist of cell-laden matrices that are deformable, and their curvature can change dynamically due to external pressure or mechanical forces (Blonski <i>et al.</i> , 2021, Chan <i>et al.</i> , 2018). (C) Bio-hybrid assemblies can incorporate active contraction or pushing to create hybrid structures, such as origami folding triggered by fibroblast contraction (He <i>et al.</i> , 2018), or cells carving out an intestinal crypt-like geometry from a softer matrix (Gjorevski <i>et al.</i> , 2016).	42

4.3	<b>Manipulating biochemical signaling:</b> Biochemical signaling and mechanics are interdependent in morphogenetic processes (A). The transport of signaling molecules can affect the cytoskeleton and mechanical properties of cells, while mechanical forces can also influence biochemical signaling. Microfluidics (D) is one method used to control biochemical signaling by providing opposing morphogen gradients through multiple channels (Demers <i>et al.</i> , 2016). Alternatively, cells can be genetically engineered to undergo apical constriction (C) or produce morphogen gradients (E) locally to form curved geometries (Cederquist <i>et al.</i> , 2019, Martínez-Ara <i>et al.</i> , 2022). Mesenchyme condensation (B) is another approach used to program curvature in developing tissues (Hughes <i>et al.</i> , 2018, Palmquist <i>et al.</i> , 2022). . . . .	44
4.4	<b>D'Arcy Thompson compares biological budding to splashes</b> (A) of fluids and Rayleigh-Plateau instability (Thompson, 1979) (B), where liquid splits up into smaller droplets. This mechanism could also be seen in organogenesis of mammary tissue (C, D) (Fernández <i>et al.</i> , 2021). . . . .	45
4.5	<b>Compressive stresses</b> occur frequently in many systems (A). We can consider epithelia and matrix as thin sheet supported by a compliant substrate. Thus, the tissue folding could be understood as buckling of sheets (B) or wrinkling or creasing of thin film supported by an hydrogel (C). . . . .	46
4.6	<b>Examples of mechanical instabilities:</b> (A) Synthetic mini brains illustrate the wrinkling of the outer layer with swelling mimicking gyrification (Tallinen <i>et al.</i> , 2016). (B, D) Other way around where inner layer of lung or intestinal epithelia develops folds when embedded into a hydrogel or muscle shell (Shyer <i>et al.</i> , 2013, Varner <i>et al.</i> , 2015). (C) It is also shown that simple epithelial tissues embedded into a shell would also buckle (Trushko <i>et al.</i> , 2020). (D) (Wyatt <i>et al.</i> , 2020) used matrix independent tissue with compression to illustrate that the epithelial tissue itself can undergo buckling. <i>Panel A, D are adpated from (Collinet and Lecuit, 2021) and C from (Matejčić and Trepak, 2020)</i> . . . . .	48

4.7	<b>Tissue hydraulics</b> plays an essential role in establishing (A) embryonic axis through lumen coarsening, and later the pressure regulates the size of the embryo. Laplace's law acts on the spherical cavities between cells to the whole blastocyst (Chan <i>et al.</i> , 2019, Collinet and Lecuit, 2021, Dumortier <i>et al.</i> , 2019). (B) Interestingly, if the inflated structure is surrounded by a mesh you see a stressball effect, where material inflates through the mesh. Similar phenomena is visible in growth and inflation of the lizard lungs. The smooth muscle constrains the deformation leading to stressball morphogenesis (Palmer <i>et al.</i> , 2021). (C) In cnidarians, the different orientation of F-actin leads to different shapes of the organism (Stokkermans <i>et al.</i> , 2022). . . . .	50
4.8	<b>Historical development of epithelial domes:</b> (A) Distended epithelium was observed in explant cultures in 1930-50s. (B) With MDCK cell line, spontaneously forming domes/hemicysts were characterized (Leighton <i>et al.</i> , 1969, Valentich <i>et al.</i> , 1979). (C,D) In our lab, shape and size of the domes were controlled with micropatterning adhesion protein (Latorre <i>et al.</i> , 2018). The pressure and tension was measured with Laplace's law and traction force microscopy. (E-F) For non-spherical domes, curved monolayer stress microscopy technique was implemented by segmenting the dome shape (Marín-Llauradó <i>et al.</i> , 2022). . . . .	52
4.9	<b>Methods for measuring pressure and tension:</b> (A) Earlier studies tried to estimate tension through geometry and thickness of the monolayer (Tanner <i>et al.</i> , 1983). (B) Later, pressure was measured by puncturing the dome with a micro-needle. However, the measurement of pressure is static, because the dome deflated after the puncturing (Choudhury <i>et al.</i> , 2022b). (C) Traction force microscopy technique provides a viable non-invasive solution for measuring pressure under to domes (Latorre <i>et al.</i> , 2018). . . . .	53
6.1	<b>Conceptual design of MOLI:</b> (A) Microfluidic device consist of a porous membrane sandwiched between two layers of schannels. (B) Upon application of pressure, cells from low adhesion will detach to form an epithelial dome. . . . .	62
6.2	<b>3D printed mold for the device</b> patterned to prepare eight devices at a time. The thickness of the PDMS block is controlled with volume of PDMS poured into the mold. After polymerization, the PDMS is cut into individual pieces and inlets are punched with a biopsy punch. . . . .	63

6.3	<b>Fabrication of MOLI:</b> Four layers assembled together with ozone plasma cleaning. Each channels has a inlet and outlet. Only the pressure channel is connected to the tubing; one side connects to the reservoir and other is sealed.	64
6.4	<b>Cells filtering through the membrane:</b> (A) Images of MDCK-CiBN CAAX GFP monolayer on the both sides of the membrane. Scale bar is $80\mu m$ . (B) Schematic of imaging through the porous layer.	66
6.5	<b>Upside-down cell culture:</b> Illustration of upside-down cell culture and the experimental setup on the microscope stage.	67
6.6	<b>Hydrostatic pressure application:</b> The device is positioned on a microscope stage and connected to a reservoir of media, which in turn is attached to a translation stage. By increasing the difference between the device and the air-liquid interface, we can measure and apply hydrostatic pressure.	68
6.7	<b>Epithelial dome:</b> Representative confocal microscopy sections of domes at 0 Pa and 200 Pa. Images in the XY plane represent the dome's maximum projection, while images in the XZ plane represent a cross section at the center plane. Three cells are highlighted with color to show the stretching during the dome inflation. Scale bar is $20\mu m$ .	69
6.8	<b>Imaging the dome with Line scanning mode:</b> (A) Confocal microscopy image of a dome's maximum projection. (B) Midsection of the same dome imaged with the line scan mode (LSM). (C-D) Time-lapse of the dome in LSM and a kymograph showing dynamics of the domes when imaged at time-step of 4s. Scale bars are $20\mu m$ .	70
6.9	<b>Light sheet MOLI:</b> (A) Isometric illustration of a single piece PDMS block engraved with two channels, so that we can have two devices in one. (B) Cross-section of the device. (C) The device is used with 40x immersion objectives coming at 45 deg angle. This limits to the field of view to $332 \times 332\mu m^2$ .	71
6.10	<b>Dome imaged with Light sheet MOLI:</b> Mid-section of a dome with membrane marker imaged every 2s. Showing the shape of individual cells undergoing changes during deflation. Scale bar is $20\mu m$ .	72
7.1	<b>Epithelial dome generated by the MOLI device:</b> Maximum intensity projection of an MDCK dome (Left). Dashed yellow line indicates the dome's footprint. Vertical yellow line crosses the center of the footprint, where the cross-section (Right) shows the spherical shape of the dome. MDCK Cells were expressing CIBN CAAX GFP-488. Pressure, 200 Pa. Scale bar is $20\mu m$ .	76

7.2	<b>Epithelial domes at constant pressure:</b> Dynamic response of three representative domes at a constant pressure of 200 Pa (Domes with base radius: red 56 $\mu\text{m}$ , blue 63 $\mu\text{m}$ , purple 42 $\mu\text{m}$ ): (A) Areal strain increases and reaches a steady state at around 5 minutes, and we can clearly see variability in the maximum strains. (B) The same domes produce a peculiar tension and strain curve. In an inset on top, all three curves collapse onto a single master curve, when tension $\sigma$ is normalized by base radius $a$ and plotted with respect to areal strain $\epsilon$ . (representative of 12 domes) . . . . .	77
7.3	<b>Illustrative explanation for isobaric curve:</b> Tension and strain are related to each other through the geometric constraint of a spherical cap. Here, the base radius ( $a$ ) is constant, so the radius of curvature is almost infinite for domes with very small strains (<0.05). As the strain increases, the radius of curvature decreases to a minimum corresponding to the base radius. Then it continues to increase again. . . . .	79
7.4	<b>Steady-state constitutive Relation of epithelial monolayers:</b> (A) We set up experiments to probe the steady state at different pressures. We will start from the highest pressure, move along the isobaric line and achieve a steady state, and then move down to the next curve, and so on. (B) The constitutive relation between dome strain and tissue tension was experimentally obtained ( $n=12$ ). The line and shaded area represent the median and standard deviation, respectively, by binning 13 points in each bin. . . . .	80
7.5	<b>Dynamic response of Epithelia:</b> (A) The XZ plane images and kymographs of domes subjected to cyclic pressure between 0 to 200 Pa with rates of 20, 1.5, and 0.2 Pa/s The kymographs generated along the midsection of the domes indicated by yellow dotted lines. These indicate the evolution of height of the domes with respect to time. (B) The strain response of domes to cyclic pressure with different rates. Magenta represents pressure and red represents strain with respect to time. For A, B, $n=7$ domes for 20 Pa/s, $n = 8$ for 1.5 Pa/s, and $n = 7$ for 0.2 Pa/s. . . . .	82
7.6	<b>Active gel tissue model:</b> (A) The cell is modeled as an active gel of cortex, which mainly comprises three aspects: viscoelasticity of the network, turnover dynamics, and active contractility. (B) These cells can be assembled into a tissue that can be used to perform in-silico experiments. An example of this is the digital dome being inflated, color is highlighting individual cells increasing their area. . . . .	84

7.7	<b>Active viscoelastic response after step deformation:</b> (A) Illustration of a resting and actual area of a cell in a tissue during stretching. (B) Evolution of total tissue tension (black), viscoelastic stress (red), and active tension (yellow) in response to step deformation. . . . .	87
7.8	<b>Material response of the digital domes:</b> (A) When subjected to constant pressure, as in experiments, the digital dome inflated and reached a steady state. (B) These simulations also produced non-monotonic tension strain curves for different pressures, all leading to a steady state. The blue curve is the result of a quasi-static increase of pressure, which traces the locus of steady-state points obtained in long isobaric simulations. Tension reported here is non dimensional. . . . .	88
7.9	<b>Evolution of Resting and Actual Cell Areas in Response to Cyclic Pressure:</b> (A) Illustration of resting and actual cell areas in a monolayer during stretching. (B) Fold area change relative to the initial area, with three rows of panels showing the evolution of area change over normalized time. Digital domes were subjected to cycles with three different time intervals: 20 s (top), 266 s (middle), and 2000 s (bottom). (C) Inset of the last two cycles in the case of fast and moderate rates. . . . .	89
8.1	<b>Digital dome undergoing buckling:</b> A digital dome at a steady state is rapidly deflated to a negative pressure of $-50\text{Pa}$ . Three snapshots show the buckling process. . . . .	95
8.2	<b>Buckling protocol:</b> The pressure is increased to $200\text{Pa}$ for inflating the dome, and then the dome is given different amounts of time (hold time) to remodel before being deflated to $-50\text{Pa}$ at different rates (deflation rate) to observe whether the dome buckles or not. . . . .	96
8.3	<b>Buckling conditions:</b> (A-D) Representative montages of dome deflation for experiments and model at different deflation rates of 200 and $0.2\text{ Pa/s}$ after holding pressure constant of $200\text{ Pa}$ for 6 and 600 s. Scale bars are $20\text{ }\mu\text{m}$ for XZ. (E) Diagram representing fraction of domes buckling for different deflation rates and hold time. Showing the optimum conditions for the buckling. (F) The maximum strain achieved is lower for 6s hold time compared to 600s conditions. . . . .	97

8.4	<b>Multiscale buckling:</b> (A) Midsection of a tissue dome undergoing buckling, with dotted yellow lines representing tissue curvature. Scalebar is $20\mu m$ . (B) Buckling event at the cell junction where cells buckle at a shorter length scale. (C) Localized subcellular buckling in a single cell with varying thickness from the nucleus to the periphery. (D) Buckling at the cellular level but not at the tissue level. Scalebar is $20\mu m$ . (E) Subcellular buckling resulting in the formation of ruffles at short wavelengths (inset). Scalebar is $5\mu m$ . (F) Buckling occurring at the subcellular level. Scalebar is $20\mu m$ with an inset scalebar of $5\mu m$ . (G) Cross-sections of the membrane and actin in cells undergoing subcellular buckling. Scalebar is $5\mu m$ . (H) Region of tissue undergoing buckling at multiple length scales. Scalebar is $5\mu m$ for (C,E,G,H). . . . .	99
8.5	<b>Buckling patterns:</b> Buckling patterns observed in differently sized digital domes. The domes were grouped into three size categories and two categories based on location of folds (along the border and in the middle). We found that larger domes are more likely to buckle into a network of folds compared to smaller ones. . . . .	100
8.6	<b>Buckling patterns in spherical domes of varied size:</b> Representative examples of digital domes undergoing buckling with time-lapse of their basal cross-section (A-C). In the first frame, the onset of buckling is visible where the dome makes contact in the middle. Subsequent frames show more of the fold coming into view, and when the dome completely deflates, a fold is formed (indicated by the green arrow). Panel (D) shows the final outcome of buckling for digital domes of different sizes. Scale bar is $20\mu m$ . . . . .	101
8.7	<b>Controing the patterns of fold:</b> A-B Simulations show digital models of ellipsoidal and triangular domes buckled into line and Y-shaped junctions. C-D Experimental results confirm the simulation findings. E-F Confocal z-stack images show the folds in the case of a line and Y-shaped junction. Scale bar is $50\mu m$ . . . . .	103



## **Part I**

# **Introduction and motivation**



# Chapter 1

## Epithelial Layers

### 1.1 Introduction



**Figure 1.1:** The Anatomy Lesson of Dr. Frederik Ruysch, 1670 by Adriaen Backer. (Adriaen Backer Wikipedia, 1670)

The term “epithelia” was first introduced by Dutch botanist Frederick Ruysch in the early 18th century (see Fig. 1.1). He used it to describe the tissue he observed while dissecting the lips of a cadaver, and the word is derived from Greek roots “*epi*,” meaning top, and “*thele*,” meaning nipple.<sup>1</sup> A few decades later, Swiss scientist

---

<sup>1</sup>Ruysch is referred to as a “Artist of death” because of his famous anatomical collection. He was the first to use arterial embalming, which allowed for visualizing and dissecting smallest arteries. He also

Albrecht von Haller began using the term “epithelium/epithelia” to describe the fibers of the body, following the old Renaissance theory that the body was made of fibers, which were believed to be a fundamental building block of living things.<sup>2</sup> It was thought that these fibers and tissues arranged in different arrays gave rise to biological structures (MacCord, 2012, Zampieri *et al.*, 2014). This theory was not far off, as epithelial tissues make up more than 60% of the cells in a vertebrate’s body and are found ubiquitously, covering the organs both inside and out (Alberts, 2015).

Epithelial cells are polarized, i.e., their apical side (typically facing the lumen of the organ), which differs in shape and composition from the basolateral side. Its polar organization is reflected in the vectorial functions like creating and maintaining concentration gradients between separated compartments (Marchiando *et al.*, 2010). Typical examples of these are transporting epithelia such as those of the renal tubule, absorptive epithelia of the intestine, and secretory epithelial cells like hepatocytes (Alberts, 2015). In addition, polarized epithelia guide the developmental process by determining the fate of cells leading to symmetry-breaking events in the embryo (Kim *et al.*, 2018).

## 1.2 Key components

The function of epithelia primarily depends on the tissue’s structure and the surrounding microenvironment. It can be divided into three aspects: cell structure, microenvironment, and cell-matrix interactions.

### 1.2.1 Cell structure

The cell cytoskeleton plays a crucial role in maintaining cell shape and supporting vital functions such as cell division and migration (Alberts, 2015). The Eukaryotic cell cytoskeleton is composed primarily of filamentous proteins, including three main types of filaments that differ in size and protein composition: microtubules, actin filaments, and intermediate filaments (see Fig. 1.2). Microtubules, with a diameter of approximately 25 nm, are the largest and made of the protein tubulin. Actin filaments, with a diameter of only 6 nm, are the smallest. Intermediate filaments,

---

was part of the macabre practice of public dissections (Halley, 2019).

<sup>2</sup>Finding a fundamental unit of living entities comes from the philosophy of Gottfried W. Leibniz. It was based on the idea of “monad”. Thanks to progress in microscopy and philosophy, naturalists were able to put together ideas for cells, fibers, and even cytoskeleton! (Zampieri *et al.*, 2014)

with a diameter of around 10 nm, are composed of several different subunit proteins and have a diameter intermediate between the other two types (Mofrad, 2009). All three filament types dynamically respond to signals from the microenvironment and cell networks.

Mechanically, microtubules have higher extensional stiffness than actin filaments but break at lower extensions. Intermediate filaments have intermediate extensional stiffness and can sustain larger extensions while showing a nonlinear stiffening response (Wen and Janmey, 2011). Differences in strength and stability arise from the properties of individual subunits. The persistence length can range from  $1\mu\text{m}$  for intermediate filaments to  $1\text{mm}$  for microtubules (Fletcher and Mullins, 2010). Actin filaments, most relevant to this thesis, have a persistence length of a few microns.

The assembly and disassembly of these filaments are dictated by the dynamics of their macromolecular components and accompanying proteins. The combination of actin filaments and myosin motors forms the actomyosin cortex, which is essential in producing intra- and intercellular forces. In an epithelial tissue, the actomyosin cortex and intercellular junctions make cell-to-cell contacts stronger and provide tissue integrity (Braga, 2016) (see Fig. 1.3). A good example of these tissue-level structures can be observed in wound healing assays, where cells surrounding the wound create a ring of actin to close it (Brugués *et al.*, 2014). In Chapter 3, we will delve into the actomyosin network in more detail.

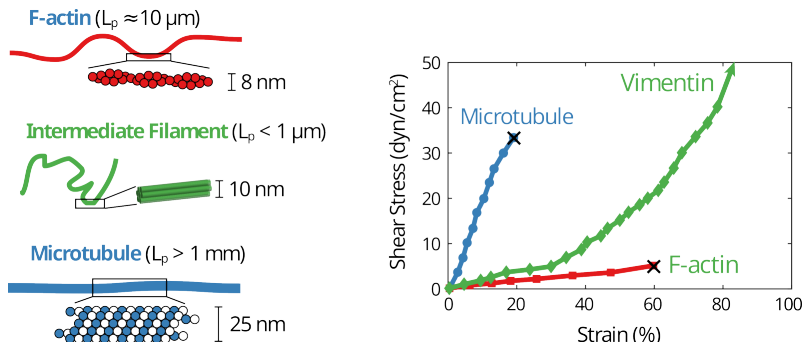


**Figure 1.2: Mechanics of cytoskeletal filaments:** Schematic and sizes of actin filaments, intermediate filaments and microtubules; along with the strain response to shear stress. Adapted from (Leggett *et al.*, 2021)

Multiple membrane molecules can facilitate cell adhesion, including cadherins. Cadherins are a crucial component for epithelial cell cohesion and the formation of adherens junctions, which transmit forces between cells. This key factor is in-

volved in the mechanical regulation of cell division and tissue rearrangement during development and homeostasis (Godard and Heisenberg, 2019, Mertz *et al.*, 2013). Desmosomes, another type of intercellular junction, are coupled with intermediate filaments and provide mechanical resilience to cell layers (Hatzfeld *et al.*, 2017, Latorre *et al.*, 2018). Tight junctions serve as a barrier and regulate the active transport of ions across epithelial layers, playing an important role in controlling fluid pressure in tissues (Chan and Hiiragi, 2020, Marchiando *et al.*, 2010).

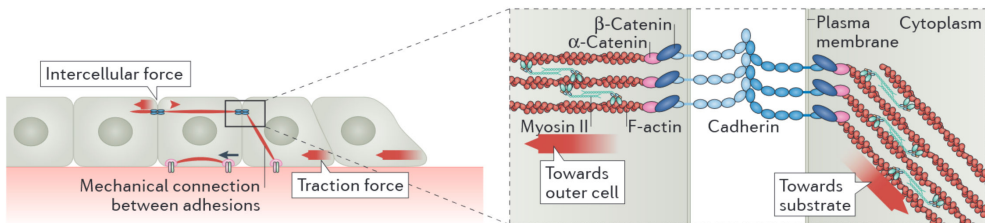


**Figure 1.3: Intercellular forces through actomyosin cables and cadherins:** Schematic showing mechanical connections between adhesions and tissue force transmission with actomyosin cytoskeleton and adhesion proteins. *Adapted from (Ladoux and Mège, 2017)*

### 1.2.2 Microenvironment

The extracellular matrix (ECM) is the substrate or cell environment to which cells adhere. It is also referred to as the matrix, mesenchyme, or cellular microenvironment. The ECM serves many functions. It endows tissues with strength, thereby maintaining their shape. Additionally, it serves as a biologically active scaffolding that allows cells to migrate or adhere. The ECM also plays a role in regulating the phenotype of cells. It provides an aqueous environment that facilitates the diffusion of nutrients, ions, hormones, and metabolites between the cell and the capillary network (Alberts, 2015).

Moreover, the ECM is subjected to mechanical forces such as blood flow in endothelia, air flow in respiratory epithelia, or hydrostatic pressure in the mammary gland and bladder (Walma and Yamada, 2020, Waters *et al.*, 2012). It has been shown that the ECM regulates cell shape, orientation, movement, and overall function in response to biophysical forces (Alberts, 2015).

The ECM is a fibrous network of proteins, consisting of collagen, elastin, and proteoglycans as its primary structural components. Collagen is one of the most abundant proteins in the body, while elastin is the most elastic and chemically stable

protein. Proteoglycans can sequester significant water as well as growth factors and proteases. The water content of the ECM allows it to deform as a poroelastic material, absorbing water upon stretching and releasing it under compression, causing a hydraulic fracture effect (Casares *et al.*, 2015). The collagen network can also remodel under the influence of cells and mechanical forces (Humphrey *et al.*, 2014).

Most ECM components undergo continuous turnover, some quickly and some slowly. For example, the half-life of collagen in the periodontal ligament is a few days, whereas that in the vasculature may be several months (Humphrey *et al.*, 2014). In response to altered physical stimuli, disease, or injury, the rates of collagen synthesis and degradation can increase many times, allowing for a rapid response.

### 1.2.3 Cell-Matrix interaction

The cells and the extracellular matrix (ECM) are in a dynamic relationship, constantly exchanging information and influencing each other. The cells sense the biophysical cues in the ECM through sensors such as integrins and focal adhesion complexes, which are responsible for cell-substrate adhesion (Kechagia *et al.*, 2019) (see Fig. 1.4). These adhesions allow cells to respond to various stimuli such as matrix stiffness, ligand density, and chemotactic gradients (Fortunato and Sunyer, 2022). It has also been shown that cells can respond to the viscoelasticity of the matrix (Elosegui-Artola *et al.*, 2022).

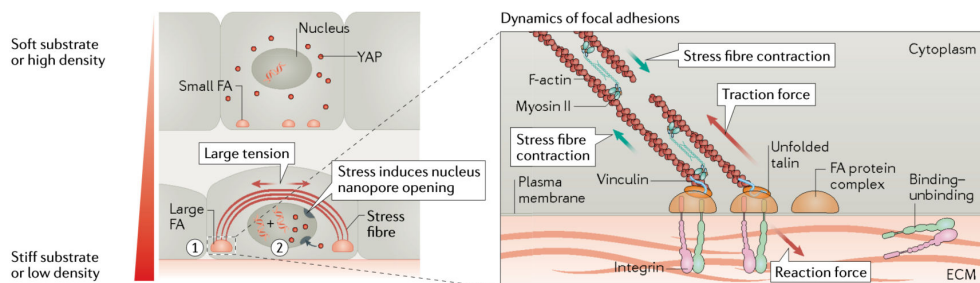


**Figure 1.4: Cell-matrix interaction with respect to matrix stiffness and cell density:** In higher tension condition, the nucleus is deformed triggering mechanotransduction and causing alterations in cytoskeleton and tractions. *Adapted from (Xi et al., 2018)*

In addition to sensing the ECM, cells also contribute to its composition by secreting ECM components or remodeling the substrate (Malandrino *et al.*, 2018). This interplay between the cells and ECM can impact the tissue behavior fundamentally, as the

connections between focal adhesions and the nucleus can affect the expression of transcriptional factors (Lomakin *et al.*, 2020, Venturini *et al.*, 2020). The precise control of cell-cell and cell-substrate interactions enables cells to transform into intricate shapes, such as curved forms in cell sheets (Schamberger *et al.*, 2022).

### 1.3 Forms of epithelia

The structure and arrangement of epithelial cells are crucial for maintaining the integrity and homeostasis of tissues and organs (see Fig. 1.5). Simple epithelia are single-cell layers where all cells are in contact with the underlying basal lamina and have a free surface on the apical side. The shape of the cells can vary, ranging from flat to cuboidal to columnar. Stratified epithelia, on the other hand, have two or more layers of cells. Additionally, there are pseudostratified epithelia, which appear to be stratified, but are monolayers where the cell nuclei are positioned in a manner that gives the appearance of a stratified epithelium.

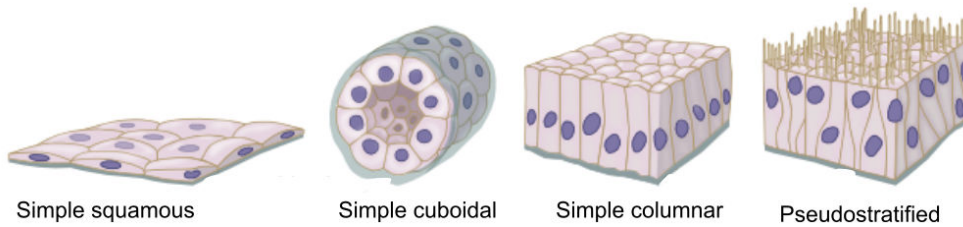


**Figure 1.5: Forms of epithelial tissues:** Simple squamous, cuboidal, columnar epithelia and pseudostratified epithelia. *Adapted from (zot)*

The classification of epithelia was first established in the XIXth century based on their structure and physiological characteristics. Germ layer theory, developed by embryologists, further expanded the epithelial nomenclature (MacCord, 2012). During early embryogenesis, three layers emerge: endoderm, mesoderm, and ectoderm. The ectoderm forms the epithelia lining the skin, mouth, and nervous system, while the endoderm gives rise to the digestive tract, respiratory system, and liver. The mesoderm, in turn, develops the endothelia covering much of the circulatory and lymphatic systems.

It is important to note that not all tissues classified as epithelia, mentioned in this thesis, are purely composed of epithelial cells. They may be a mixture of different cell

types that have epithelial-like characteristics. The focus of this thesis is on packed cell monolayers, which can form and self-organize into various 3D shapes, ranging from simple spheres to complex branched tubules. The thesis will explore the role of mechanics in epithelial morphogenesis.



## **Chapter 2**

# **The mechanical basis of Morphogenesis**

### **2.1 The complexity of the morphogenesis**

Epithelial cells play a crucial role in the formation of transient structures during embryonic development, such as the neural tube, somites, and precardiac epithelium, which serve as the precursor for the development of complex organs. During this process, different types of epithelia acquire distinct morphological forms and perform specific functions, including branched lungs, looped gut, kidney tubules, thyroid follicles, and sinusoids in the liver. The regulation of epithelial morphogenesis is a complex and hierarchical process that involves coordinated events at multiple spatial and temporal scales (Trepat and Sahai, 2018).

Some processes appear to be happening fast at the local level, such as cell shape changes through apical constrictions, which lead to global changes, such as the formation of a ventral furrow in a *Drosophila* embryo (Martin *et al.*, 2009). At the same time, chemical signaling events that activate these processes are slow and occur at a global level. The same complexity can be seen in *in vitro* systems, where a cluster of dissociated stem cells can assemble into an organoid or gastruloid and undergo global folds in response to appropriate culture conditions (Collinet and Lecuit, 2021).

The underlying mechanisms of epithelial morphogenesis are intricate and involve multiple factors, including genes responding to morphogen gradients, molecular machinery involved in apical constriction, and mechanical stresses that cause tissue-

scale deformations. To fully understand the phenomenon of epithelial morphogenesis, it is essential to study these processes in detail, at multiple levels of complexity (Lecuit *et al.*, 2011, Schöck and Perrimon, 2002).

Rudolf Virchow's third tenet of the cell theory states that "omnis cellula e cellula," meaning "all cells come from cells" (Virchow *et al.*, 1860).<sup>1</sup> Although all tissues originate from cells that contain essentially the same genetic information, each tissue has a distinct architecture and function. This raises several questions, such as: what makes cells different from each other? Are differences due to genes, environmental factors, or both? What drives shape changes in tissue morphogenesis? Over the last two centuries, the field of developmental biology has addressed many of these questions, but it has also raised new issues and left others unanswered.

Until last decade, the focus of the field had been on tracking and mapping patterns of cell movements to patterns of gene or protein expression (Gorfinkel and Martinez Arias, 2021). While these studies are influential and important for understanding morphogenetic patterns, they fall short in explaining how cells and tissues are physically shaped (Odell *et al.*, 1981, Veenvliet *et al.*, 2021). This is because the physical understanding of tissues has been limited to kinematic descriptions, which only describe tissue deformation or cell motion. However, we know that cells and tissues actively drive shape changes and movements through the generation of mechanical forces (Lecuit *et al.*, 2011). Thus, to have an integrated understanding of morphogenesis, we must consider the role of forces and mechanics.

## 2.2 On growth and form

Throughout history, the form of both animate and inanimate objects has been closely linked to their intended function. In fact, the 20th-century architectural principle 'form follows function' highlights the idea that the organization of a structure should be based on its intended purpose. However, in developmental biology, the relationship between form and function is more complicated. For instance, self-assembling systems such as intestinal organoids, cancer spheroids, and gastruloids are perfect examples of this relationship, as each structure emerges from a set of cells in a suitable environment, adapting to perform a specific biological function (Gjorevski *et al.*,

---

<sup>1</sup>The famous epigram was coined by François-Vincent Raspail. Virchow is regarded as influential biomedical scientist of 19th century, but more interesting part is as a radical who took part in the March revolution of 1848. He was one of the first to advocate for the social origins of illness (Brown and Fee, 2006, Wright and Poulsom, 2012).

2016, Ishiguro *et al.*, 2017, Morizane and Bonventre, 2017, Vianello and Lutolf, 2019). However, in numerous *in vitro* experiments that involve a controlled cellular environment, the opposite principle appears to be at work. In these experiments, geometric constraints appear to drive biological function (Xi *et al.*, 2018). For example, seeding stem cells in a bio-printed three-dimensional geometry of the gastrointestinal tract can lead to the production of functional tissues with physiological characteristics of the intestine. The curvature of the structure can even control the formation of villus-like structures (Brassard *et al.*, 2021).

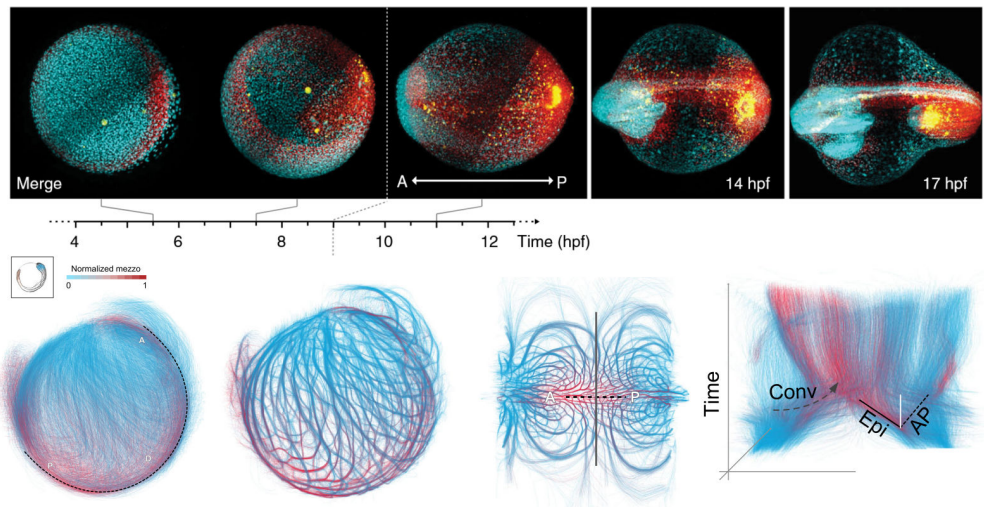


**Figure 2.1: Multiscale imaging and tracking of embryo cell dynamics:** Top panels show *in toto* imaging of germlayer specification; red is mesendoderm, blue is epiblast, and yellow is endoderm. Bottom panel shows data analysis of long term pan embryo cell dynamics (Shah *et al.*, 2019)

In a way, assembly of biological systems treads the line between self-organization and programmed material. Advanced microscopy techniques have allowed us to witness the intricacies of developmental processes with unprecedented clarity (see Fig. 2.1). We can now observe cells and their motion throughout the morphogenetic process, from the formation of a spherical embryo to the creation of a complete organism (Shah *et al.*, 2019). Cells undergo shape changes and large-scale flows as they undergo morphogenesis, driven by mechanical forces in concert with biochemical processes (Labernadie and Trepat, 2018, Lecuit *et al.*, 2011, Trepat and Sahai, 2018). Thus, the dichotomy of form and function is incomplete without considering the

physical laws of mechanics.

Over a century ago, D'Arcy Wentworth Thompson wrote the influential book "On Growth and Form" (Thompson, 1979), in which he explored the relationship between geometry, physics, and biology in the context of morphogenesis. Thompson used examples to show how mathematical principles can explain biological phenomena, such as his theory of transformations, which demonstrates how related species can be represented geometrically (see Fig. 2.2). According to Thompson's daughter, he even used to draw pictures of dogs on rubber sheets and stretch them to show children how poodles could become dachshunds (wol). This distortion of shape represents significant alterations in various forces or rates of growth throughout the developmental processes of different organisms.

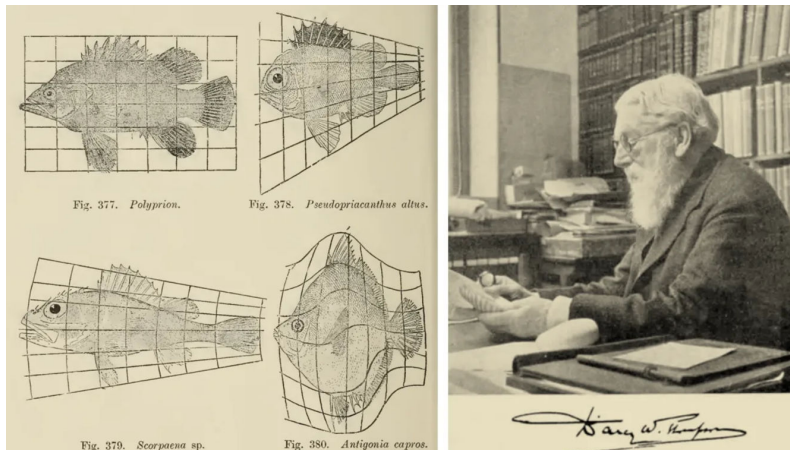


**Figure 2.2:** D'Arcy Thompson's fishes and his theory of transformation. (Thompson, 1979, Wolfram, 2017)

Thompson's approach was highly speculative, but his goal was to identify general principles behind the diverse forms and patterns found in biology. He compared growth curves of haddock, trees, and tadpoles, and found logarithmic spirals in shells, horns, and leaf arrangements.<sup>2</sup> Essentially, this book emphasized two points: first, all material forms of living things—cells, tissues, and organs—must obey the laws of

<sup>2</sup>Funnily, He criticized the zoologists and morphologists of the time of assigning shapes to psychical instinct of the organism or some divine interference for creating the perfect shapes: "He finds a simple geometric construction, for instance in the honeycomb structure, he would fain refer it to psychical instinct or design rather than in the operation of physical forces. ... When he sees in snail, or nautilus, or tiny foraminiferal or radiolarian shell a close approach to sphere or spiral, he is prone of old habit to believe that after all it is something more than a spiral or a sphere, and that in this "something more" there lies what neither mathematics nor physics can explain"

physics, and second, quantitative measurements are necessary to unravel the physical principles of biology.

Thompson's work continues to inspire researchers even today. Right as I began my Ph.D., the centenary of the book's publication was being celebrated in the fields of developmental biology and biophysics (nat, 2017a,b, Heer and Martin, 2017). Even more so by the field of mechanobiology, an interdisciplinary field that studies the role of biophysical forces in cell and tissue functioning.

## 2.3 Mechanobiology

The cells within epithelial tissue can be viewed as mathematical systems that integrate multiple input cues to result in an output behavior. These inputs can be mechanical or chemical, such as the stretching of lungs or the presence of morphogen gradients during embryonic development. The outputs can include cell deformation, migration, differentiation, or proliferation (Kumar *et al.*, 2017). Some outputs can even feedback into the system as an input, such as when cells remodel the matrix (Malandrino *et al.*, 2018). Mechanochemical switches at the membrane, cell-cell junctions, or cell-matrix adhesions mediate the sensing of the environment, triggering a biochemical cascade that leads to a cellular response (Roca-Cusachs *et al.*, 2017). This interplay between biochemistry and mechanics is known as mechanotransduction.

During morphogenesis, mechanotransduction occurs at various scales, ranging from a single cell to complex multicellular tissue. To understand the role of different variables, experiments at different scales are necessary. It has been observed that individual cells can sense their environment and respond by altering their behavior through mechanical or biochemical processes. Whereas, multicellular systems can transmit forces and information at a longer length scale, allowing for emergent characteristics such as collective migrations, oscillations, rearrangements, and even turbulent flows (Heer and Martin, 2017, Lecuit *et al.*, 2011, Trepat and Sahai, 2018).

An excellent demonstration of the interaction between tissues and their environment is provided by the phenomenon of durotaxis. Epithelial cells can detect changes in the stiffness of the extracellular matrix and migrate towards areas of higher rigidity. This migration towards stiffer regions has been observed both *in vitro*, where cells in a monolayer collectively expand and relocate to stiffer areas, and *in vivo*, such as during the migration of neural crest cells in *Xenopus laevis* (Shellard and Mayor, 2021, Sunyer *et al.*, 2016). It is worth noting that the migration of neural crest cells

themselves generates the durotactic gradient. In another example, during *Drosophila* oogenesis, the disorganized matrix is remodeled by cells to create a polarized matrix that aligns with the actin bundles in the follicular epithelium. This alignment is achieved through the coordinated rotation of cells and can guide the directed motion of cells along the polarized fibers (Cetera *et al.*, 2014, Haigo and Bilder, 2011).

The interplay between individual cells, their neighbors, and exogenous stimuli makes it difficult to decouple various biophysical aspects of the environment, such as forces, pressures, matrix stiffness, spatial confinement, porosity, or viscoelasticity. Direct force measurements in and out of tissues are also challenging. To address these challenges, researchers from various disciplines have attempted to recreate experimental systems with precise control over the biochemical and mechanical environments of cells (Xi *et al.*, 2018). This has been made possible through continuous technological advancements in fluorescent probes, imaging, microfabrication, and force measurements (Roca-Cusachs *et al.*, 2017). In the following section, I will provide an overview of relevant techniques and experiments in the field of mechanobiology.

### 2.3.1 Synthetic substrates

The use of Polyacrylamide and soft PDMS gels has enabled researchers to investigate mechanical interactions at cell-substrate adhesion (see Fig. 2.3 A). Simply seeding cells on hydrogels of different stiffnesses reveals a significant impact on the actin cytoskeleton, cell shape, and lineage specification (Engler *et al.*, 2006, Yeung *et al.*, 2005). These substrates, because of their known elastic response, are also utilized in techniques like traction force microscopy (TFM) to measure the forces exerted by cells and tissues on the substrate (Gómez-González *et al.*, 2020, Harris *et al.*, 1980) (see Fig. 2.3 D). TFM studies have shown that cells and tissues can exert greater forces on stiffer substrates as a result of the remodeling of the cytoskeleton (Elosegui-Artola *et al.*, 2016). Higher matrix stiffness has also been found to induce the translocation of Yes-associated protein (YAP) from the cytoplasm to the nucleus, which is considered a sensor for mechanotransduction (Elosegui-Artola *et al.*, 2017). However, increasing extracellular matrix (ECM) ligand density alone can induce YAP nuclear translocation without changing substrate stiffness (Stanton *et al.*, 2019).

### 2.3.2 Geometric control

The shape of cells or tissues on 2D substrates can be controlled using micropatterned adhesion proteins or microfabricated stencils. Protein patterning techniques are used to pattern adhesion promoting proteins and control cell attachment and spreading, while microfabricated stencils physically confine cells in a particular geometry (see Fig. 2.3 B C). When cells are confined, they respond by reorganizing their actin cytoskeleton and focal adhesion complexes to match the shape imposed on them (Vignaud *et al.*, 2012). Confined tissues undergo larger-scale rearrangements, leading to the formation of fascinating topological defects or oscillations (Balasubramaniam *et al.*, 2021, Guillamat *et al.*, 2022, Tlili *et al.*, 2018). Through these experiments, we can uncover the mechanisms of force transmission and regulation of collective cell migration and epithelial growth in two dimensions (Deforet *et al.*, 2014, Nelson *et al.*, 2005, Vedula *et al.*, 2012).

Embryonic stem cells subjected to 2D confinement have been shown to differentiate based on the shape and size of the confinement. For example, a circular monolayer of stem cells can reproduce the tissue patterning of a 3D gastruloid (Warmflash *et al.*, 2014), and confinement in a triangular shape can lead to high tension at the vertices and activate Wnt signaling, promoting differentiation to mesoderm (Muncie *et al.*, 2020). Moreover, advancements in photopatterning technologies allow for precise control of multiple proteins on the same substrate (Guyon *et al.*, 2021, Prahl *et al.*, 2022), enabling the establishment of complex co-culture systems that mimic *in vivo* events.

Not just 2D shape, epithelial monolayers are also able to respond to curvature by regulating cell migration, orientation, cell/nucleus size, and shape (Marín-Llauradó *et al.*, 2022, Schamberger *et al.*, 2022) (see Fig. 2.3 C). For example, an epithelial monolayer on hemispheres of elastomers acts as a fluid with increasing curvature (Tang *et al.*, 2022). On a smaller scale, cells attached to corrugated hydrogels show variations in lamins, chromatin condensation, and cell proliferation rate in response to curvature (Luciano *et al.*, 2021). Bio-printing of three-dimensional tissue architectures can also create functional tissues (Brassard *et al.*, 2021, Breau *et al.*, 2022).

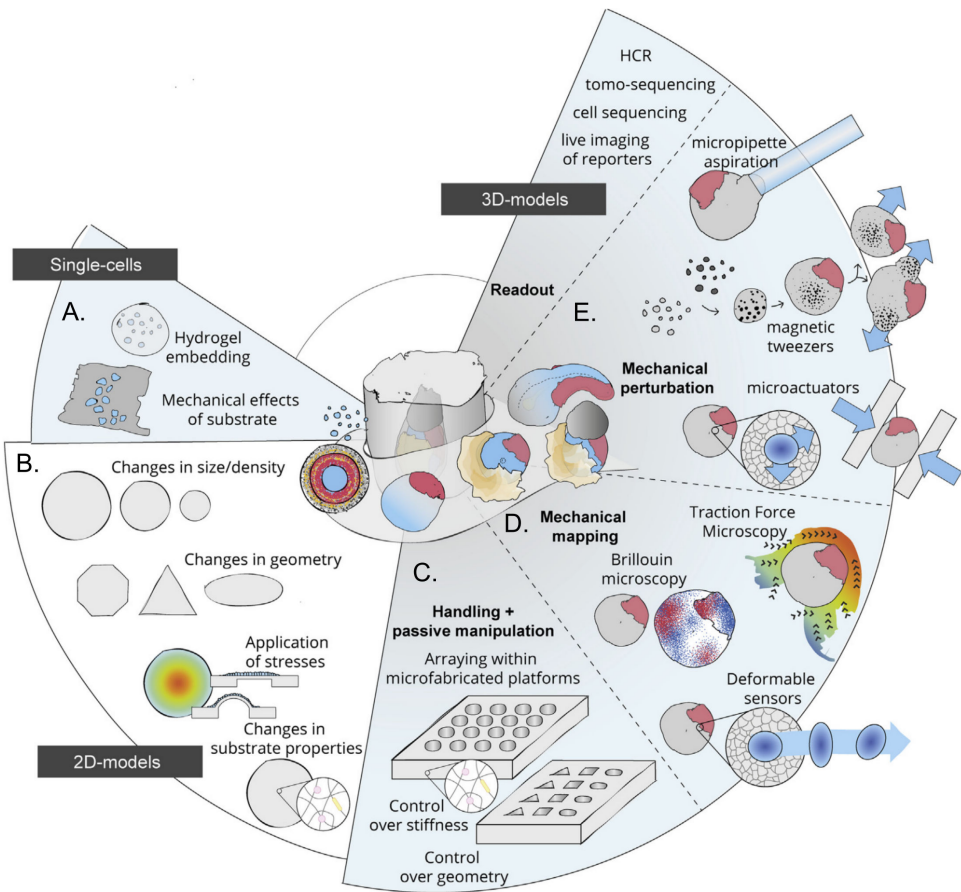


**Figure 2.3: Mechanobiological strategies for studying morphogenesis** Adapted from (Vianello and Lutolf, 2019)

### 2.3.3 Mechanical control

Living systems have mechanical control in addition to spatial control, as physical forces emerge from growth, deformation, and remodeling of the extracellular matrix (ECM) and fluid pressure in closed geometries. For example, the intestinal epithelia are stretched during peristaltic movements in the gut and lung alveoli deformations during breathing. Compression can also guide morphogenetic events that involve tissue bending and folding, such as the formation of the optic cup, gut villi, and cortical convolutions in the brain (Okuda *et al.*, 2018, Shyer *et al.*, 2013, Tallinen *et al.*,

2016).

To study tissue behavior under external perturbation, cells and tissues are probed at the molecular and subcellular scales using techniques such as atomic force microscopy, magnetic beads, optical tweezers, and micropipettes (Bao and Suresh, 2003) (see Fig. 2.3 E). At a larger scale, various types of stretching devices, tissue rheometers, and force plates can be used (Xi *et al.*, 2018). These experiments reveal that cells exhibit complex viscoelastic behavior at different levels of deformation and different regions of the cytoskeleton (Mofrad, 2009). The response of tissues to stretching can vary depending on the timescale of the stretch and the reorganization of cells within the tissue (Guillot and Lecuit, 2013). Rheological experiments also help to uncover the role of signaling pathways, such as YAP transcription factors, in mechanosensation (Wagh *et al.*, 2021).

The microfluidic system, also known as “cells on a chip,” has emerged as a valuable tool for investigating cell behavior under controlled biophysical conditions that mimic *in vivo* conditions (Ingber, 2018). This system allows for the application of stretch or shear forces, as well as the creation of a controlled microenvironment that mimics the organ-level cues present in the body. For instance, the surface tension at the air-liquid interface in the lungs and the fluid flow through the vasculature, as well as the cyclic mechanical stretch of the tissue-tissue interface due to breathing, can be replicated using this approach (Huh *et al.*, 2010).

In the context of developmental biology, the use of microfluidic systems has allowed for the study of self-organization and embryo functions under controlled physical conditions. The co-culture of iPSC-derived motoneurons and brain microvascular endothelial cells in a microfluidic system has produced the *in vivo*-like maturation of spinal cord neural tissue, representing a new avenue for exploring the complex interplay between physical and biological factors in development (Samal *et al.*, 2019, Sances *et al.*, 2018).

As mentioned earlier, the tissue-matrix interaction plays a critical role in sensing and rapidly transmitting forces (Serra-Picamal *et al.*, 2012, Sunyer *et al.*, 2016, Tambe *et al.*, 2011). However, in early embryonic epithelia where little or no ECM is present, stresses generated by actomyosin contraction of the cells in one tissue are transmitted over long ranges via intercellular adhesions to other tissues. Thus, studying a simple free-standing epithelial monolayer is very appealing in terms of characterizing the mechanical response to stretch at different time scales.

Only two techniques are available for this: first, Harris and colleagues created

a suspended monolayer by culturing a cell monolayer on a collagen matrix on two rods, and later removed the matrix using enzymatic digestion (Harris *et al.*, 2012). Second, epithelial domes, where MDCK cells pump ions to form fluid-filled blisters, have been used (Lever, 1979). Recently, my colleagues, Ernest Latorre and Ariadna Marín-Llaurado, have enhanced control over the curvature, shape, and size of the domes (Latorre *et al.*, 2018, Marín-Llauradó *et al.*, 2022), details on this system in the next chapter. These experiments showed that elasticity measurements of the monolayer were two orders of magnitude larger than those of individual cellular parts, and the monolayer could sustain more than 200% strain before the rupture of cell-cell junctions. The cell cytoskeleton, particularly the actomyosin network and cadherin junctions, actively remodel during stretching, while the keratin network reinforces monolayer integrity at higher strains (Duque *et al.*, 2023, Latorre *et al.*, 2018). With sustained stretching, the tissue undergoes significant realignment and rearrangement via division (Wyatt *et al.*, 2015). Experiments on tissue devoid of the matrix also revealed epithelial actions such as superelasticity and buckling (Latorre *et al.*, 2018, Wyatt *et al.*, 2020).

### 2.3.4 3D systems

*In vitro* experiments with 2D cell systems have improved our understanding of cell mechanics in morphogenesis by allowing us to measure deformations and forces and control environmental conditions that are inaccessible *in vivo*. However, to gain a deeper understanding of cell mechanics, systems closer to the *in vivo* environment must be probed.

Cell aggregates are a promising *in vitro* system for probing cell mechanics, where synthetic matrix and mechanical measurement tools can be used. The response of cell clusters to the matrix, while similar to planar tissues, is more complex and includes sensitivity to matrix stiffness, confinement, and ECM concentration, as well as the ability to undergo 3D shape transformations (see Fig. 2.3 E). Our lab has demonstrated that cell aggregates perform durotaxis and exhibit wetting behavior dependent on stiffness (Pallarès *et al.*, 2022, Pérez-González *et al.*, 2019). Additionally, cell aggregates in suspension behave like viscous droplets and can be used to measure rheological properties, such as when squeezed between plates or probed with AFM or a micropipette (Xi *et al.*, 2018). The viscoelastic properties of cell aggregates can even be measured by coalescing two aggregates (Oriola *et al.*, 2022).

In recent years, the use of hydrogel systems for the culturing cell aggregates

has gained significant attention. Hydrogels, such as polyethylene glycol (PEG), polyacrylamide, collagen, or Matrigel, serve as a supportive environment for cell growth. Naturally extracted hydrogels like Matrigel provide a similar architecture to the native ECM. When embedded into a hydrogel, polarized epithelia tend to form a spherical structure with a hollow lumen, which can be induced to form branching morphogenesis by hepatocyte growth factor (Bryant and Mostov, 2008).

Cell-driven self-assembly in organoids leads to tissue formation that mimics organ features, but achieving reproducibility in shape and composition is often challenging (Hofer and Lutolf, 2021, Nelson *et al.*, 2008). Synthetic hydrogels with control over ligand presentation, crosslinking, and degradability have proven useful for epithelial organoids, allowing for control over cell fate (Gjorevski *et al.*, 2022, 2016).

3D gel-based culture systems with spatiotemporal control over the mechanical properties corresponding to *in vivo*-like functional structures have also been developed (Torras *et al.*, 2018). Interestingly, recent publications show tissue transformation from planar to complex organ-resembling tissue without fine environmental control. For example, intestinal epithelium mechanically compartmentalizes itself, and 2D stem cells transform into a 3D neural tube (Karzbrun *et al.*, 2021, Pérez-González *et al.*, 2021).

In developing embryos, both embryonic and extraembryonic fluids generate frictional and tensional stresses when flowing, or hydrostatic pressures when confined within spaces (Chan and Hiiragi, 2020, Vianello and Lutolf, 2019). The challenge of measuring these forces has led to the use of various techniques, including micropipette aspiration. Micropipette experiments, where a needle is inserted into the embryo to control pressure, have revealed that the internal hydrostatic pressure determines the embryonic size and dictates cell fate allocation (Chan *et al.*, 2019) (see Fig. 2.3 E). As a fluid-filled structure, the hydrostatic pressure inside the embryo corresponds to tension in its surfaces, and changes in luminal volumes are sensed by cells through increased cortical tension, inducing changes in cell shape and cytoskeleton organization (Chan *et al.*, 2019, Choudhury *et al.*, 2022b). Micropipette aspiration has also been effective in measuring the surface tension of individual cells or whole blastomeres (Dumortier *et al.*, 2019), thus providing insight into the role of the actin cortex in regulating preimplantation embryonic contractility (Firmin *et al.*, 2022, Özgürç *et al.*, 2022).

The measurement of forces within embryos has also been approached through the insertion of deformable probes, such as hydrogels, oil, or magnetic droplets (Campàs

*et al.*, 2014, Dolega *et al.*, 2017, Serwane *et al.*, 2017). The shape changes of these probes allow for measurement of local forces and osmotic pressures (Mongera *et al.*, 2023).

In addition to embryos, explant systems have been utilized to study organogenesis in the brain, gut, and lungs. Lung explant research has been particularly useful in understanding different aspects of shape formation, which occurs under the influence of pressure and growth factors. The explant system allows for direct control over the chemical and mechanical environment at specific stages of development. Work with mouse airway epithelium has shown that pressure and matrix stiffness impact the number of lung branches (Nelson *et al.*, 2017, Palmer *et al.*, 2021, Varner *et al.*, 2015).

Other tools such as optical tweezers, laser ablation, and optogenetic excitations have been used at different levels to probe the mechanics of development (Gómez-González *et al.*, 2020, Lecuit *et al.*, 2011). However, independent control over multiple factors remains difficult and force measurement remains indirect.

In conclusion, epithelial tissues are highly sensitive to various biophysical forces and constantly undergo remodeling at different scales and timeframes. There are multiple techniques available to manipulate and study these tissues, from single cells to embryos, with controlled forces and deformation. Due to its dynamic behavior, epithelial tissue can be considered an active material. The focus of this thesis is to develop a system that can control and measure physical forces to understand epithelial behavior as an active material. In the following chapter, we will delve into the molecular machinery responsible for driving these active tissues.

# **Chapter 3**

## **Active tissue mechanics**

### **3.1 Force generation with actin**

In the field of morphogenesis, cells are central to the formation of specific structures through changes in their shape. Early embryologists posited the existence of a mysterious external vital force that guides the morphogenesis of individual cells in tissues (Thompson, 1979). However, as research progressed, particularly experiments by Wilhelm His and Wilhelm Roux, it became clear that the physical forces generated within the cell itself (Clarke and Martin, 2021). In the present day, we now understand, what was unknowable in the XIXth century, that the machinery responsible for generating these physical forces is the actin cytoskeleton.

Specifically, the actomyosin cortex forms a mesh containing actin filaments and myosin motors just beneath the plasma membrane of a cell (Alberts, 2015). This mesh is organized into various higher-order arrays capable of dynamic remodeling, giving rise to the complex shapes and structures we observe in the world around us. We can understand the actomyosin cortex step by step, starting from its basic organization of single actin filaments to higher-order supracellular actomyosin cables.

#### **3.1.1 Actin filaments**

The actin filaments are helical polymers composed of G-actin proteins (see Fig. 3.1 A). The asymmetrical nature of these proteins leads to the development of two distinct ends, referred to as the barbed and pointed ends, that can be differentiated based on their appearance in electron micrographs. The actin filaments are known for their

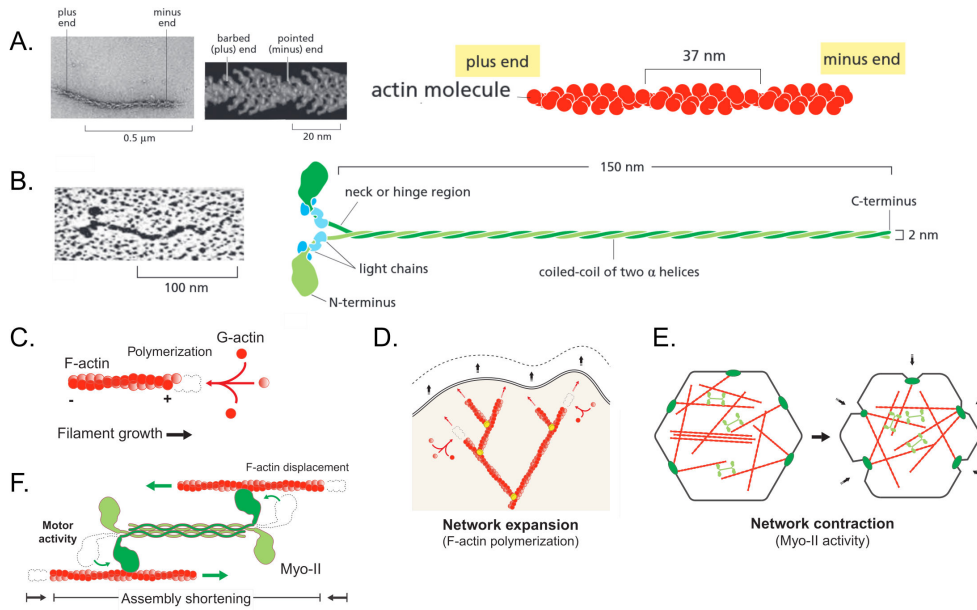


**Figure 3.1: Actin and Myosin:** (A) Electron micrograph of Actin filament with zoomed in images of barbed and pointed end. (B) Same for Myosin II minifilament with clearly visible two globular heads and a long tail. (C-D) Actin network can apply pushing force through polymerization of single filaments or network expansion. (E,F) While myosin activity would lead to contraction of the networks. *Adapted from A-B (Alberts, 2015) and C-F (Clarke and Martin, 2021)*

dynamic assembly and disassembly processes, where the distinct ends have different rates of kinetics. This results in growth in the direction of the barbed end, with the length of the filament can be maintained by a constant flux of subunits from the pool of monomers in the cell and nucleotide hydrolysis. This process is referred to as *treadmilling* (see Fig. 3.2 A). However, if one end of the filament is capped, it will continue to grow and apply a pushing force in the outward direction.

### 3.1.2 Actin networks

Actin filaments can also form branched networks, facilitated by the presence of nucleation sites on the filament and proteins containing actin-binding motifs. The actin nucleation can be catalyzed by two primary factors, the ARP 2/3 complex or formins. The ARP 2/3 complex creates a pointed end in the center of a filament, leading to the formation of a new branch from that site. This results in the formation

of a tree-like network of branches, capable of generating sufficient pushing forces to move a part of the cell membrane (see Fig. 3.2 E,F). The formins, in conjunction with profilin, aid in the growth of the filaments, with profilin serving as a staging area for the rapid addition of monomers to the filament. These structures can take the form of dendritic actin networks that enable membrane protrusion at lamellipodia or spike-like projections of the plasma membrane that allow a cell to explore its environment (see Fig. 3.2 C). The pushing forces generated at the molecular level are of the order of 1 piconewton.

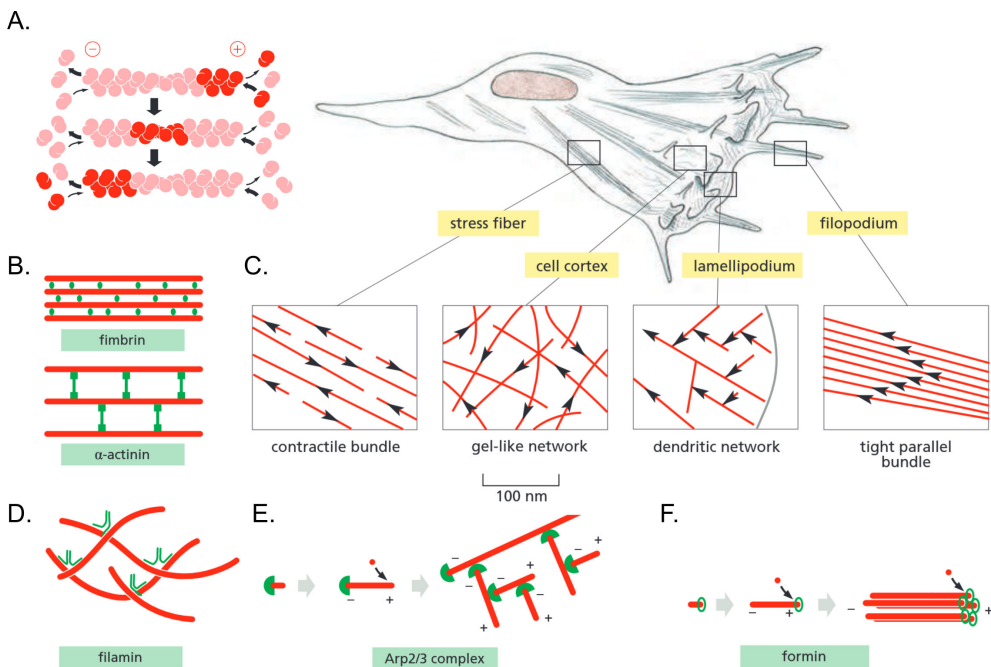


**Figure 3.2: Forms of actin networks:** (A) Actin treadmilling: where highlighted actins move from positive end to negative end as the filament polymerizes and depolymerizes from both ends. (C) In an adherent cells, there are many different kinds of actin structures from contractile network to gel-like cortex. (B,D,E,F) Actin structures can be thought as meshwork of actin filaments (red) with crosslinkers(green). Different crosslinkers produce distinct form of actin network. *Adapted from (Alberts, 2015)*

### 3.1.3 Actin cortex

The actin filaments can also form tight or loose bundles, facilitated by crosslinking proteins. Fimbrins enable multiple actin filaments to arrange in parallel, resulting in closely packed bundles that exclude myosin from connecting to the filaments. On the other hand,  $\alpha$ -actinin crosslinks actin filaments with opposite polarity into a loose bundle, allowing myosin to bind and create contractile bundles (see Fig. 3.2 B). Myosin II oligomerizes into a bipolar short filament that can connect multiple actin filaments and move across them, resulting in a pulling effect (see Fig. 3.1 B). This movement is driven by ATP hydrolysis making contracting an active process. The loose bundle forms the gel-like network in the cell cortex. Other actin crosslinking proteins can result in different structures. Filamin creates a loose and viscous gel that is essential for migration, while spectrin creates a strong and flexible web-like network of short actin filaments that allows cells to reversibly deform (see Fig. 3.2 D). The actomyosin bundles in the cortex can generate two orders of magnitude more force than a single filament (Clarke and Martin, 2021).

## 3.2 Actin structures at a larger scale

During epithelial morphogenesis, individual cells can undergo shape changes by modifying their contractility or actin turnover, resulting in the development of tissue curvature. As mentioned previously, epithelial cells exhibit apicobasal polarity, which results in a non-uniform distribution of the actin cytoskeleton that influences cell shape and tissue architecture.

The geometry of columnar or wedge-like cells in a monolayer determines the specific ways in which they can be organized (Gómez-Gálvez *et al.*, 2021). Columnar cells, when arranged together, produce a flat tissue, while wedge-shaped cells with a narrow top result in convex curvature (see Fig. 3.3 A). Conversely, concave curvature with a narrow bottom can also be created. By observing the actin cytoskeleton, we can determine the specific mechanisms of tissue shaping (see Fig. 3.3 B). For example, apical constriction with concentrated actin cortex on the apical surface is involved in multiple convexly curved tissues, such as the invagination of the intestinal crypt, the Drosophila mesoderm, and the vertebrate lens placode (Houssin *et al.*, 2020, Lecuit *et al.*, 2011, Pérez-González *et al.*, 2021).

On the other hand, basal constriction results in opposite curvature, as observed in the optic cup and mid-hind brain fold of zebrafish (Gutzman *et al.*, 2018, Sidhaye

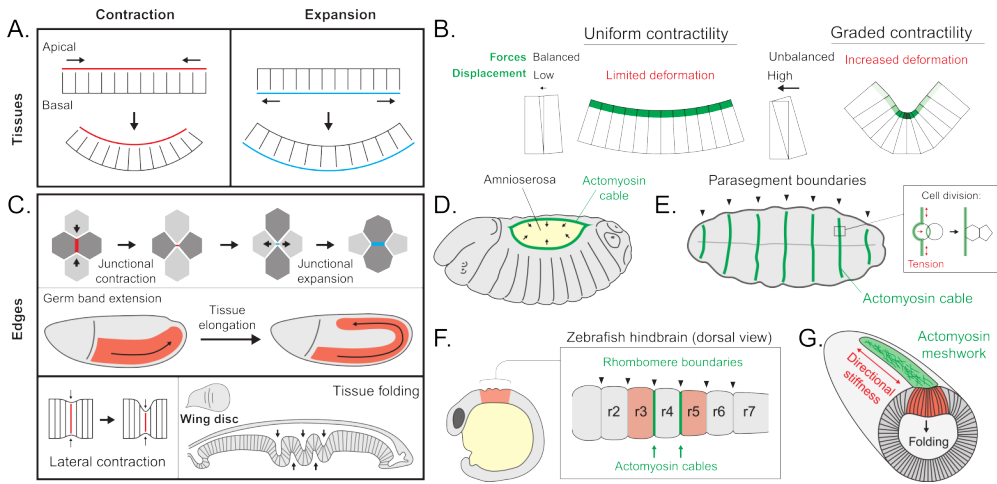


**Figure 3.3: Morphogenesis driven by actin at tissue scale:** (A) Apical contraction or basal relaxation both results in the same curvature. (B) However, amount of deformation will depend on the contractility gradient. (C) Lateral surface of cells can also undergo expansion or contraction leading to cell rearrangements or tissue folding. (D-G) Supracellular actin cables plays vital role in creating boundaries or causing large scale deformations. Adapted from (Clarke and Martin, 2021)

and Norden, 2017). However, convex curvature can also be produced through basal expansion, as seen in the Drosophila wing disc (see Fig. 3.3 A). Certain parts of the wing disc can locally relax the basal side without affecting the apical side, leading to basal expansion (Sui *et al.*, 2018). In addition to the apical and basal surfaces, lateral surfaces can also contract or expand due to myosin II activity, which can cause tissue folding in the wing and leg discs of Drosophila (Monier *et al.*, 2015, Sui *et al.*, 2018). Furthermore, cell-cell rearrangements can be produced by altering junction lengths during germ band extension (Collinet *et al.*, 2015, Yu and Fernandez-Gonzalez, 2016) (see Fig. 3.3 C).

Not only do individual cells undergo coordinated actin reorganization during epithelial morphogenesis, but supracellular actin structures can also emerge at the tissue level (see Fig. 3.4 A-C). Junctional actomyosin organizes to form bundles connected across multiple cells, allowing for important functions such as wound healing and morphogenesis (Brugués *et al.*, 2014, Clarke and Martin, 2021) (see Fig. 3.3 D-F). These supracellular networks can exert forces at the scale of the embryo, as observed in cases such as dorsal closure and parasegment boundary formation in Drosophila and epiboly in zebrafish (Calzolari *et al.*, 2014, Ducuing and Vincent, 2016).

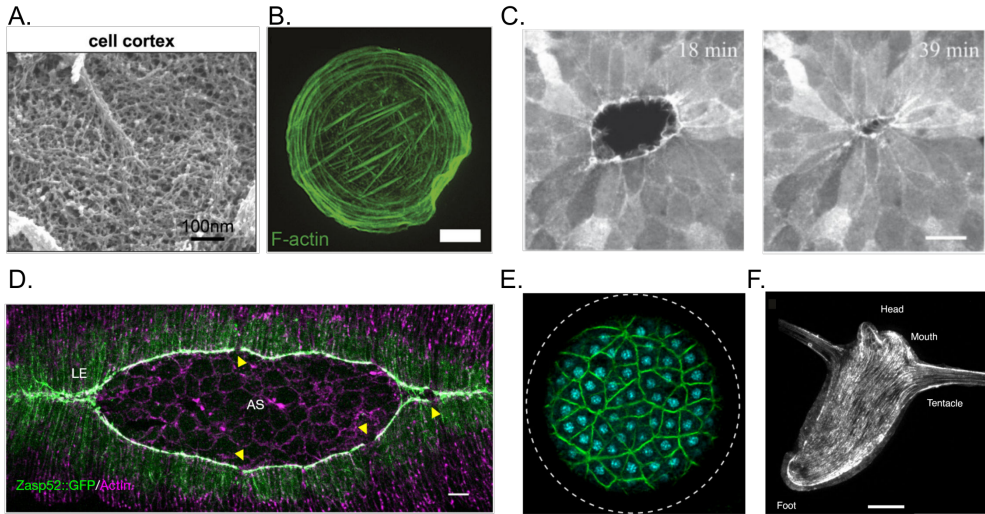


**Figure 3.4: Actin organization at different scales:**(A) Electron micrograph of actin cortex of mitotic Hela cells (Kelkar *et al.*, 2020). (B) Different forms of actin organization in circular fibroblast cell (Jalal *et al.*, 2019) Scale= 10 $\mu$ m. (C) Supracellular actin ring during wound closure (Brugués *et al.*, 2014) Scale= 20 $\mu$ m. (D) Dorsal closure of amnioserosa with actin network (Ducuing and Vincent, 2016) Scale= 10 $\mu$ m. (E) Supra-cellular organization of actin for cellularization of coenocyte. Circle is 60 $\mu$ m (Dudin *et al.*, 2019). (F) Hydra with actin network, whose nematic defects determines morphogenesis (Maroudas-Sacks *et al.*, 2021) Scale= 100 $\mu$ m.

Additionally, these networks can alter the material properties of specific regions in the embryo, making them more prone to deformation and thus aiding in the formation of folds or invaginations (see Fig. 3.3 G).

During Drosophila gastrulation, tissue-level actin cortex is altered in the direction of the anterior-posterior axis, providing increased bending strength in that direction. This supports the internalization of the mesoderm by promoting folding in a perpendicular direction (Yevick *et al.*, 2019). Interestingly, highly organized actin bundles are also found in even larger systems such as Hydra, vertebrate smooth muscle, and the heart (Cetera *et al.*, 2014, Helm *et al.*, 2005, Maroudas-Sacks *et al.*, 2021, Palmer *et al.*, 2021) (see Fig. 3.4 D-F). These bundles assist in generating mechanical force patterns that create coordinated tissue movements at a global scale.

### 3.3 Timescales of the actin cytoskeleton

Morphogenesis, the process of shaping and forming living structures, occurs at varying timescales and requires the cell cytoskeleton to change its shape accordingly. Rheological and mechanobiological experiments have given us insights into how cells respond to forces and deformations based on their magnitude and rate (see Fig. 3.5; reviewed in (Wyatt *et al.*, 2016)).

For fast deformations (in the range of milliseconds to seconds), cells exhibit predominantly elastic behavior, as there is insufficient time for the actin cortex to respond or remodel (Deng *et al.*, 2006). The cytoskeleton can store elastic energy and release it. At this scale, there is also flow of cytosol through the cortical mesh, resulting in poroelastic behavior (Moeendarbary *et al.*, 2013).

When forces or deformations are applied over longer timescales (seconds to minutes), cells exhibit an increasingly viscoelastic behavior (Kollmannsberger and Fabry, 2011). The actin cortex can flow and is unable to fully store energy. The actin filaments and crosslinkers, such as myosins and actinin, allow the cytoskeleton to remodel in response to mechanical perturbations through turnover in tens of seconds or a few seconds, respectively. Myosin mini filaments, however, can take longer to remodel, up to hundreds of seconds.

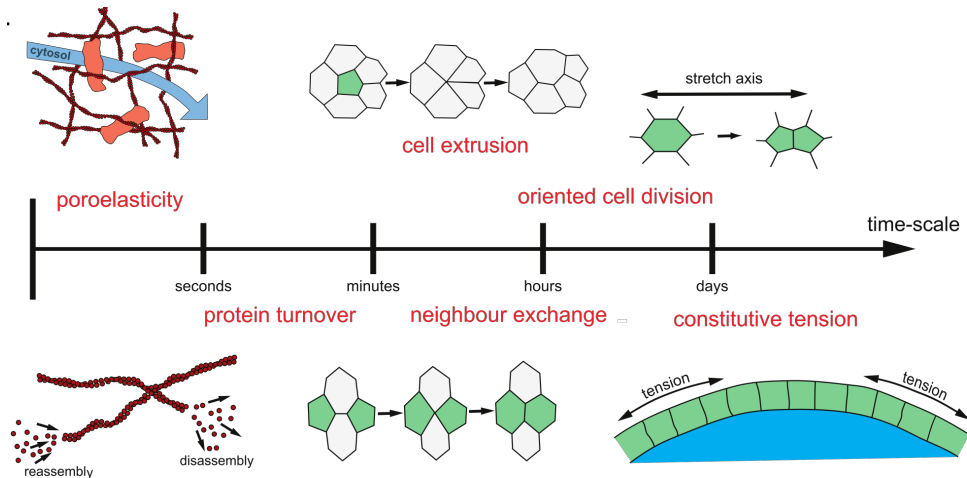


**Figure 3.5: Timescale of actin network related processes:** Timescales of different actin driven cellular processes, ranging from cytoskeletal fluid deformation to large-scale tissue deformations. Adapted from (Kelkar *et al.*, 2020).

At even longer timescales (minutes to hours), cells or tissues may respond through oriented division or rearrangement, allowing them to adapt to persistent forces such as gravity or surface tension. Tissues may resemble a viscous fluid and morph into a sphere, such as a blastocyst. Interactions with the extracellular matrix over hours can lead to adjustments in the constitutive tension of tissues based on biophysical and biochemical forces (Porazinski *et al.*, 2015).

### 3.4 Modeling active tissue dynamics

The advancement of molecular biology and tissue dynamics has increased our understanding of morphogenesis. However, it is becoming increasingly crucial to interpret biological experiments through theoretical models in order to generate new hypotheses and validate them through further experimentation.

Mathematical models at multiple scales are used to describe both physics and biology. At larger tissue scales, hyperelastic continuum material models could be utilized to describe the behavior of the cardiovascular system (Holzapfel *et al.*, 2019). On smaller scales, agent-based models are used to explain epithelial tissue behavior in terms of cell sorting and reorganization (Voss-Böhme, 2012). This section aims to provide the reader with a brief overview of the relevant modeling approaches in this field.

#### 3.4.1 Vertex models

D'Arcy Thompson, in his chapter on "The Forms of Tissues," presents an intuitive argument regarding the role of surface tension or capillarity in organizing cells into a tissue (Graner and Riveline, 2017, Thompson, 1979). He observed this phenomenon in a wide range of biological systems, from two connected cells to the organization of cells in a dragonfly wing, which resemble the associations of soap bubbles or foams (see Fig. 3.6).<sup>1</sup> In the case of monolayered epithelial tissue, its polygonal cellular pattern on its surface enables the easy description and tracking of cell motion and shape change through the use of vertices and edges.

---

<sup>1</sup>"we recognize the appearance of a "froth," precisely resembling that which we can construct by imprisoning a mass of soap-bubbles in a narrow vessel with flat sides of glass; in both cases we see the cell-walls everywhere meeting, by threes, at angles of 120 deg, irrespective of the size of the individual cells: whose relative size, on the other hand, determines the curvature of the partition-walls", writes Thompson

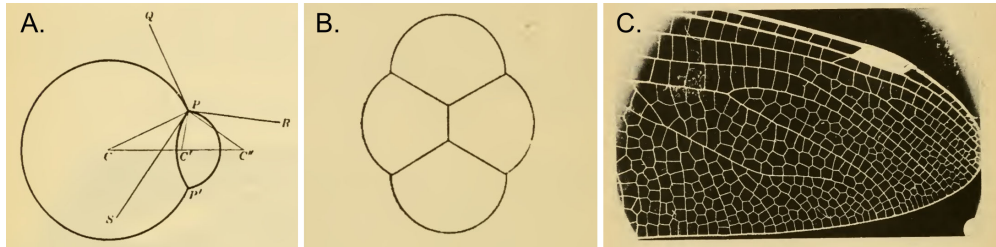


**Figure 3.6: D'Arcy Thompson's forms of tissues:** (A-B) Thompson equates cell aggregates to coalescence of bubbles like in a froth. (C) A dragon fly wing is a clear example of this organization. *Adapted from (Thompson, 1979)*

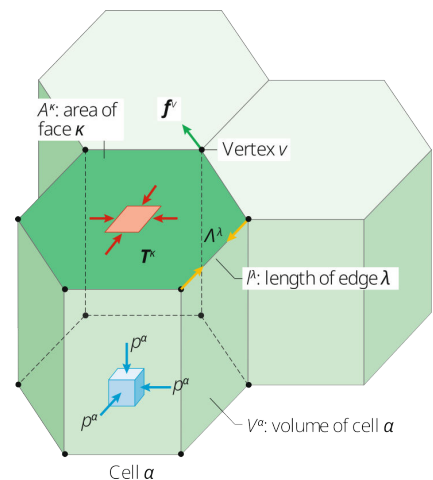
Vertex models have proven to be valuable in understanding the complex interactions between cellular shape, the forces generated within epithelial cells, and the mechanical constraints imposed on the tissue from external sources (as reviewed in (Alt *et al.*, 2017)). These models can be two-dimensional or three-dimensional, depending on the system being modeled, but cells are consistently defined as having both an apical and basal surface, as well as lateral interfaces between neighbors. Further complexities have been added to describe specific systems, such as intercalations in three-dimensional epithelia, through the use of a geometric shape known as the Scutoid (reviewed in (Gómez-Gálvez *et al.*, 2021)).

To determine the motion of the vertex, mechanics must be specified. It is often done using the virtual work function ( $W$ ). There are two components: internal ( $\delta W_i$ ) and external ( $\delta W_e$ ).

$$\delta W = \delta W_i + \delta W_e.$$

The changes in internal virtual work, ( $\delta W_i$ ) can result from changes in the cell volumes ( $\delta V$ ), in the areas of surfaces ( $\delta A$ ), or in the lengths of bonds ( $\delta l$ ). By defining the cell pressure ( $P$ ), the surface tension ( $T$ ), the line tensions ( $\Lambda$ ), and internal dissipative forces ( $f_i$ ), the differential of the internal virtual work for vertex movements

**Figure 3.7: Vertex model for cells in a monolayer** *Adapted from (Gómez-González *et al.*, 2020).*



can be written.

$$\delta W_i = \sum_{cell} \alpha (-P^\alpha \delta V^\alpha) + \sum_{surface} k (T^k \delta A^k) + \sum_{edge} \lambda (\Lambda^\lambda \delta l^\lambda) - \sum_{vertex} v (f_i^v \delta x^v).$$

Similarly, the external virtual work, ( $\delta W_e$ ), can be written according to the external forces ( $f_e$ ) that come from external mechanical forces applied to the tissue through the matrix, or fluid pressure acting on apical or basal cell surfaces.

$$\delta W_e = -\sum_{vertex} v (f_e^v \delta x^v).$$

The state of a monolayer is determined by minimizing the virtual work function, taking into account the molecular complexities that contribute to surface tension and line tensions. In the context of epithelial layers, the actin cortex significantly impacts the tensions along the edges. Vertex model simulations in 2D models demonstrate the important role of interfacial tensions in shaping cell orientation, coordinating collective migration, and facilitating tissue rearrangement through cell division.

In contrast, 3D models capture the physics of various morphogenetic processes, such as the formation of appendages on the drosophila eggshell and the mechanical compartmentalization of intestinal epithelia (Osterfield *et al.*, 2017, Pérez-González *et al.*, 2021). These models offer unique insights into cell packing and the transition between jamming and unjamming (Park *et al.*, 2015, Tang *et al.*, 2022). In some cases, phase transitions from a solid to fluid state result from localized proliferation and oriented divisions, showing that the epithelial tissue behaves as an active material (reviewed in (Lenne and Trivedi, 2022)).

### 3.4.2 Continuum models

The viscoelastic properties of tissues are captured in vertex models, which are useful for smaller scale. However, for larger scale deformations or flows, we can model tissues as a continuous material. There are two tactics for thinking about these models: one focuses on the rheological properties of the tissue, and the other on shape transformations. By thinking of a continuous sheet of cells as an active surface, we can capture the physics of single cells to embryos (Khoromskaia and Salbreux, 2023, Salbreux and Jülicher, 2017).

Continuum models focus on developing reliable constitutive relations and solving initial-boundary-value problems. Constitutive relations describe how materials respond to applied loads, and they depend on the internal constitution of the material.

Determining constitutive relations for epithelial monolayers can be challenging because these tissues are much more complex than simple metals or passive polymers (see Fig. 3.8 A-B). However, their complex material behavior can be understood by characterizing their mechanical response using standard material testing techniques (Humphrey, 2002). Typically, they can be probed mechanically in a biologically relevant manner, such as through biaxial or uniaxial stretching experiments that simulate *in vivo* tissue behavior (Humphrey *et al.*, 2014). These experiments with epithelial tissues have revealed the viscoelastic nature of these materials (Harris *et al.*, 2012, Khalilgharibi *et al.*, 2019).

Solids, such as rubber, are considered to have elastic properties, allowing them to deform reversibly when subjected to a force. Conversely, fluids are characterized by their viscosity, meaning they flow in response to an applied force. Viscoelastic materials exhibit both solid-like and fluid-like behaviors (see Fig. 3.8 C). Simple models can represent these behaviors by combining elastic components, represented as springs, and viscous components, represented as dashpots. The elastic response does not dissipate energy, unlike the viscous response.

$$\sigma = E\epsilon, \quad \sigma = \eta \frac{d\gamma}{dt}.$$

Other material properties like stiffness or Poisson's ratio can be revealed through quasi-static stretching or compression. However, dynamic properties are better understood through frequency sweep, creep, or stress relaxation experiments (Guimarães *et al.*, 2020). Rheological experiments have been extremely valuable in gaining insight into the mechanical response of various biological materials, ranging from reconstituted cytoskeletal proteins to large multicellular aggregates (Cavanaugh *et al.*, 2020, Mofrad, 2009, Xi *et al.*, 2018).

Rheological properties are often linked to physiological state and are crucial for their specific functions (Park *et al.*, 2015, Vedula *et al.*, 2012). For example, many fundamental shape transitions in embryos occur through abrupt change in tissue material properties (Hannezo and Heisenberg, 2022). Therefore, it is important to assess rheological properties in different microenvironments. Mechanical information such as deformation, deformation rates or velocity fields, traction forces exerted by cells on substrates, and intercellular mechanical stress can provide a more complete picture of tissue rheology when combined with information about cellular architecture obtained through imaging (Roca-Cusachs *et al.*, 2017). These types of experiments

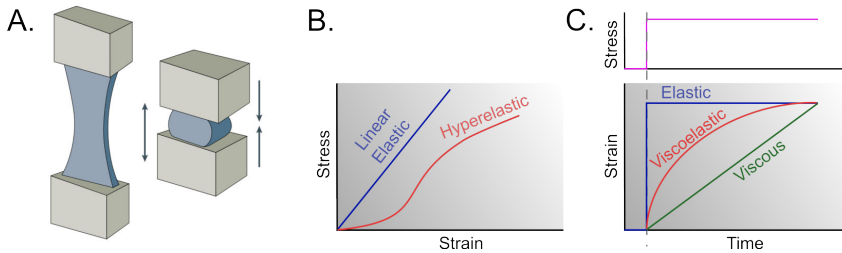


**Figure 3.8: Stress strain behavior of materials:** (A) materials being stretched or compressed. (B) Quasistatic deformations yield stress-strain curves. (C) Creep test where strain response is characterized at constant stress.

shed light on the complex mechanisms of strain stiffening and viscoelastic behavior at different deformation regimes involving various parts of the cytoskeleton.

One general feature of most biological tissues is their softness, and hence the fact that they undergo large deformations. However, linear elasticity is valid for infinitesimally small deformations. To account for such large deformations, geometrically exact continuum mechanics descriptions have been applied to a variety of systems including cardiovascular mechanics or the growth of organs. In this approach, deformation is described by a function  $x = \chi(X, t)$  mapping a reference to a deformed configuration. The deformation gradient and Green's strain tensor (nonlinear in the deformation) are defined as

$$F = \nabla_X \chi(X, t); \quad E = \frac{1}{2}(F^T F - I).$$

Based on these deformation measures, hyperelasticity is based on defining a strain energy function  $W(E)$  from which elastic stresses can be computed as  $S = \partial W / \partial E$ .

The use of hyperelastic models has proven to be effective in capturing the material response in various biological tissues, such as the bladder, heart tissue, skin, and arteries (Holzapfel, 2000). This type of formulation provides a degree of flexibility, as it allows for the inclusion of additional physical constraints, such as the anisotropy of the tissue microstructure or its incompressibility. Minor modifications to these constitutive relations can be used to capture the material response, such as explaining the phenomenon of strain stiffening, or accounting for the inhomogeneity in the material, such as the collagen content and crosslinking in the tissue (Holzapfel *et al.*, 2019).

These models are also employed in the understanding of growth and remodel-

ing, by expanding the framework of hyperelasticity through the use of kinematical growth theory (Ambrosi *et al.*, 2019). In such theories, the deformation gradient is decomposed into elastic and growth components  $F = F_e F_g$ , with the stress depending on the elastic part of the deformation gradient and  $F_g$  being determined by a growth law. This theory highlights the existence of residual stresses in growing tissues, leading to a modification of the tissue properties into a spatially inhomogeneous and anisotropic states. This process is of great significance in the field of solid tumor growth mechanobiology, as the residual stresses directly impact tumor aggressiveness, nutrient pathways, necrosis, and angiogenesis.

### 3.4.3 Active surface models

At the cellular level, the mechanical properties of tissues are largely determined by the biopolymeric cytoskeleton, which consists of filaments and cross-linkers and molecular motors. These components continuously convert energy, ATP to ADP, through contractions or extensions of the network, resulting in a physical gel-like system due to its cross-linked actin filament network. However, the presence of phenomena such as treadmilling, active polymerization-depolymerization of filaments, and the mobility of molecular motors, such as myosin, makes the tissue system an active gel that lacks time-reversal symmetry due to its continuous energy transduction.

Additionally, the filaments are polar, which allows for the acquisition of orientational order. This has led to the modeling of tissues as active gels, similar to modeling active systems, such as flocks of birds and schools of fish, using hydrodynamics of active matter (Jülicher *et al.*, 2018). Active matter systems are a subclass of continuum models used to describe the dynamics of packed active particles, which are based on the liquid crystal theories of soft condensed matter. Like liquid crystals, cells also possess orientation and the ability to move past each other. In this framework, the orientation of filaments in the cytoskeleton or the elongation of cells in the tissue can be characterized by a nematic order parameter matrix (see Fig. 3.9).

$$Q = \frac{3S}{2} \left( n \otimes n - \frac{I}{3} \right), \quad S = [\cos 2\theta],$$

$$\sigma_{active} = \zeta Q.$$

The utilization of this formulation is significant in characterizing the active forces produced by the network. The stress is separated into two components: active and

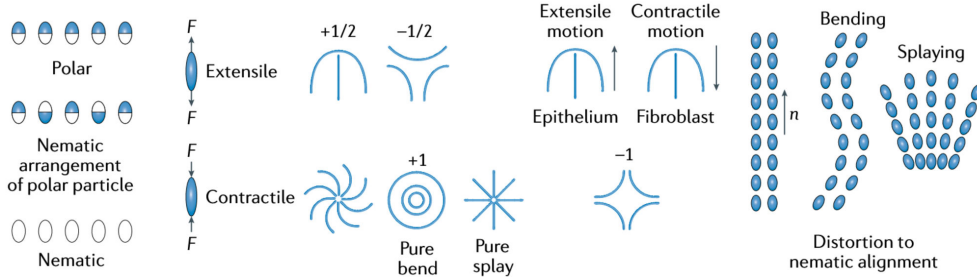


**Figure 3.9: Active nematics:** Schematics of (A) nematic or polar particles, (B) extensile and contractile force dipoles, (C) Various types of defects and related motion of cells *Adapted from (Xi et al., 2018)*.

passive. The passive stress arises from the viscoelasticity of the material and the bending, splaying, and twisting of the aligned elements. The active stress, on the other hand, is calculated by combining the strength of activity, represented by the parameter zeta, and the nematic order matrix. The sign of zeta determines the type of force dipole generated; a negative sign results in contraction of the system, while a positive sign leads to expansion along the nematic axis.

The active stress plays a crucial role in the motion of the system and can result in chaotic motion even in low Reynolds number systems, as evidenced in dense bacterial systems of *Bacillus subtilis* where jet flows and turbulent patterns have been observed, as well as in expanding monolayers where independent vortices have been recorded (Blanch-Mercader *et al.*, 2018, Wensink *et al.*, 2012). The nematic formulation have proven to be effective in capturing the physics of 2D confined systems and expanding systems (reviewed in (Saw *et al.*, 2018)).

In the context of 3D models, active surfaces are used to describe the actomyosin cortex near cell membranes or epithelium in embryos (Salbreux and Jülicher, 2017). This thin sheet of matter generates internal forces and torques that drive shape changes at the cellular or tissue level. The resulting three-dimensional structures can be conceptualized as curved, active two-dimensional surfaces. Forces and torques can be defined in terms of tension ( $t$ ) and moment ( $m$ ), and the model also considers the mirror and rotation symmetries of the surface elements (see Fig. 3.10).

Salbreux and Julicher's work has demonstrated that flat active membranes with up-down asymmetry exhibit stability dependent on active tension and active tension-curvature coupling term. This tension-curvature dependency has been observed in

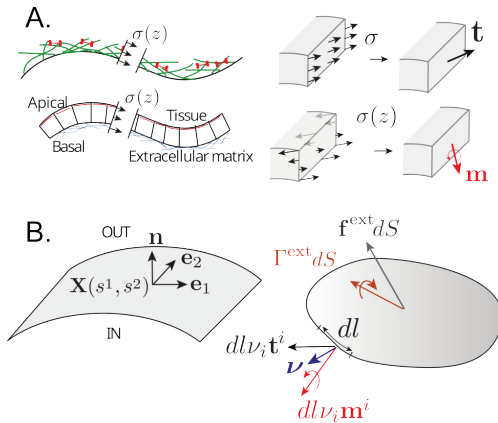


**Figure 3.10: Active surface models:** (A) Tissues or cell surfaces can be modeled as surface with stresses and torques along the thickness. (B) Internal and external forces act on a surface element. The kinematics of these surfaces, mathematical tools from differential geometry can be applied, using generalized coordinates ( $X$ ), metric tensor ( $g$ ), and curvature tensor ( $C$ ), where ( $dl$ ) is the length of the line element with tangential unit vector ( $v$ ). Adapted from (Salbreux and Jülicher, 2017)

the pancreas of mice, where the morphology of epithelial tumors is determined by the interplay of cytoskeletal changes in transformed cells and the existing tubular geometry (Messal *et al.*, 2019). Specifically, small pancreatic ducts produced exophytic growth, whereas large ducts deformed endophytically, consistent with theoretical predictions. Another example shows that curls of high curvature form spontaneously at the free edge of suspended epithelial monolayers, which originate from an enrichment of myosin in the basal domain that generates an active spontaneous curvature (Fouchard *et al.*, 2020). The extent of curling is controlled by the interplay between internal stresses in the monolayer.

While the molecular level behind epithelial morphogenesis, specifically the actin cytoskeleton, is well understood, there are still gaps in the theoretical and experimental framework that can bridge the gap between molecular dynamics and tissue-scale deformations. Vertex and continuum models have been developed to capture the physics of morphogenesis at the tissue scale, and phenomenological experiments provide insights into the constitutive relations of cytoskeletal components and tissues in specific conditions. However, combining vertex models and active surface mechanics could provide finer control over individual cell surfaces, enabling more precise bottom-up morphogenesis.



# **Chapter 4**

## **Bottom up morphogenesis**

### **4.1 Learn by building**

The mechanics and biology of epithelial tissues are complex, with mechano-chemical signaling and multiscale behavior all intertwined. The lens of active material has been instrumental in illuminating the role of molecular elements in undergoing shape changes during morphogenesis. Mechanistic understanding has been enhanced with new mathematical tools and advanced microscopy, enabling measurement of the forces involved in tissues.

The traditional and successful method for studying mechanics has been to deconstruct the system one component or parameter at a time. By manipulating genes or disrupting cellular processes, we can observe how mechanics change. This perturbative method allows for the alteration of biological systems at various levels, from molecular to tissue, (see Fig. 4.1) .

However, studying systems like organoids or embryos can only provide limited physical insights into the topological transitions of these structures, as experimental systems have limited physical control and ability to measure forces. An alternative approach is to learn by actively performing morphogenesis or reconstructing biological structures from their basic components.

For years, researchers have broken down biological systems into approachable parts - tissues, cells, proteins - in order to understand the behavior of each component. However, combining existing knowledge of these parts to recreate novel experimental systems could reveal the basic building blocks and effects of scale. This approach would complement top-down approaches in developmental biology. Synthetic biology,

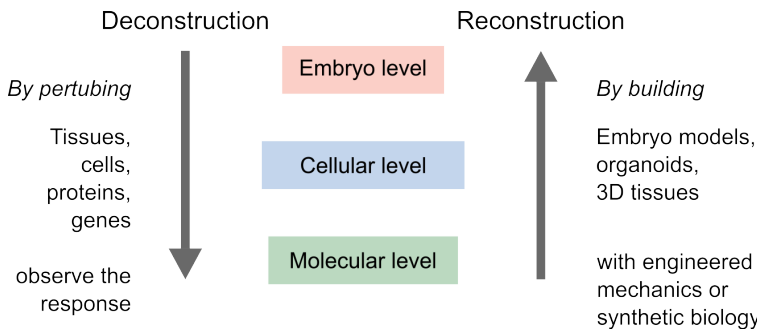


**Figure 4.1: A conceptual representation of two approaches to understanding mechanics: reconstruction (bottom-up) and deconstruction (top-down).** In reality, they are not separate from each other. These methods inform each other, with past top-down research guiding new reconstruction, and new engineered cells or tissues furthering our understanding of the field in innovative directions.

a perfect example of reconstruction, seeks to recreate life at various scales, from synthetic proteins to entire cells, in order to gain a deeper understanding of the indispensable components of life.

As active agents exist at every scale, emergent properties can appear at higher scales. Thus, it is essential to focus on higher scales or work with collectives of cells. This reminds me of the example of cars and traffic: Imagine you know the behavior of all individual car components, but this information is not sufficient to understand the behavior of traffic flow. This requires a higher level of analysis.<sup>1</sup> Similarly, biological structures exhibit numerous collective behaviors, such as jamming, nematic order, instabilities, or self-organization (Trepaut and Sahai, 2018).

Recreating structures from scratch also provides an opportunity to understand the role of physics at different scales. In the spirit of D'Arcy Thompson, we can explore the fundamental properties of matter in biological structures.<sup>2</sup> For instance, we can study the role of surface tension in guiding the shape of cellular aggregates or lumens.

<sup>1</sup>Matthew Good's commentary provides an insightful perspective on the complexity involved in building cells from interacting molecules. Meanwhile, Xavier Trepaut argues that a bottom-up approach does not fully explain the emergent behavior of higher-level structures and emphasizes the need for constructing tissues at the mesoscale. Trepaut uses the analogy of traffic jams to illustrate the importance of considering the collective behavior of cells in tissue engineering (Good and Trepaut, 2018).

<sup>2</sup>Thompson writes, "...to seek not for ends but for antecedents is the way of the physicists, who finds causes in what he has learned to recognize as fundamental properties, or inseparable concomitants, or unchanging laws, of matter and of energy." (Thompson, 1979)

In this work, we focus on the mesoscale structures of epithelia ( $\sim 10 - 10^4 \mu\text{m}$ ).

We present our efforts to engineer an epithelial structure with a controlled microenvironment that is sensitive to self-organization and mechanical instabilities. The following sections will describe the ways of creating these structures from minimal ingredients.

## 4.2 How to build tissue structures?

Before embarking on the construction of a tissue structure, it is important to consider the desired form and function. Despite the diversity in the shapes and functions of tissues, certain elementary shapes can be seen in many cases, resulting from the interplay between physical forces and biochemical signaling. Examples of such shapes include spherical blastocysts, ellipsoidal embryos, or cylindrical vessels.

After considering the desired form and function of the structure, established cell lines are selected and synthetic structures are constructed using various techniques, such as geometry control and localized folding, as discussed in the chapter 2.3. The resulting structures can be further studied to understand the interplay between physical forces and biochemical signaling, as well as their potential applications in various biological systems.

### 4.2.1 Controlling geometry and physical forces

From an engineering perspective, scaffolding is a commonly used approach for constructing synthetic epithelial structures. Scaffolds can be generated through 3D printing or microfabrication techniques, and cells can then be seeded onto the scaffold to attain the desired shape (Torras *et al.*, 2018). This method allows for the creation of a well-controlled microenvironment for the cells in terms of geometry, stiffness, adhesion proteins, and cell culture media (see Fig. 4.2 A) . Structures generated through this approach can be utilized to investigate tissue behavior in response to forces and curvature.

For instance, cells can be used to form a micro-vessel using a hydrogel with a cylindrical hole (Dessalles *et al.*, 2021). The hydrogel and cells were housed in a microfluidic device that controlled pressure and flow in the vessel, and the authors were able to examine the role of hydrogel poroelastic properties in regulating the dynamics of the vessel. Another exciting study demonstrated the potential of epithelial

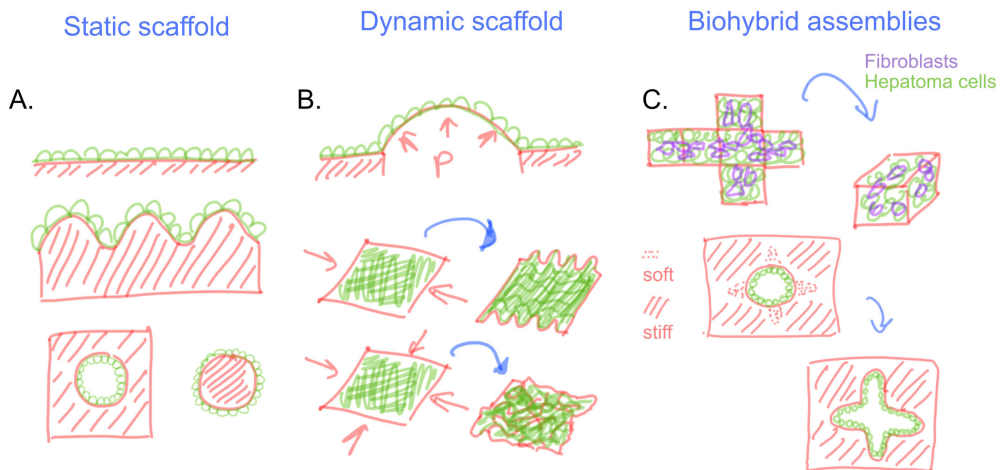


**Figure 4.2: Controlling geometry and physical forces:** The concept of scaffolding can be divided into two categories: static and dynamic scaffolds. (A) Static scaffolds are microfabricated structures that cells can adapt to and respond to geometrical cues, leading to the formation of a specific tissue organization (Brassard *et al.*, 2021). (B) In contrast, dynamic scaffolds consist of cell-laden matrices that are deformable, and their curvature can change dynamically due to external pressure or mechanical forces (Blonski *et al.*, 2021, Chan *et al.*, 2018). (C) Biohybrid assemblies can incorporate active contraction or pushing to create hybrid structures, such as origami folding triggered by fibroblast contraction (He *et al.*, 2018), or cells carving out an intestinal crypt-like geometry from a softer matrix (Gjorevski *et al.*, 2016).

tissues to form shape-programmable materials by using a collagen scaffold (Mailand *et al.*, 2022).

Scaffolds can also be designed to dynamically change their shape (see Fig. 4.2 B). For example, a cell monolayer on a flexible membrane can alter its curvature (Blonski *et al.*, 2021), and a combination of stretching and unstretching a cell-laden hydrogel can produce distinctive folds and patterns (Chan *et al.*, 2018). In some cutting-edge studies, researchers have utilized 4D bioprinting, where 3D printed objects undergo transformation over time (Arif *et al.*, 2022). For instance, a flat hydrogel sheet containing endothelial cells and photo-crosslinking can be transformed into a tube (Zhang *et al.*, 2020).

Additionally, the contractility of fibroblasts and hepatoma cells has been utilized to fold 2D structures into 3D shapes (He *et al.*, 2018) (see Fig. 4.2 C). Microplates with an origami folding pattern are created, and the cells apply forces to generate a 3D

structure. In other scenarios, cells are allowed to self-organize through the imposition of geometric constraints, which enhances the efficiency of organoid-like systems (Gjorevski *et al.*, 2016). In the case of intestinal organoids, controlling the stiffness of the matrix in specific regions leads to growth and differentiation at softer areas, producing a highly reproducible structure (Gjorevski *et al.*, 2022).

### 4.2.2 Manipulating biochemical signaling

Another approach to constructing biological structures involves controlling biochemical signaling to induce shape transformation. This approach utilizes natural processes in embryo morphogenesis, such as apical constriction in ventral furrow formation or cell jamming in the normal elongation of the zebrafish. Optogenetic tools, such as controlling Rho signaling, can be used to induce localized apical constriction with spatiotemporal control (Izquierdo *et al.*, 2018). This technique can also be applied to other proteins, such as Shroom3, to induce synthetic morphogenesis in neural organoids (Martínez-Ara *et al.*, 2022) (see Fig. 4.3 C).

Epithelial-mesenchymal interaction is another crucial aspect of the tissue folding process. Hughes *et al.* demonstrated that cell clusters can remodel the matrix to create oriented stresses that lead to budding in tissues (Hughes *et al.*, 2018). By controlling the location and density of these cell clusters, it is possible to manipulate the curvature of the epithelia. Mesenchymal condensation serves as a folding template for the final tissue structure (Palmquist *et al.*, 2022, Shyer *et al.*, 2017) (see Fig. 4.3 B).

The microenvironment plays a critical role in providing vital signals to tissues and can be manipulated to activate specific cellular functions. Microfluidic techniques can deliver appropriate morphogen gradients to the tissue with precise timing (Hofer and Lutolf, 2021). *In vivo*, multiple morphogens often act simultaneously. For instance, during neural tube development, there is an opposing gradient of sonic hedgehog (SHH) and bone morphogenic protein (BMP). With microfluidic devices, stable gradients can be generated, even in opposite directions (Demers *et al.*, 2016), thus mimicking symmetry-breaking events and directional neural tube patterning (see Fig. 4.3 D).

Moreover, genetic engineering of specific cells can be utilized to control signaling. Human pluripotent stem cells (hPSCs) can be programmed to express SHH (Cederquist *et al.*, 2019) (see Fig. 4.3 E). Mixing these cells with others could result in a polarized organoid and a patterned cerebral organoid.

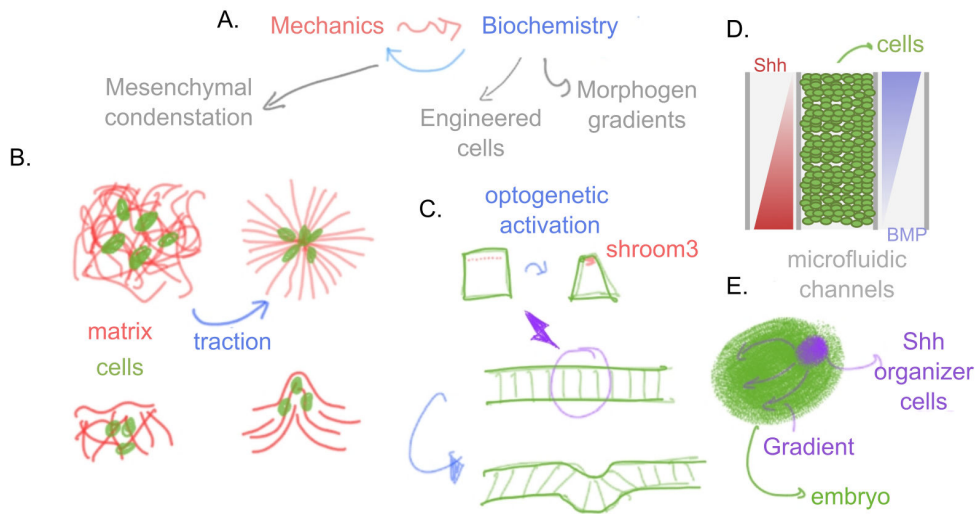


**Figure 4.3: Manipulating biochemical signaling:** Biochemical signaling and mechanics are interdependent in morphogenetic processes (A). The transport of signaling molecules can affect the cytoskeleton and mechanical properties of cells, while mechanical forces can also influence biochemical signaling. Microfluidics (D) is one method used to control biochemical signaling by providing opposing morphogen gradients through multiple channels (Demers *et al.*, 2016). Alternatively, cells can be genetically engineered to undergo apical constriction (C) or produce morphogen gradients (E) locally to form curved geometries (Cederquist *et al.*, 2019, Martínez-Ara *et al.*, 2022). Mesenchyme condensation (B) is another approach used to program curvature in developing tissues (Hughes *et al.*, 2018, Palmquist *et al.*, 2022).

#### 4.2.3 Exploiting mechanical instabilities

Morphogenesis, the process of shaping and formation of biological structures, often involves spontaneous pattern formation or symmetry-breaking events (Ishihara and Tanaka, 2018). These processes are often dictated by mechanical instabilities, which can lead to large deformations in soft matter systems. In material science, these instabilities are typically seen as problematic as they cause rapid breakage. However, in soft matter, large deformations can lead to interesting topological transformations, providing an opportunity for engineers to exploit these instabilities in the development of new actuators or soft robots (reviewed in (Pal *et al.*, 2021)).<sup>3</sup>

<sup>3</sup>"Mechanical instabilities have provided a unique approach to imbue "material intelligence" into soft machines without requiring the addition of rigid components. For example, binary actuators relying on mechanical instabilities can recreate logic modules and reproduce valving functionality using entirely soft elements."

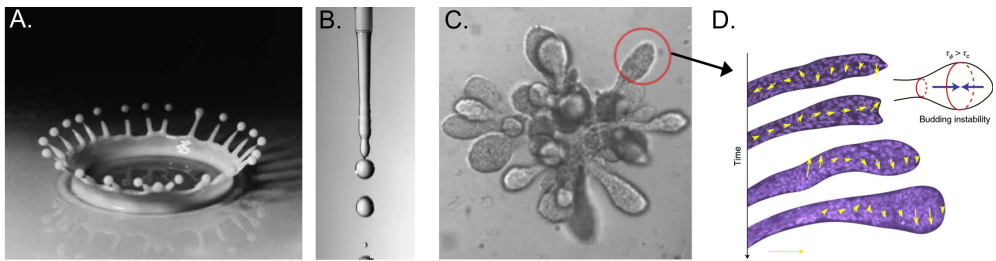


**Figure 4.4: D'Arcy Thompson compares biological budding to splashes** (A) of fluids and Rayleigh-Plateau instability (Thompson, 1979) (B), where liquid splits up into smaller droplets. This mechanism could also be seen in organogenesis of mammary tissue (C, D) (Fernández *et al.*, 2021).

The significance of mechanical instabilities was foreseen by D'Arcy Thompson in his comparison of fluid splashes to hydroids (see Fig. 4.4 A). He wrote that the shapes of a potter's cup, glass blower's bulb, and biological structures are simply glorified splashes formed slowly under conditions of restraint that enhance or reveal their mathematical symmetry (Thompson, 1979).<sup>4</sup> This conjecture has been confirmed through numerous quantitative studies on various systems, including ripples in leaves and wrinkles in the brain (Karzbrun *et al.*, 2018, Liang and Mahadevan, 2009).

There are various instabilities associated with solids and fluids. For example, the Rayleigh-Plateau instability explains why a fluid stream breaks into smaller packets, driven by the fluid's tendency to minimize its surface area due to surface tension. The same instability can arise when fluid is surrounded by an elastic medium, instead of air, provided the surface tensions can overcome the elastic stresses, leading to budding as observed in alveogenesis in human mammary tissue (Fernández *et al.*, 2021) (see Fig. 4.4 C-D). However, as tissues are active viscoelastic materials surrounded by viscoelastic medium, the timescales of these instabilities change, slowing down to hours instead of milliseconds in water droplets.

There are several types of mechanical instabilities associated with solids and fluids, including Rayleigh-Plateau instability, Kelvin-Helmholtz instability, Rayleigh-Taylor instability, viscous coiling and folding, and large-scale wrinkling and buckling

<sup>4</sup>I cannot recommend enough the chapter "the forms of cell". He states "Many forms are capable of realization under surface-tension, ... The subject is a very general one; it is, in its essence, more mathematical than physical; it is part of the mathematics of surfaces, and only comes into relation with surface-tension because this physical phenomenon illustrates and exemplifies, in a concrete way, the simple and symmetrical conditions with which the mathematical theory is capable of dealing."

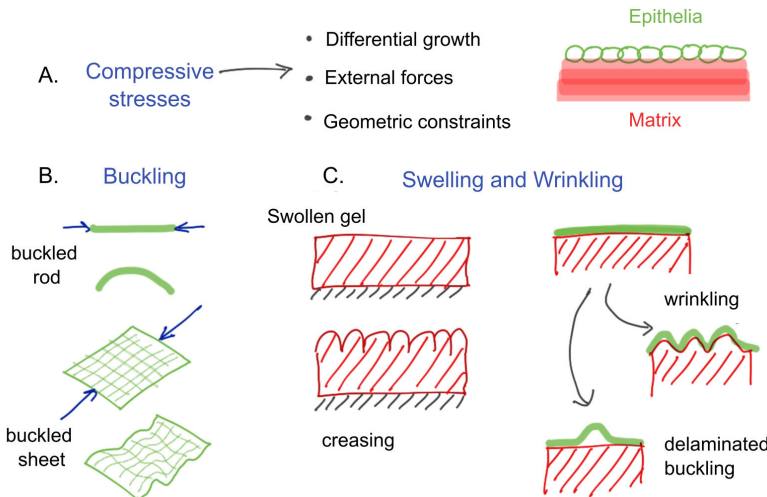


**Figure 4.5:** **Compressive stresses** occur frequently in many systems (A). We can consider epithelia and matrix as thin sheet supported by a compliant substrate. Thus, the tissue folding could be understood as buckling of sheets (B) or wrinkling or creasing of thin film supported by an hydrogel (C).

(Gallaire and Brun, 2017, Kourouklis and Nelson, 2018). In this study, we aim to harness these instabilities to recreate epithelial structures.

Applying compressive stresses is one of the easiest ways to induce mechanical instabilities in solids. These stresses can occur in biological systems as a result of differential growth, swelling, or morphogen gradients and can lead to various forms of instabilities, including wrinkling, creasing, and buckling. Buckling occurs when a thin sheet is subjected to in-plane compressive stress, and if the stress is above a critical value, the sheet undergoes out-of-plane deformation instead of in-plane shrinkage (see Fig. 4.5 B). In contrast, wrinkling and creasing occur in similar compressive stresses, but the thin sheet is typically supported by a compliant substrate.

The creation of biological tissues *in vitro* has been a subject of great interest in the field of tissue engineering. To reproduce the characteristics of these tissues, researchers have turned to the use of hydrogels. These materials can be mechanically and chemically manipulated to simulate the behavior of biological matrices, which provide support for epithelial structures.

One of the ways in which hydrogels can be used to recreate the behavior of biological tissues is through the application of physical stress. For example, swelling of the hydrogel can cause it to undergo rapid large volumetric changes, producing

crease-like patterns on the surface. If the hydrogel is constrained at the bottom, these creases can become permanent. Alternatively, if the hydrogel is supported by another flexible material, such as another hydrogel or an elastic substrate, the stresses produced during swelling will result in a wrinkling instability (see Fig. 4.5 A). These instabilities are important for understanding the formation of a variety of structures, including the gyrification of the brain cortex.

In a study by Tallinen *et al.*, the gyrification of the brain cortex was replicated through the programming of materials to produce wrinkling (Tallinen *et al.*, 2016). The researchers created a synthetic brain with an inner core of an inert elastomer and an outer layer of a swellable elastomer. On swelling, the outer layer produced folds that closely matched the process of gyrification (see Fig. 4.6 A).

Similar mechanisms have been observed in other systems undergoing differential growth, such as the branching of lungs and formation of intestinal villi (Shyer *et al.*, 2013, Varner *et al.*, 2015) (see Fig. 4.6 B,D). These findings highlight the potential of hydrogels as a tool for understanding the physical mechanisms underlying tissue development. However, it is worth noting that the mechanisms described here are the subject of ongoing research and debate in the field of developmental biology.

The ability to recreate biological tissue growth conditions *in vitro* has been made possible through the use of hydrogels. Researchers have discovered that by mechanically and chemically controlling the hydrogel, they can generate desired mechanical instabilities (Dervaux and Amar, 2012). This can be accomplished through the swelling or pre-stretching of the gel, or by manually applying compressive stresses.

One way to simulate growth is through the direct stretching or compression of the gel. Chan *et al.* (2018) showed that the patterns produced can be controlled by modulating the shear modulus of the hydrogel with the epithelial layer and stretch (see Fig. 4.5 B). By pre-stretching the hydrogel before seeding cells, they were able to produce folded patterns with different wavelengths depending on the type of pre-stretching applied (uniaxial or biaxial).

Another type of instability in bilayers is delaminated buckling, which is often observed in thin film delamination in furniture. This can be induced through compressive stresses created during growth or collective tension. Recent studies have shown that growing epithelia confined in a sphere undergo delaminated buckling after reaching a critical growth-induced stress (Trushko *et al.*, 2020) (see Fig. 4.6 C), or through intercellular stresses (Oyama *et al.*, 2021) or by placing a biofilm on top of the epithelial monolayer (Cont *et al.*, 2020).

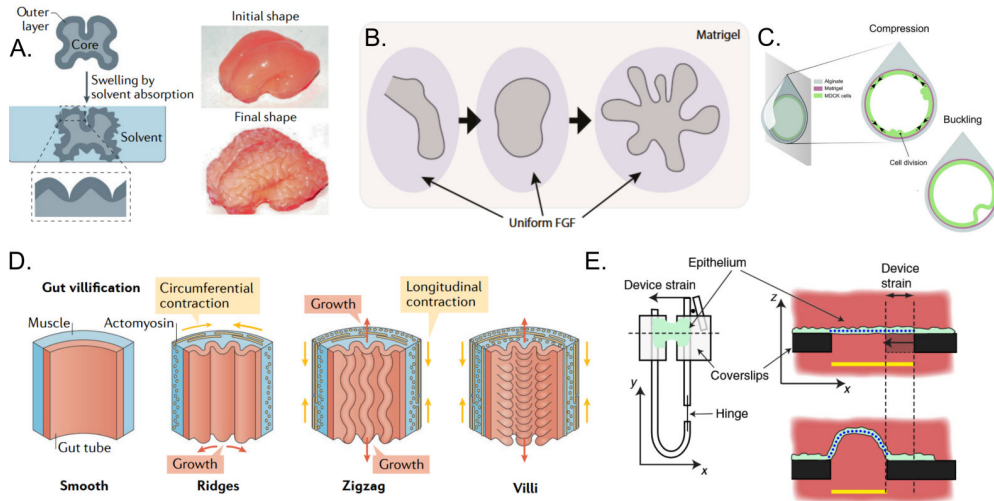


**Figure 4.6: Examples of mechanical instabilities:** (A) Synthetic mini brains illustrate the wrinkling of the outer layer with swelling mimicking gyration (Tallinen *et al.*, 2016). (B, D) Other way around where inner layer of lung or intestinal epithelia develops folds when embedded into a hydrogel or muscle shell (Shyer *et al.*, 2013, Varner *et al.*, 2015). (C) It is also shown that simple epithelial tissues embedded into a shell would also buckle (Trushko *et al.*, 2020). (D) (Wyatt *et al.*, 2020) used matrix independent tissue with compression to illustrate that the epithelial tissue itself can undergo buckling. *Panel A, D are adapted from (Collinet and Lecuit, 2021) and C from (Matejčić and Trepak, 2020)*

The formation of the ventral furrow in the drosophila embryo can also be considered as a buckling event. Although there are multiple explanations for this phenomenon, recent studies have shown that the instability leading to the fold is caused by embryo-level forces (Fierling *et al.*, 2022, Guo *et al.*, 2022). Apart from instabilities, it is remarkable that the mechanical information can be encoded in the substrate. For instance, the tension produced by the cells in a pre-stretched membrane, on cutting would lead to curling (Tomba *et al.*, 2022), or through stretching a suspended epithelial layer would also do the same (Fouchard *et al.*, 2020).

It is noteworthy that there is currently only one established method for directly applying compressive stresses to suspended epithelial tissue. The Lab of Guillaume Charras has developed a technique using a cell-laden collagen gel sandwiched between two rods, where the gel is digested with collagenase to create a suspended monolayer (see Fig. 4.6 E). Through extensive experimentation, they have observed that the compression of more than 35% strain produces transient buckling events (Wyatt

*et al.*, 2020). Importantly, the actin cytoskeleton plays a crucial role in buffering deformations in this system.

## 4.3 Tissue hydraulics

### 4.3.1 Hydraulic control of morphogenesis

In this thesis, we focus on the role of hydraulic pressure in morphogenesis. It has been well established in the field of developmental biology that fluid pressure plays a significant role in lumen expansion. For instance, in the mouse embryo, cell aggregates form small fluid cavities in intercellular junctions, which grow and coalesce into a large lumen, breaking the symmetry of the embryo, due to the presence of an osmotic pressure gradient ((Dumortier *et al.*, 2019); reviewed by (Torres-Sánchez *et al.*, 2021), see Fig. 4.7 A). This process is powered by the pumping of ions and water by the cells, which generates pressure in the fluid-filled cavities, ultimately leading to the formation of spherical embryos. For any inflated spherical shell, the relationship between pressure ( $\Delta P$ ), curvature ( $R$ ), and surface tension ( $\sigma$ ) can be described by Laplace's law.

$$\sigma = \frac{\Delta P R}{2}.$$

The shape that is created under pressure depends on the material properties of the tissue. For example, a homogeneous material would create a uniform curvature, such as a spherical shape, while an anisotropic tissue with oriented cells would result in various shapes, such as cylinders or ellipsoids (Stokkermans *et al.*, 2021) (see Fig. 4.7 C). An interesting example of this phenomenon can be seen in the lobed epithelium of lizard lungs, which resembles the shape of a stress ball. Palmer et al. propose that the smooth muscle network functions as a mesh that constrains the epithelium, much like the outer layer of a stress ball (Palmer *et al.*, 2021) (see Fig. 4.7 B). Upon the application of pressure, the epithelium inflates in the regions between the gaps in the muscles.

For embryos, an increase in pressure results in an increase in tension and stretching of the cells. Once a certain threshold is reached, the cell junctions may leak, causing a reduction in luminal pressure and shrinkage of the embryonic cavity. This system of pressure regulation through leakage acts as a mechanism for size regulation (Chan *et al.*, 2019). At the same time, it polarizes the embryo and promotes cell segregation and fate specification (see Fig. 4.7 A, reviewed by (Chan and Hiiragi, 2020)).

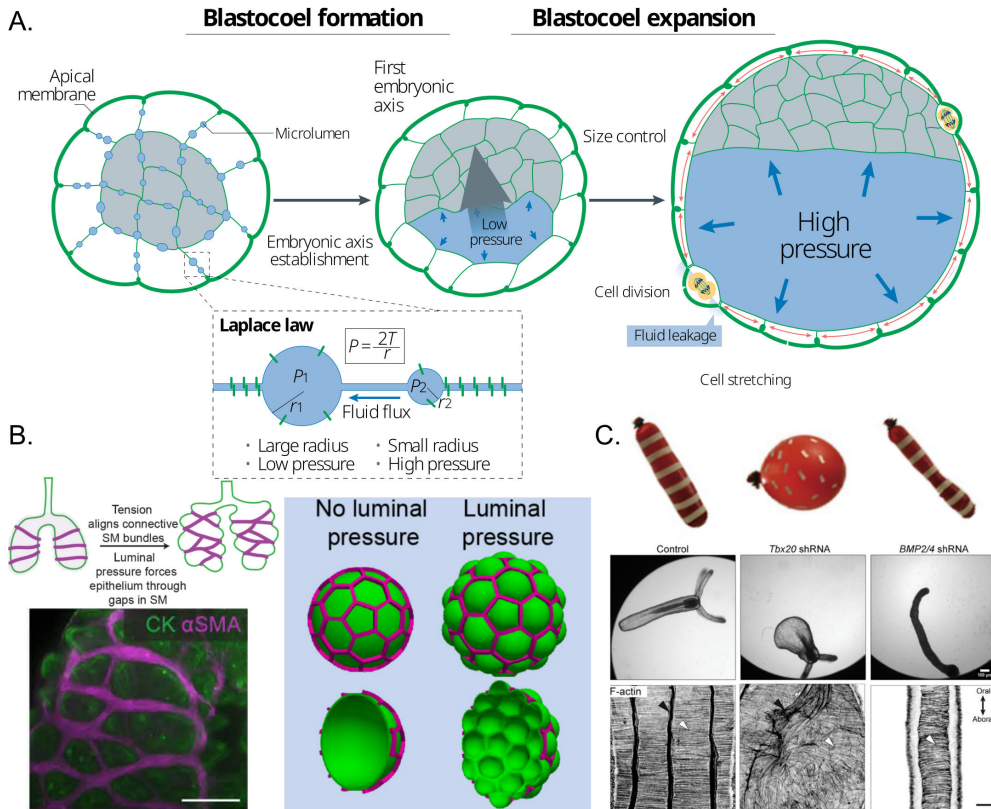


**Figure 4.7:** **Tissue hydraulics** plays an essential role in establishing (A) embryonic axis through lumen coarsening, and later the pressure regulates the size of the embryo. Laplace's law acts on the spherical cavities between cells to the whole blastocyst (Chan *et al.*, 2019, Collinet and Lecuit, 2021, Dumortier *et al.*, 2019). (B) Interestingly, if the inflated structure is surrounded by a mesh you see a stressball effect, where material inflates through the mesh. Similar phenomena is visible in growth and inflation of the lizard lungs. The smooth muscle constrains the deformation leading to stressball morphogenesis (Palmer *et al.*, 2021). (C) In cnidarians, the different orientation of F-actin leads to different shapes of the organism (Stokkermans *et al.*, 2022).

Similar coalescence and lumen coarsening have been observed in other systems (reviewed in (Schlifka and Maitre, 2019)). The pressure can also be generated through secretion of the matrix, as seen in the case of the drosophila hindgut with mucins (Syed *et al.*, 2012), or through the secretion of hyaluronic acid in the formation of ear canals in zebrafish otic vesicles (Munjal *et al.*, 2021). Despite numerous *in vivo* experiments, there are very few systems in which epithelial tissue can be subjected

to controlled shape and size *in vitro*.

### 4.3.2 Mechanics of domes

Many of the morphogenetic events are called doming because the shape vaguely resemble a spherical cap. For instance, doming of the retina in the eye or zebrafish embryo, or doming during duct formation of mammary or salivary glands. There are typically two mechanisms for these: first, an accumulation of the cells or matrix to create curvature; and second, trans-epithelial transport causing hydraulic pressure-driven shape change. The second kind is remarkable as they mimic various lumenized epithelia *in vivo*.

This is the most pertinent system to the thesis. I would briefly go into the historical developments in dome mechanics.

Fluid-filled dome formation in epithelial tissue culture has been recorded since 1933 (Cameron, 1953) (see Fig. 4.8 A). After several decades alongside the development of cell culture techniques, microscopy, and MDCK cell line<sup>5</sup>, in 1968, Leighton and colleagues observed that the confluent MDCK cell monolayers formed hemispherical blisters (domes) (Leighton *et al.*, 1969) (see Fig. 4.8 B). They observed that these are different from renal tubules because the apical surface, with microvilli, was facing outwards. They saw that these fluid-filled structures are dynamically changing size and curvature. They would burst to deflate and leak fluid out in the medium (Valentich *et al.*, 1979). After sometime, they could heal and form the dome again. Later, other cell lines derived from mammalian and amphibian kidneys were often observed to form domes too (Dulbecco and Okada, 1980, Leighton, 1981, Lever, 1979)

Now the mechanism is clear as the epithelial cells perform critical barrier function alongside controlling the transepithelial flow of ions and water. It was shown that hindering sodium-potassium ion pumping reduces the likelihood of domes (Leighton *et al.*, 1969). Thus, on forming a confluent monolayer these cells perform their function of pumping ions from apical to basal direction (Valentich *et al.*, 1979). If the substrate is solid and impermeable the tissue accumulates enough pressure to delaminate and form a spherical structure.

Most domes observed have been spherical and circular in footprint, indicating

---

<sup>5</sup>It is very important to acknowledge the contribution of Madin-Darby canine kidney (MDCK) cells to the field of mechanobiology and enhancing our understanding of tissues *in vitro*. Stewart H. Madin and Norman B. Darby, Jr. isolated female cocker spaniel dog's kidney tubules cells in 1958. MDCK cells can self-organize in 2D and 3D; form monolayers and stratified layers; and undergo collective migrations. These cells are incredibly robust for experimentation.

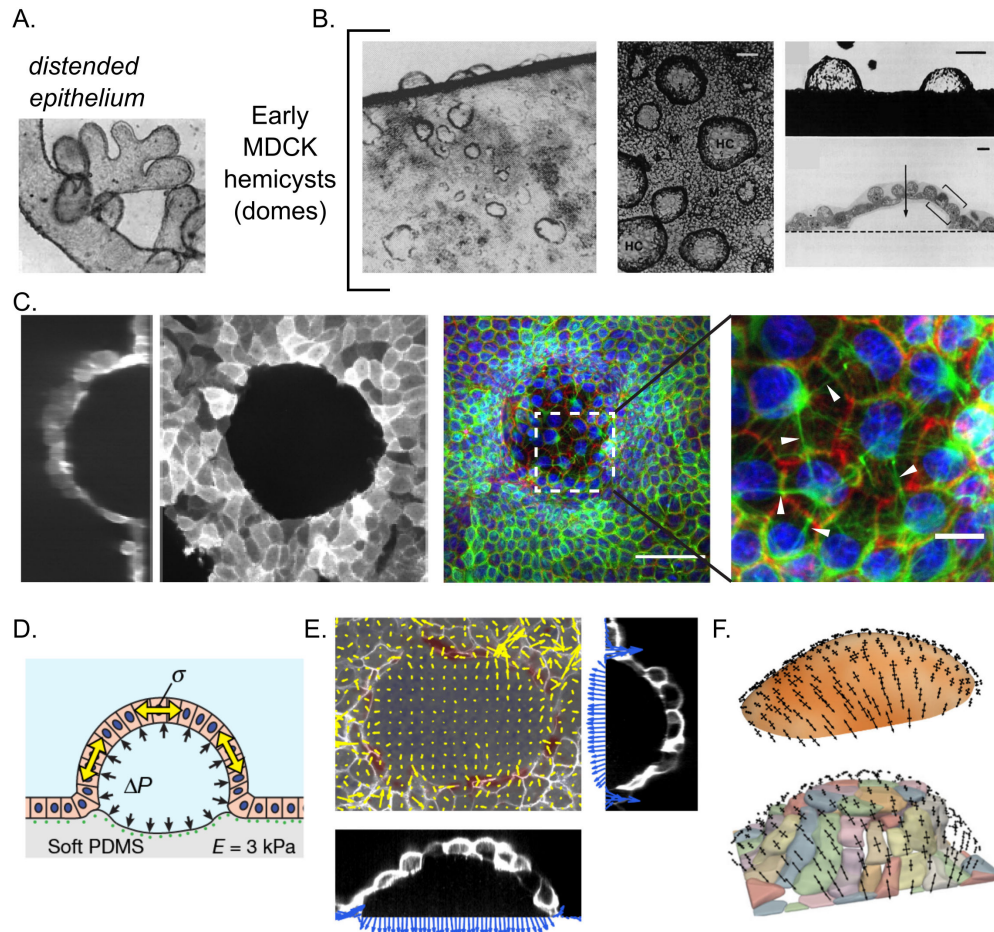


**Figure 4.8: Historical development of epithelial domes:**(A) Distended epithelium was observed in explant cultures in 1930-50s. (B) With MDCK cell line, spontaneously forming domes/hemicysts were characterized (Leighton *et al.*, 1969, Valentich *et al.*, 1979). (C,D) In our lab, shape and size of the domes were controlled with micropatterning adhesion protein (Latorre *et al.*, 2018). The pressure and tension was measured with Laplace's law and traction force microscopy. (E-F) For non-spherical domes, curved monolayer stress microscopy technique was implemented by segmenting the dome shape (Marín-Llauradó *et al.*, 2022).

uniform tension across the dome. This can be explained by considering the dome as a thin shell under pressure, similar to a bubble, and following Laplace's law. Early studies attempted to infer tension through geometry and pressure measurement (Tanner *et al.*, 1983), finding that the pressure was of the same order as physiological

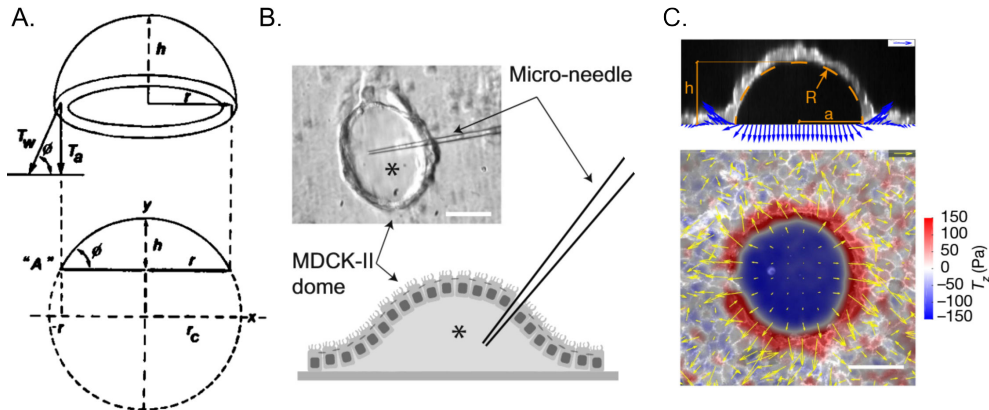


**Figure 4.9: Methods for measuring pressure and tension:** (A) Earlier studies tried to estimate tension through geometry and thickness of the monolayer (Tanner *et al.*, 1983). (B) Later, pressure was measured by puncturing the dome with a micro-needle. However, the measurement of pressure is static, because the dome deflated after the puncturing (Choudhury *et al.*, 2022b). (C) Traction force microscopy technique provides a viable non-invasive solution for measuring pressure under to domes (Latorre *et al.*, 2018).

vessels (see Fig. 4.9 A-B).

One study (Popowicz *et al.*, 1986) identified a “dome curve” when the frequency of domes was plotted against size, observing three classes of domes in terms of size. Smaller domes were observed to swell and increase in size. It was also suggested that there could be different subpopulations of MDCK cells. In the 1990s, many strains were characterized that formed different inflated structures, ranging from normal domes to tubules (Klebe *et al.*, 1995). One cell line, called super dome MDCK, formed larger domes.

Despite research into ion transport, hormone signaling, the role of tight junctions, and external shear stress, the understanding of the mechanics of domes and pressure has remained stagnant due to the lack of tools for measuring tension, pressure, and controlling the shape and size of these structures.

The work of Ernest Latorre in our laboratory has led to the development of a system for controlling the size of domes and studying the relationship between tension and pressure (Latorre *et al.*, 2018) (see Fig. 4.8 C-D). By utilizing protein patterning techniques, Latorre was able to create non-adhesive circular regions on soft PDMS gel, which, when seeded with MDCK cells, led to the formation of domes. The gel was embedded with beads to allow for the calculation of traction forces

and pressures exerted by the monolayer (see Fig. 4.9 C). This system allowed for a deeper understanding of the rheology of tissue and the role of the cytoskeleton. He observed that stretching the actin cortex leads to dilution, and that tension reaches a stable value regardless of strain. He also observed the surprising phenomenon of superelasticity, where cells are heterogeneously stretched in the dome when tension is uniform. To further understand the role of actin and keratin bundles in providing superelasticity, Latorre et al. developed a vertex model through which they could understand the instability triggered by actin dilution, and rescued by intermediate filaments.

Ariadna Marin-Llaurado extended Latorre's work by examining domes of varying sizes and shapes (see Fig. 4.8 E). This study found that different-sized spherical domes have similar tensions, and that pressure is compensated according to curvature. Marin-Llaurado couldn't rely on a simple formula for tension calculation, because the tension in non-spherical domes is non-uniform (Marín-Llauradó *et al.*, 2022). They used confocal microscopy to map dome curvature and calculated stresses computationally using a novel method called cMSM (curved Monolayer Stress Microscopy) (see Fig. 4.8 F). This method infers stresses just through geometry and pressure as in Young-Laplace relation. It does not need to make any assumptions related to material properties. The results showed that cells tended to align along the principal stress direction.

The mechanics of osmotic and hydraulic gradients are also crucial to understand. Choudhury *et al.* (2022b) demonstrated that kidney cells act like a mechanobiological pump. Using a two-layer microfluidic chip, the team was able to measure and apply pressure differences across an epithelial monolayer and observe that the tissue acted like a mechanical pump that stalls at high pressure. Remarkably, they discovered that diseased kidney cells pump in a different direction than healthy ones. They were able to control both osmotic and hydraulic pressure. Another study Ishida-Ishihara *et al.* (2020) investigated the connection between osmotic pressure and extracellular matrix swelling. The researchers found that osmotic gradients trigger Aquaporin transport channels, leading to dome formation through Matrigel swelling. However, these domes are gel-filled structures that differ from fluid-filled domes.

MDCK domes provide a model system for studying transport, cell fate, and tissue dynamics with a curvature. However, control over luminal pressure in these structures remains a challenge.

## 4.4 What is to be done?

Morphogenesis refers to the process of tissue deformation or growth, which results from the combination of both endogenous and exogenous mechanical forces (Collinet and Lecuit, 2021, Valet *et al.*, 2022). These forces may arise from the contractility of the epithelium and the surrounding matrix, as well as hydraulic pressure from the lumen (Chan and Hiiiragi, 2020, Torres-Sánchez *et al.*, 2021). The various stresses act on different components of the tissue, such as cells and the extracellular matrix, which exhibit unique viscoelastic properties and remodeling time scales (Ambrosi *et al.*, 2019, Cavanaugh *et al.*, 2020, Kelkar *et al.*, 2020). However, comprehending how these stresses interact with viscoelastic properties to bring about particular morphogenetic events *in vivo* presents significant technical and conceptual challenges. These obstacles include disentangling the roles played by distinct components in a system, a lack of tools for quantitative measurements of stresses and mechanical properties, and an inability to apply controlled stresses over a wide range of amplitudes and rates.

In response to these challenges, bottom-up approaches have emerged as a complementary strategy for understanding the morphogenetic potential of individual components and building complex, functional tissues (Ingber, 2018, Trentesaux *et al.*, 2023). These approaches have been successful in engineering basic morphogenetic processes such as epithelial bending or buckling (Matejčić and Trepat, 2022). However, even though bottom-up approaches are proving to be successful, we still need tools that can measure and control the shape and stress of 3D epithelia simultaneously. Additionally, we lack computational models that integrate cellular and tissue shape with the subcellular determinants of epithelial mechanics, such as the contractility, turnover, and viscoelasticity of the actomyosin cortex.

This thesis seeks to address these gaps in knowledge by investigating the mechanics of epithelial tissues. A comprehensive understanding of the principles that govern tissue form and function is essential for both advancing our understanding of fundamental physical rules in biology and inspiring new engineering tools and design principles. To achieve this, we leverage cutting-edge technologies, such as 3D printing, microfluidics, and 3D cell cultures, to individually control morphogenetic driving factors.

Our approach provides a material science perspective for probing the intricate mechanisms involved in the generation of forces and shape changes at the cellular and

tissue levels, and holds promise for discovering emergent phenomena and enabling the building of novel tissue forms and assemblies.

# **Chapter 5**

## **Structure of the thesis**

### **5.1 Objectives**

#### **General aim of the thesis**

This thesis aims to investigate the mechanics of epithelial tissues under controlled pressure.

#### **Specific aims of the thesis**

General aims are divided into specific goals:

1. Develop a novel technology for constructing three-dimensional epithelia using lumen pressure control.
2. Characterize the material response of the pressurized epithelial tissue.
3. Explore the mechanics of epithelial folds.

### **5.2 Thesis outline**

Results are presented in Part 2 with four chapters that address the specific aims of the thesis and provide an understanding of the mechanics of epithelial layers subjected to controlled pressure.

- Chapter 6 details the construction of an experimental system designed to physically control epithelial monolayers. This chapter showcases the main

result of the PhD, a novel microfluidic system that generates 3D epithelia with controlled pressure and shape. The chapter highlights the successful development of the microfluidic system, while also summarizing any failed or attempted methods used in constructing the device.

- Chapter 7 focuses on using the microfluidic device to understand epithelial mechanics. The chapter reports the results of rheological experiments and relates them to a computational framework that explains the observed phenomenology in terms of the viscoelasticity of the actomyosin cortex.
- Chapter 8 describes a buckling instability in pressurized epithelia. It is found that rapid deflation produces a buckling instability that leads to the formation of epithelial folds. Buckling occurs across different length scales to overcome compressive stresses, and folding patterns become more complex with increasing size. The chapter discusses the potential of guiding the folds by controlling the shape and size of the epithelia.
- Finally, in Chapter 9, the findings are summarized with a list of conclusions along with a brief discussion on future perspectives of this thesis.

In summary, the thesis presents a microfluidic-based technique to impose a controlled deformation on an epithelial monolayer while continuously monitoring its state of stress. This technique allows for investigation of the active viscoelasticity of epithelial layers over physiological time scales. The thesis also presents a 3D model of the epithelium, developed by Adam Ouzeri and Marino Arroyo, which explains the observed phenomena using the active viscoelastic properties of the actomyosin cortex. Furthermore, it is demonstrated that these viscoelastic properties, along with adhesion micropatterning, can be utilized to engineer epithelial wrinkles with predictable geometry. The results provide an understanding of the mechanics of epithelial layers subjected to controlled pressure and showcase the potential of the developed techniques to further explore the synthetic morphogenesis.

## **Part II**

# **Results**



# **Chapter 6**

## **A microfluidic device for generating 3D epithelia**

### **6.1 Introduction**

To generate three-dimensional epithelial structures in vitro from planar epithelial monolayers, we chose to utilize an existing system of epithelial domes (spontaneous domes) developed by Ernest Latorre and improved by Ariadna Marín-Llauradó (Latorre *et al.*, 2018, Marín-Llauradó *et al.*, 2022). This system involves seeding a Madin-Darby canine kidney (MDCK) cell monolayer on a substrate that is patterned with circular non-adhesive regions. The cells invade these regions and form a cohesive monolayer everywhere within 24 to 48 hours. Due to the active ion pumping mechanism of the MDCK cells in the apical-to-basal direction, the cells delaminate from impermeable substrates such as glass or soft PDMS gel and form spherical cap structures on the circular patterns, known as epithelial domes. Latorre and Marín-Llauradó demonstrated that they could form a variety of structures with controlled shape and size, ranging from spherical to tubular caps.

This system also enables the use of 3D traction force microscopy to measure pressure. The technique involves measuring the deformation of a soft PDMS gel embedded with beads to characterize the forces and pressures applied by the cells on the substrate. This method offers an innovative approach to measuring pressure compared to the previous technique of puncturing epithelial domes with a microneedle (Choudhury *et al.*, 2022b, Tanner *et al.*, 1983). It also allows for the characterization

of the rheology of epithelia and the discovery of interesting material properties such as the superelasticity of cells during stretching (Latorre *et al.*, 2018).

However, the formation of epithelial domes is dependent on the ion pumping mechanism of the domes, making them spontaneous structures. Therefore, the timescales for the dome stretching are not controlled, although this process can be marginally accelerated by a few hours through the use of drugs like Forskolin, which can activate transepithelial channels of  $\text{Na}^+/\text{K}^+/\text{Cl}^-$  (Bourke *et al.*, 1987, Klebe *et al.*, 1995). Furthermore, not all epithelial tissues actively pump ions or do it with the required polarity for dome formation. In this chapter, we will be discussing a microfluidic chip that can inflate an epithelial monolayer into a dome with arbitrary time evolution of applied pressure while also allowing us to measure and control the forces involved.

## 6.2 Monolayer Inflator

Drawing inspiration from the pioneering work on organ-on-chip microfluidic devices, we have deemed these platforms to be an ideal system for the precise manipulation of pressure, cell culture conditions, and the acquisition of high-resolution imaging data (Huh *et al.*, 2010, Nelson *et al.*, 2017). An illustrative example is the lungs-on-chip device, which comprises two distinct layers separated by a porous membrane. The top layer contains a channel for the epithelial cells, while the bottom layer has a

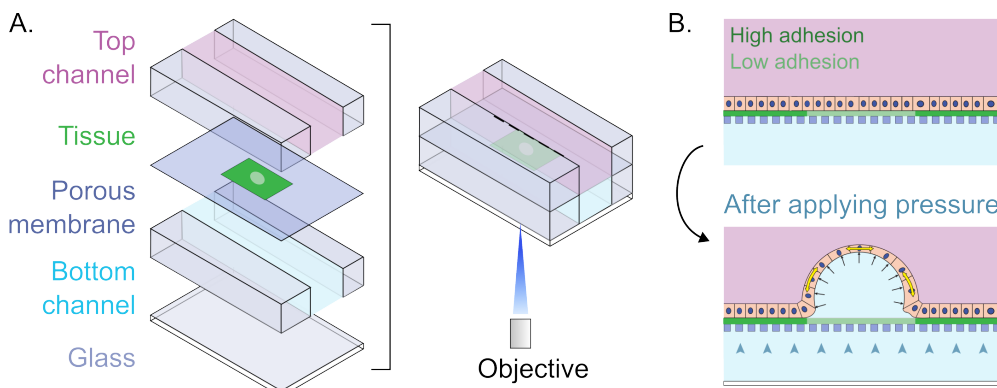


**Figure 6.1: Conceptual design of MOLI:** (A) Microfluidic device consist of a porous membrane sandwiched between two layers of schannels. (B) Upon application of pressure, cells from low adhesion will detach to form an epithelial dome.

channel for the endothelial cells. This device is assembled on a thin glass slide, which facilitates the collection of high-quality imaging data.

Therefore, we conceived the idea of a MONoLayer Inflator (MOLI) device, which utilizes a two-layer microfluidic channel with one side for epithelial monolayers and the other for the application of pressure (see Fig. 6.1). The epithelial monolayer side is micropatterned with a protein that contains non-adhesive or less-adhesive regions for dome formation. Our working hypothesis postulated that cells would adhere to the protein substrate uniformly, even in regions with lower adhesive properties. We anticipated that upon the application of pressure, cells would detach from the regions with weaker adhesion, leading to the formation of a dome-shaped structure.

We attempted to fabricate the devices by utilizing plastic stickers and photopolymerizable adhesive, but encountered difficulties such as fluid leakage and limited biocompatibility, rendering them unsuitable (Bartolo *et al.*, 2008, Sollier *et al.*, 2011). Consequently, we opted for the utilization of PDMS material to construct the microfluidic chip due to its facile handling and processing characteristics.

### 6.3 Fabrication of the device

The structure of the device consists of four layers: glass, bottom channel, porous membrane, and top channel. These layers are bonded together using ozone plasma activation.

For imaging epithelial structures with high-resolution confocal microscopy, the device must be mounted on a thin glass slide. We used #0 glass slides, which have

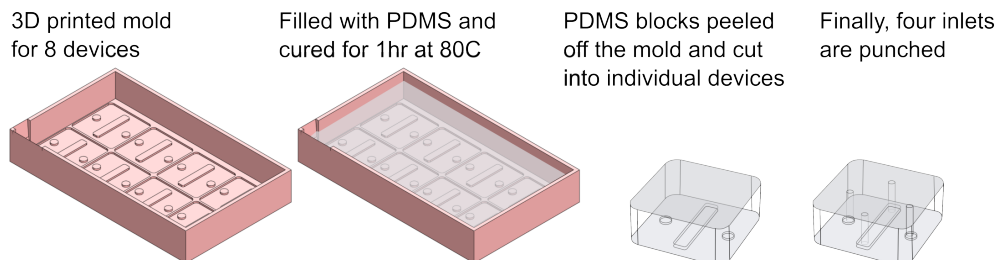


**Figure 6.2: 3D printed mold for the device** patterned to prepare eight devices at a time. The thickness of the PDMS block is controlled with volume of PDMS poured into the mold. After polymerization, the PDMS is cut into individual pieces and inlets are punched with a biopsy punch.

a thickness range of 85-115  $\mu\text{m}$  and are designed for high-performance microscopy applications.

To ensure that the porous membrane is positioned as close as possible to the microscope objectives, whose working distance typically ranges between 200  $\mu\text{m}$  and 1000  $\mu\text{m}$ , it is crucial that the channel is sufficiently thin. To this end, we fabricated the bottom layer with a thickness of 100  $\mu\text{m}$ . This thickness provides adequate structural support for manual handling, while avoiding potential microfluidic issues arising from pressure loss and lower flow rates. To achieve the desired thickness, we utilized a spin coating method to fabricate a thin layer of polydimethylsiloxane (PDMS). Subsequently, the layer was precisely cut into the channel shape using a desktop cutting machine (Silhouette Cameo 4, Silhouette America).

The primary function of the porous membrane is to enable pressure application while preventing the migration of cells from the cell channel to the pressure channel. Initially, we used a membrane with pores of 10  $\mu\text{m}$  diameter based on literature. We attempted to create 10  $\mu\text{m}$  pores in a 100  $\mu\text{m}$  thin layer of PDMS using photolithography to facilitate manual handling. However, we encountered difficulty in fabricating 10  $\mu\text{m}$  pillars with a height of 100  $\mu\text{m}$  due to an excessively high aspect ratio, making the pillars too fragile and prone to breakage during fabrication. Therefore, we opted to employ plastic, polyethylene terephthalate (PET), membranes with 10  $\mu\text{m}$  pores.

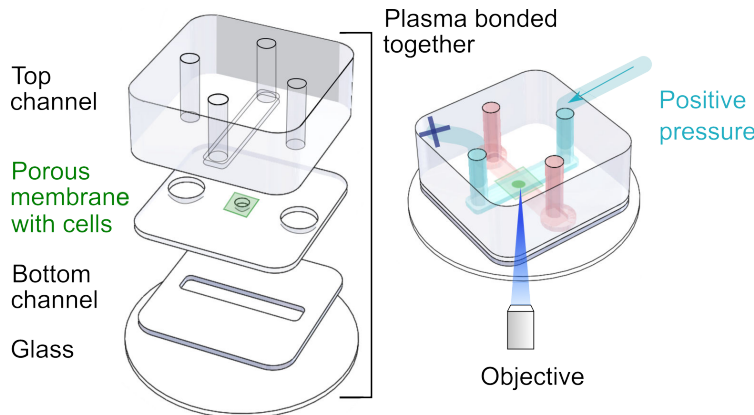


**Figure 6.3: Fabrication of MOLI:** Four layers assembled together with ozone plasma cleaning. Each channels has a inlet and outlet. Only the pressure channel is connected to the tubing; one side connects to the reservoir and other is sealed.

The thin (10  $\mu\text{m}$ ) plastic sheets were easily manageable, but we encountered difficulties with bonding and experienced leakages due to membrane wrinkling. To address these difficulties, we decided to modify the middle layer by using a PDMS layer with a hole attached to a small piece of membrane, instead of whole layer being a porous membrane. This approach allowed us to achieve stronger and leak-proof bonding by sandwiching a smaller area between the two PDMS layers. The middle PDMS thin layer was constructed with a 1.2 mm hole to expose the membrane to pressure, as this dimension is approximately the size of the field of view of a 10X objective.

The design of the top channel in the device involved a PDMS block with a 5 mm thickness and a 1mm engraved channel. The decision to select the thickness of the top channel was based on the requirement for the block to be sufficiently thick to accommodate tubing for pressure application. To create the mold with the channel, a precision 3D printer (Solus DLP 3D Printer) was utilized. Additionally, four inlets with a diameter of 1.5 mm were punched into the block using a biopsy punch to facilitate two inlets for the pressure channel and two inlets for cell seeding purposes (see Fig. 6.2).

Ultimately, the integration of the layers was accomplished through a two-step bonding process utilizing an ozone plasma cleaner (refer to Fig. 6.3). First, we bonded the glass to the bottom channel and simultaneously bonded the middle layer to the top channel. Following this step, the two assembled layers were bonded together with the membrane sandwiched in the middle to create the final device.

## 6.4 Protein patterning and "upside-down" cell culture

To overcome issues encountered in earlier prototypes, we opted to employ a glass-bottomed dish (35 mm, #0 coverslip thickness, Cellvis) as the container for our experimental setup. This design choice was made to address concerns surrounding the potential for cell culture medium to spill over/under the device during pressure application, especially in the case of a leaky device.

In the context of the spontaneous dome system, the upper surface is accessible for various treatments and microcontact printing using a PDMS block. However, in our case, we have a completely sealed device, which necessitated the use of the photopatterning technique known as PRIMO. In brief, first the surface to be micropatterned is coated with poly-L-lysine (PLL) and then SVA-PEG chains. Upon

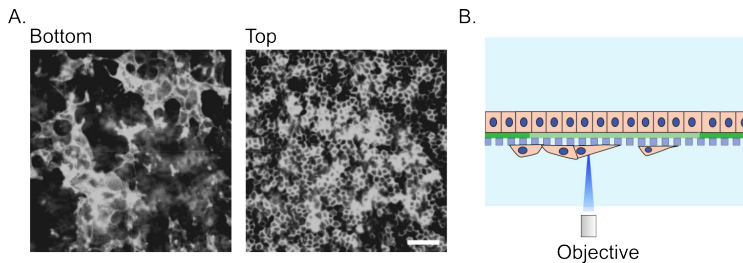


**Figure 6.4: Cells filtering through the membrane:** (A) Images of MDCK-CiBN CAAX GFP monolayer on the both sides of the membrane. Scale bar is  $80\mu m$ . (B) Schematic of imaging through the porous layer.

illumination with UV light (375 nm), PEG chains in selective regions could be cleaved and subsequently exposed to adhesion-promoting proteins. The PRIMO technique had been optimized previously for substrates made of glass and soft PDMS. We had to optimize the technique for use with a porous plastic membrane, which entailed increasing laser power to  $1500\text{ mJ/mm}^2$  (for details see the Appendix A). We also optimized coating the devices with fibronectin, vitronectin and collagen. For the experiments featured in this thesis, we are using fibronectin mixed with fluorescent fibrinogen for finding the samples.

To ensure successful attachment of cells and formation of monolayer, a concentration of  $25\text{-}30 \times 10^6\text{ cells/mL}$  was seeded for one hour, followed by rigorous flushing with fresh cell culture media to wash away any unattached cells. Early experiments revealed that while cells attached to the top side of the porous membrane, there were very few dome formations upon application of pressure. Additionally, imaging through the porous membrane was poor quality, as the cells were further away from the microscope objective, and some cells were filtering through the membrane from top to bottom (see Fig. 6.4).

To prevent cells from crossing the membrane, various plastic membranes with smaller pore sizes (ranging from 50 nm to 10  $\mu m$ ) were systematically tested. Considering the flow rates and cell filtration through the membrane, a 400 nm pore size membrane was chosen. However, imaging the green channel (488 nm) through these pores was impossible. Therefore, an "upside-down" cell culture approach was implemented, where the device was flipped immediately after seeding cells in the bottom channel to ensure attachment on the membrane instead of the glass (see Fig. 6.5). Thorough washing of the channel was necessary to prevent cell attachment to the glass, which would have obstructed the imaging of the domes.

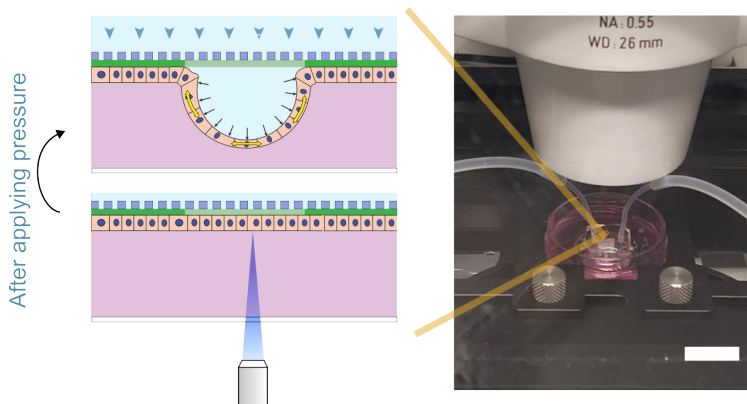


**Figure 6.5: Upside-down cell culture:** Illustration of upside-down cell culture and the experimental setup on the microscope stage.

Despite optimization efforts, achieving complete coverage of non-adhesive regions with a cell monolayer remained a significant challenge. To address this issue, the protein concentration in these regions was increased to facilitate cell attachment at the designated dome location. Upon application of pressure, cells from the lower adhesion region would detach, resulting in the formation of the dome structure.

## 6.5 Pressure control

For the application of external pressure, we selected hydrostatic pressure as the method of choice. Previous studies had reported a pressure requirement of approximately 100 Pa, equivalent to 1 cm of water column, for the formation of a dome. Initially, pipette tips were employed to apply pressure, but we observed that they were susceptible to bubble formation and leaks. Hence, we switched to using Polytetrafluoroethylene tubing, which was connected to a 50 mL reservoir (Falcon tube) to mitigate these issues (see Fig. 6.6). By adjusting the height of the tube to match the air-liquid interface in the reservoir with the device, zero pressure was exerted on the cell monolayer. To apply pressure, we increased the height of the tube by 2cm, resulting in the application of 200 Pa pressure to the monolayer, leading to the delamination of cells and the formation of domes.

Nonetheless, we exercised caution regarding the potential occurrence of bubble formation within the cell channel. To avoid this we subjected the media to a vacuum chamber for 30 min prior to the experiment to eliminate any nascent bubbles that

may have developed over time. During tubing insertion, however, the system posed a risk of reintroducing bubbles into the system. To counter this issue, we employed the two inlets for each channel to flush fresh media from the reservoir, ensuring that no bubbles were present.

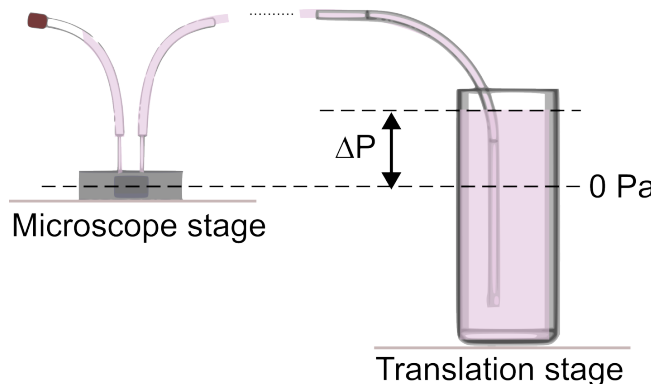


**Figure 6.6: Hydrostatic pressure application:** The device is positioned on a microscope stage and connected to a reservoir of media, which in turn is attached to a translation stage. By increasing the difference between the device and the air-liquid interface, we can measure and apply hydrostatic pressure.

To control the pressure, we used an automatic translation stage (Zaber High speed motorized linear stage) that could be programmed to lift the reservoir. We measured the pressure by tracking the height of the stage and the zero-pressure position. With this stage, we could apply pressure in the range of  $0 \rightarrow 1500$  Pa, and we could even apply negative pressure by setting it lower. For our experiments, we used the range of  $-200 \rightarrow 1300$  Pa.

This translation stage is capable of accommodating linear velocities ranging from 0.000303 to 280 mm/s, which correspond to pressure rates of 0.00303 to 2800 Pa/s. At higher pressure rates, one may inquire about pressure losses within the device. To calculate these losses, we assumed that the walls of the microfluidic device remain undeformed given the small pressure differentials (200 Pa), and that all flow rate is due to changes in volume in the domes. Consider, an 80  $\mu\text{m}$  diameter dome with 100% strain holds around 0.1  $\mu\text{L}$  of fluid, which flows through a  $5020 \mu\text{m}^2$  dome footprint. The membrane vendor specifies a limiting flow rate of 45 mL/min/cm<sup>2</sup> for water at 70 kPa. Assuming a linear relationship between flow rate and pressure, we can find that the flow rate through the dome footprint for a pressure of 200 Pa to be  $1.0952 \times 10^{-13} \text{ m}^3/\text{s}$ . By considering the length of the tube (30 cm), its internal

diameter (1 mm), and the dynamic viscosity of water (1 mPas), we can use the Poiseuille equation to estimate the pressure loss in the tubes to be 0.4523 Pa. This value is negligible in comparison to the pressures that are applied in the system.

## 6.6 Imaging the epithelial domes

Following extensive optimization of protein patterning, cell culture conditions, and confocal microscopy techniques, we were able to generate domes in accordance with the intended pattern and exert precise control over the pressure required for their formation. To obtain images of the dome, we utilized a spinning disk confocal microscope with a 40X objective lens (NA 0.75), which allowed us to visualize the membrane (CIBN CAAX GFP) and adhesion protein (Fibrinogen) pattern in separate channels (488 nm and 644 nm, respectively). By incorporating a labeled adhesion protein, we were able to track the formation of the domes with greater ease and accuracy.

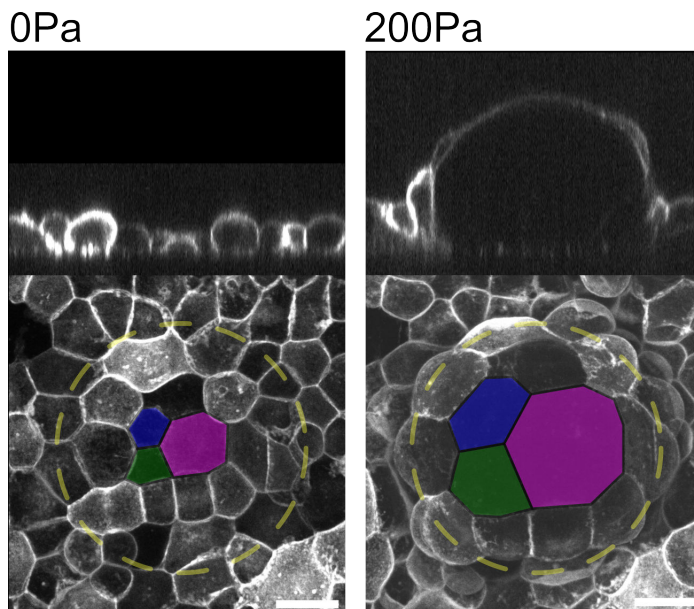


**Figure 6.7: Epithelial dome:** Representative confocal microscopy sections of domes at 0 Pa and 200 Pa. Images in the XY plane represent the dome's maximum projection, while images in the XZ plane represent a cross section at the center plane. Three cells are highlighted with color to show the stretching during the dome inflation. Scale bar is 20 $\mu$ m.

We initially focused on characterizing the mechanics of spherical domes at constant pressure to gain insights into epithelial behavior (see Fig. 6.7). Laplace's law was employed to calculate tension using pressure, cell shape, and tissue curvature data, which we could easily monitor. Unlike previous studies that did not control the pressure under the dome, our experimental system allowed us to inflate and deflate the domes in seconds. This forced us to monitor them by observing the base of the dome where the monolayer would intermittently come in and out of view.

Acquiring images of the dome stack in a confocal microscope required three minutes using a step size of 0.5  $\mu\text{m}$  (exposure 500 ms) and a height of 100  $\mu\text{m}$ , which was slower than the rate at which we could deform the dome by changing the pressure (see Fig. 6.7). To investigate the rheology of the domes, it was necessary to monitor their dynamic response at faster pressure rates and shorter timescales while measuring dome strain and curvature. Since the dome possessed inherent symmetry, imaging the mid-section of the structure provided all the geometric information required.

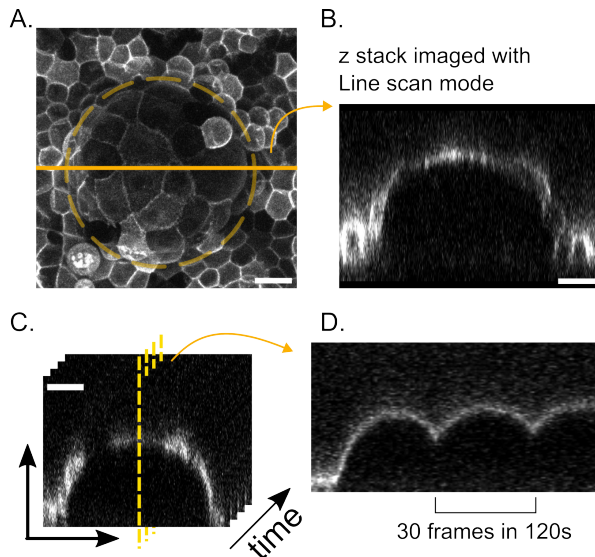


**Figure 6.8:**  
**Imaging the dome with Line scanning mode:**  
(A) Confocal microscopy image of a dome's maximum projection.  
(B) Midsection of the same dome imaged with the line scan mode (LSM).  
(C-D) Timelapse of the dome in LSM and a kymograph showing dynamics of the domes when imaged at time-step of 4s.  
Scale bars are 20  $\mu\text{m}$ .

Using the line scanning mode of a Zeiss Airy Scan Microscope, we imaged a single line of pixels across the midsection of the dome and acquired a confocal z-stack (1024 pixel, 4.1  $\mu\text{s}/\text{pixel}$  dwell time, and 1  $\mu\text{m}$  step size) along the height of the dome (refer to Fig. 6.8). This approach allowed us to obtain a cross-sectional view of the dome in a fraction of the time required for a normal stack. By enabling piezo stage movement, we imaged a 100  $\mu\text{m}$  tall dome in just 4 seconds and tracked its height

evolution using a kymograph of the central part of the dome. It is important to note that this imaging method is primarily useful for tracking dome strain and curvature, and the cell images obtained are often of low quality.

## 6.7 Light-sheet MOLI

We utilized a Brucker QuVi SPIM light sheet microscope to capture rapid subcellular or cellular changes. The microscope was equipped with two immersion-upright 40X objectives (NA 0.8) at 45° to the horizontal plane. Drawing upon our proficiency in device fabrication, we devised a new setup that facilitated top imaging of cells and porous membranes (see Fig. 6.9).

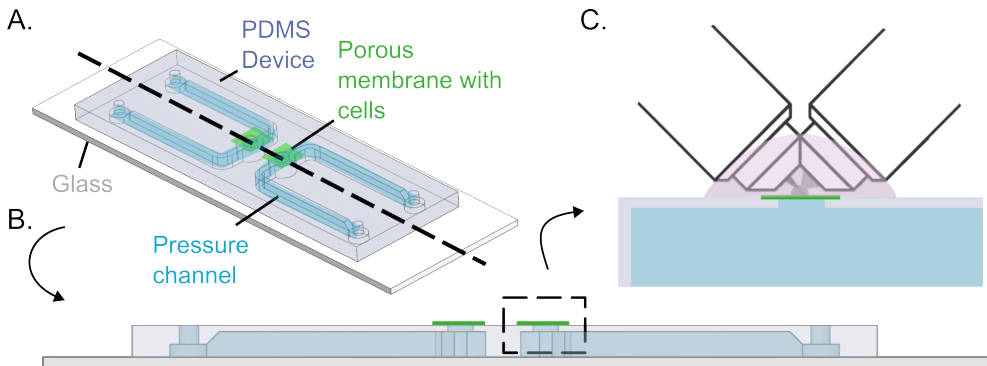


**Figure 6.9: Light sheet MOLI:** (A) Isometric illustration of a single piece PDMS block engraved with two channels, so that we can have two devices in one. (B) Cross-section of the device. (C) The device is used with 40x immersion objectives coming at 45 deg angle. This limits to the field of view to  $332 \times 332 \mu\text{m}^2$ .

To simplify the fabrication process, we inverted the conventional MOLI device. This necessitated only a pressure channel and a middle layer with a hole and porous membrane. The device was manufactured sufficiently thick to plug in the tubing, and given the device and channels' size, we produced the mold using a standard 3D printer, Ultimaker 3D printer. We incorporated a ridge-like protrusion to manufacture the pressure channel and cell seeding hole in one go. The device was bonded to a microscope slide using unpolymerized PDMS, and we performed PRIMO patterning of the device by flipping it upside down. In this setup, seeding cells was easier, as the cell seeding part was exposed.



**Figure 6.10: Dome imaged with Light sheet MOLI:** Mid-section of a dome with membrane marker imaged every 2s. Showing the shape of individual cells undergoing changes during deflation. Scale bar is  $20\mu m$ .

As expected, we were able to generate domes using the same system as before by applying pressure. The imaging technique we developed enabled us to acquire a full dome image in a mere 4 seconds, which involves using objective scan, where only one objective to scan the dome with 100 frames with step size of  $1\mu m$  at rate of 4ms. This allows us to observe fast-moving features that were indiscernible with other imaging techniques (see Fig. 6.10).

## 6.8 Summary and Discussion

We have developed a microfluidic chip to generate 3D curved epithelia, utilizing a multilevel device consisting of two layers separated by a porous membrane. Seeding cells on the membrane in the bottom channel allowed for dome formation closer to the microscope objective, enabling high-quality confocal imaging. Hydrostatic pressure was under the dome was controlled dynamically, allowing for monitoring of cells and tissue behavior. Additionally, we developed imaging strategies to capture dynamics of these 3D structures faster using line scanning mode of confocal microscope or light sheet microscope.

Using this device, we were able to form the domes and monitor cellular and tissue behavior. As demonstrated in previous studies, the most intriguing aspect of the system is that complex materials such as epithelial tissue, in order to maintain mechanical equilibrium, must adopt a spherical cap shape for a circular footprint. This uniform curvature and pressure imply uniform and isotropic tension, independent of tissue material properties (Latorre *et al.*, 2018, Marín-Llauradó *et al.*, 2022). The tissue tension can be easily measured by applying Laplace's law for spherical cap domes. However, in the case of non-spherical geometry, there would be anisotropic stresses that would require a computational model, such as curved monolayer stress microscopy, to solve an inverse problem to go from geometry to forces (Marín-

Llauradó *et al.*, 2022).

The geometry of the domes is primarily controlled by the adhesion protein pattern, but delamination can still occur. In spontaneous domes, circular footprints were found to be the most common (Tanner *et al.*, 1983), while domes formed around sharp corners can blunt themselves through delamination (Latorre *et al.*, 2018). This must be taken into consideration when creating specific geometries. Tissue tension and adhesion forces also interact with each other. In MDCK suspended monolayer, it is seen that cell-cell junctions are stronger than cell-substrate adhesion (Harris *et al.*, 2012), so if tension at the base of the dome exceeds the adhesion forces, it can lead to detachment and delamination.

Furthermore, although not studied systematically here, MOLI can be used as a quantitative peeling system to probe tissue detachment from the substrate. If the dome retains its spherical shape, we can calculate the forces required to break cell-substrate adhesion and identify the contribution of focal adhesion molecular components.

This system provides a novel approach for testing material properties and probing mechanics at the tissue scale, allowing for simultaneous high-quality imaging and monitoring of cytoskeletal components and the nucleus. Additionally, we can create a 3D tissue with controlled lumen pressure, providing a well-controlled protocol that is suitable for replicating curvature-pressure-tension conditions in various cell types, including those that do not actively pump ions and form spontaneous domes. However, our primary focus is on comprehending the mechanics of epithelial tissue under controlled pressure.



# **Chapter 7**

## **Dynamic material response of epithelial domes**

### **7.1 Introduction**

This chapter focuses on investigating the dynamic material response of epithelial domes to varying strain, tension, and pressure. In a morphogenetic context, pressure levels can vary significantly across a wide range of magnitudes and timescales in different situations (Choudhury *et al.*, 2022a, Torres-Sánchez *et al.*, 2021). For example, during blastocyst development, luminal pressure doubles, leading to changes in cortical tension and cellular strain (Chan *et al.*, 2019).

In the case of epithelial domes, Latorre *et al.* (2018) observed a broad spectrum of pressure levels throughout dome evolution, resulting in various cellular deformations and tissue behaviors including active-superelasticity. However, in this system, control is limited to the footprint of the domes, with no capability to control pressure and tension. To address this limitation, in this chapter, we will employ the monolayer inflator (MOLI) system to subject tissues to different strain and tension regimes and characterize the material response of epithelial tissues.

### **7.2 Measurement of dome mechanics**

To characterize the dynamics of the domes, we assumed that the shape of domes closely follows a spherical cap geometry, and hence we focused on the midsection

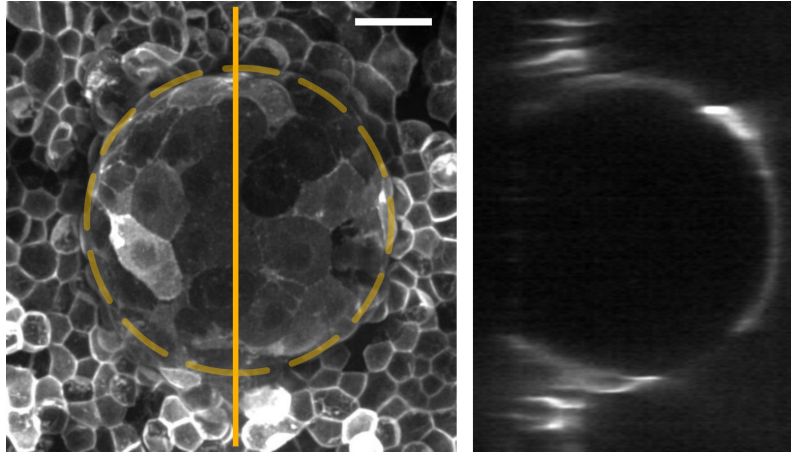


**Figure 7.1: Epithelial dome generated by the MOLI device:** Maximum intensity projection of an MDCK dome (Left). Dashed yellow line indicates the dome's footprint. Vertical yellow line crosses the center of the footprint, where the cross-section (Right) shows the spherical shape of the dome. MDCK Cells were expressing CIBN CAAX GFP-488. Pressure, 200 Pa. Scale bar is 20 $\mu m$ .

(see Figure 7.1). This approximation is reasonable for domes with circular footprint. For spherical domes supporting a membrane state of stress, mechanical equilibrium tangential to the surface implies that tension is isotropic and uniform tension, whereas mechanical equilibrium normal to the surface is expressed by Laplace's law (Latorre *et al.*, 2018). However, MOLI can also be applied to map the heterogeneous and anisotropic tension of non-spherical domes, e.g. resulting from non-circular footprints, applying curved Monolayer Stress Microscopy (Marín-Llauradó *et al.*, 2022).

From the cross-section, we measured the height  $h$  and base radius  $a$  of each dome, which allowed us to calculate the radius of curvature  $R$  as

$$R = \frac{h^2 + a^2}{2h}. \quad (7.1)$$

Additionally, MOLI provides a direct readout of pressure  $\Delta P$ , allowing us to compute the tension ( $\sigma$ ) using Laplace's law

$$\sigma = \frac{\Delta P R}{2}. \quad (7.2)$$

To quantify dome deformation, we used the areal strain measure, which is defined as the difference between the dome surface area ( $A$ ) and the area of the footprint ( $A_0$ )

normalized by the latter, leading to

$$\epsilon = \frac{A - A_0}{A_0} = \frac{\pi(h^2 + a^2) - \pi a^2}{\pi a^2} = \frac{h^2}{a^2}. \quad (7.3)$$

To obtain the temporal evolution of the dome's geometry, we generated kymographs of the top section of the domes. These kymographs provide the time evolution of  $h$ . Given  $a$  and the applied pressure as a function of time, we computed tensions and strain using the relations above.

### 7.3 Epithelial domes at constant pressure

First, we systematically applied varying pressures ranging from 0–400 Pa to the domes. However, we observed that domes could not form at pressures lower than 50–100 Pa due to cell-substrate adhesion forces. Conversely, high pressures resulted in tissue delamination beyond the boundary of the patterned footprint. We determined that 200 Pa allowed the domes to form without delamination, falling within the previously reported pressure range (Choudhury *et al.*, 2022b, Marín-Llauradó *et al.*, 2022).

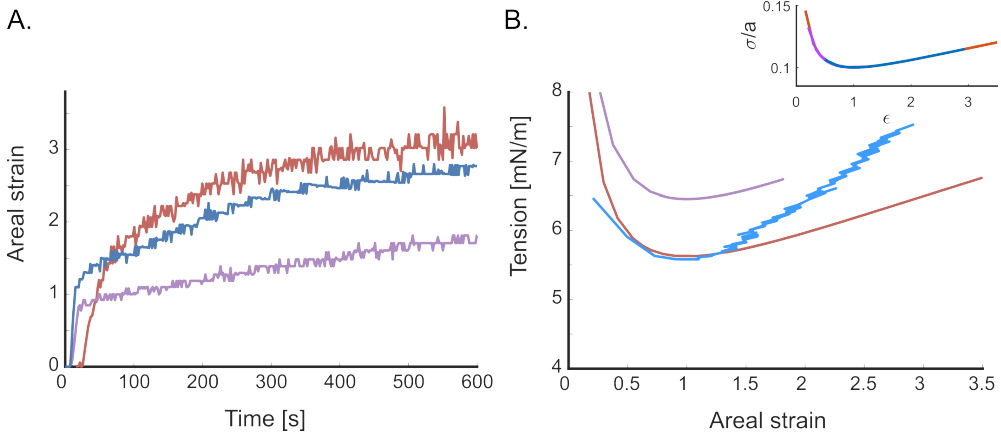


**Figure 7.2: Epithelial domes at constant pressure:** Dynamic response of three representative domes at a constant pressure of 200 Pa (Domes with base radius: red 56  $\mu\text{m}$ , blue 63  $\mu\text{m}$ , purple 42  $\mu\text{m}$ ): (A) Areal strain increases and reaches a steady state at around 5 minutes, and we can clearly see variability in the maximum strains. (B) The same domes produce a peculiar tension and strain curve. In an inset on top, all three curves collapse onto a single master curve, when tension  $\sigma$  is normalized by base radius  $a$  and plotted with respect to areal strain  $\epsilon$ . (representative of 12 domes)

When domes were subjected to a constant pressure of 200 Pa, they underwent a significant increase in areal strain during the first three to five minutes of pressure application. Following this initial increase, the areal strain reached a plateau and remained relatively constant for the next 5-10 minutes (see Figure 7.2 A). Notably, our measurements also indicated considerable variability in the maximum strain achieved by domes for the same pressure, with strains ranging from 50% to 300%. Nevertheless, the stabilization in strain across all the domes suggested that the epithelial tissue reached a mechanical steady state.

We then plotted the tension-strain relationship of these domes, systematically finding a non-monotonic curve similar to the Nike "swoosh" symbol (see Figure 7.2 B). At low strains, the tension within the domes is very high, followed by a decline to a minimum value at an areal strain of 100%, where the dome adopts a hemispherical shape. Tension then increases again, but the rate of increase is slower than the rate at which tension decreases at lower strains. This non-monotonic tension-strain curve is at odds with previous measurements of tension-strain relations in spontaneously fluctuating domes (Latorre *et al.*, 2018, Marín-Llauradó *et al.*, 2022) or in cell monolayers subjected to uniaxial stretch (Duque *et al.*, 2023). The fact that strains and tensions strongly varied from dome to dome but the minimum of tension was achieved precisely at 100% areal strain for all domes suggested that this behavior is related to the nature of our measurement.

Our measurement of the stress-strain relation only uses (1) mechanical equilibrium, encoded by Laplace's law, and (2) the geometrical relations between the radius of curvature  $R$  of the dome, the footprint radius  $a$ , the height  $h$  and the areal strain  $\epsilon$ . The geometric Eqs. (7.1,7.3) can be combined to find an explicit relation between radius of curvature and strain

$$R = \frac{h^2/a^2 + 1}{2h/a^2} = a \frac{\epsilon + 1}{\sqrt{\epsilon}}, \quad (7.4)$$

which when plugged into Laplace's law in Eq. (7.2) results in

$$\frac{\sigma}{a\Delta P} = \frac{1}{4} \frac{\epsilon + 1}{\sqrt{\epsilon}}. \quad (7.5)$$

This relation relates two non-dimensional quantities. Since in the experiments reported in Figure 7.2 pressure  $\Delta P$  and footprint radius  $a$  are constant, this relation shows that tension should be proportional to  $(\epsilon + 1)/\sqrt{\epsilon}$  irrespective of the mechanical

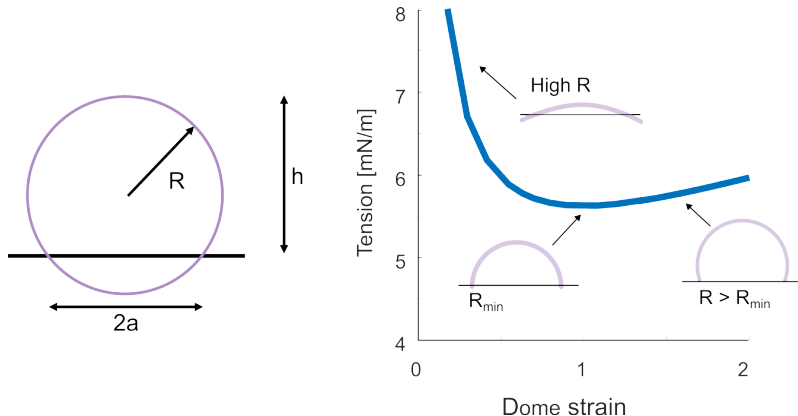


**Figure 7.3: Illustrative explanation for isobaric curve:** Tension and strain are related to each other through the geometric constraint of a spherical cap. Here, the base radius ( $a$ ) is constant, so the radius of curvature is almost infinite for domes with very small strains ( $< 0.05$ ). As the strain increases, the radius of curvature decreases to a minimum corresponding to the base radius. Then it continues to increase again.

response of the tissue, as a result of geometry and mechanical equilibrium. For small strains ( $\epsilon \ll 1$ ), we have  $\sigma \propto 1/\sqrt{\epsilon}$ , whereas for large strains  $\epsilon \gg 1$ , we have  $\sigma \propto \sqrt{\epsilon}$  in agreement with the non-monotonic measured stress-strain curves. A geometric interpretation of the isobaric curve is shown in Figure 7.3, which reflects the fact that the radius of curvature of a spherical dome of fixed footprint is minimum when the dome is half sphere. When represented according to Eq. (7.5), all tension-strain curves collapse to a master curve reflecting the hypotheses of the measurement (see Fig. 7.2 B inset).

The previous discussion shows that Eq. (7.5) alone does not say anything about the mechanical response of the epithelial monolayer. It just characterizes the locus of tension-strain states of a spherical dome that respects the physical constraint of mechanical equilibrium. This relation also shows the non-trivial relation between the pressure-controlled mechanical ensemble of MOLI, very natural for pressurized lumens, and more common tension-controlled or strain-controlled ensembles. Hence, the dynamics of Figure 7.2 A cannot be interpreted as neither stress-relaxation nor creep experiments. This figure also shows that during their trajectory along the isobaric curve, the tissue experiences a time-dependent relaxation towards a steady-state strain, and hence to a steady-state tension according to the isobaric relation Eq. (7.5). Using a mechanical analogy, we can interpret that during these dynamics out-of-equilibrium (viscous) stresses relax and we are left with a pair  $(\epsilon^*, \sigma^*)_{\Delta P}$  along

a steady-state constitutive relation  $\sigma^{ss}(\epsilon)$  of the tissue. In the next section, we discuss how to use this principle to measure this constitutive relation.

## 7.4 Steady-state constitutive relation of epithelia

Viewing the cell monolayer as a material sheet, we sought to characterize the stress-strain relation  $\sigma^{ss}(\epsilon)$  under quasi-static or steady-state conditions using MOLI (Duque *et al.*, 2023, Latorre *et al.*, 2018). If such a relation were to exist, they it should intersect the family of isobaric curves as we sweep  $\Delta P$ , see Fig. 7.4 A, and hence, in principle, we should be able to track it by identifying steady state pairs  $(\epsilon^*, \sigma^*)_{\Delta P}$  at different pressures.

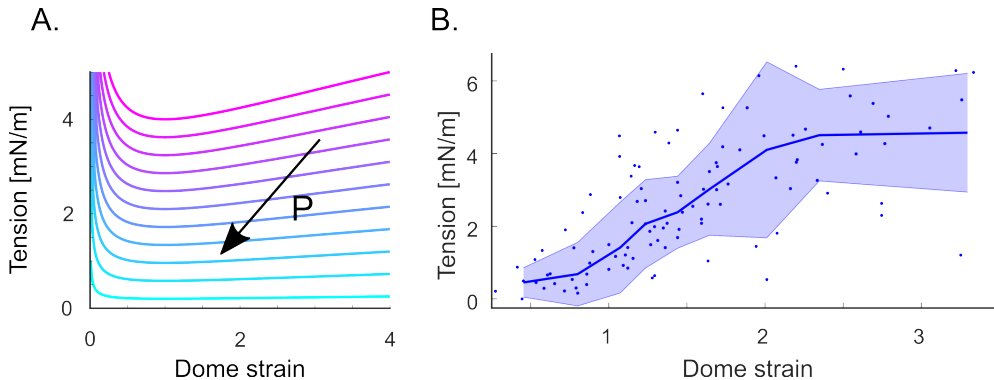


**Figure 7.4: Steady-state constitutive Relation of epithelial monolayers:** (A) We set up experiments to probe the steady state at different pressures. We will start from the highest pressure, move along the isobaric line and achieve a steady state, and then move down to the next curve, and so on. (B) The constitutive relation between dome strain and tissue tension was experimentally obtained ( $n=12$ ). The line and shaded area represent the median and standard deviation, respectively, by binning 13 points in each bin.

To implement this approach, progressively increasing pressure to track steady states is not feasible due to the existence of a pressure threshold for delamination. Instead, we swept pressures by deflating domes in steps. Specifically, we applied a pressure of 200 Pa for 5 minutes, allowing the dome to reach a steady state. We then reduced the pressure in increments of 20 Pa, allowing the dome to reach steady state at each step. This process continued until the dome was completely deflated. This approach allowed us to collect steady state tension-strain pairs that should lie on the curve  $\sigma^{ss}(\epsilon)$ , hence mapping the steady-state constitutive relation of the tissue,

Fig. 7.4 B. The resulting constitutive relation showed an initial increase in tension with strain for lower strains. For larger strains, the tension plateaued, consistent with earlier studies on MDCK domes. It is important to note the significant variability in dome-to-dome tension, with recorded tensions around 4.5 mN/m with the same order of magnitude as those in previous studies (Latorre *et al.*, 2018, Marín-Llauradó *et al.*, 2022). In summary, we show that MOLI can be used to map the steady-state constitutive relation of a tissue by stepwise pressure reduction. We probe next the dynamical material response.

## 7.5 Dynamics of the epithelial domes

Next, we investigated the dynamic material response of the domes by conducting cyclic pressurization experiments. We subjected the domes to a triangular wave of pressure with a magnitude of 200 Pa at three distinct timescales, as depicted in Figure 7.5. The selected timescales of 20 s, 266 s, and 2000 s were based on existing literature on tissue remodeling, particularly the work of Khalilgharibi *et al.* (2019) and Casares *et al.* (2015). These studies demonstrated that stress relaxation in tissues occurs from tens of seconds to minute timescales due to F-actin remodeling and myosin-driven contractility. Even faster deformation rates, which have been studied using different methods (Khalilgharibi *et al.*, 2019), are not accessible to the current implementation of MOLI because of the microscope's imaging speed.

	Fast	Moderate	Slow
Time period (s)	20	266	2000
Rates (Pa/s)	20	1.5	0.2

Table 7.1: Pressure rates used for cyclic stretching experiments

For the fastest cycles, we observed that the maximum strain achieved by the domes in each cycle increased until they reached a steady state oscillation around 600 seconds. The experiment was conducted over 1200 seconds, equivalent to 60 cycles, during which we observed a cumulative buildup of strain over time. In the loading phase, the domes underwent stretching, while during the unloading phase, they experienced unstretching but failed to revert to zero strain after the initial cycles. In the concluding cycles, we noted that the dome oscillated between two distinct states of strain, resembling a limit cycle (see Fig. 7.5 B top).

A similar response was observed for the moderate cycles, where the domes were stretched for five cycles of 266 s each. Strain accumulated in the first two cycles, with strains reaching higher values than those observed in the fast case (see Fig. 7.5 B middle). After the third cycle, the dome appeared to reach a stable limit cycle.

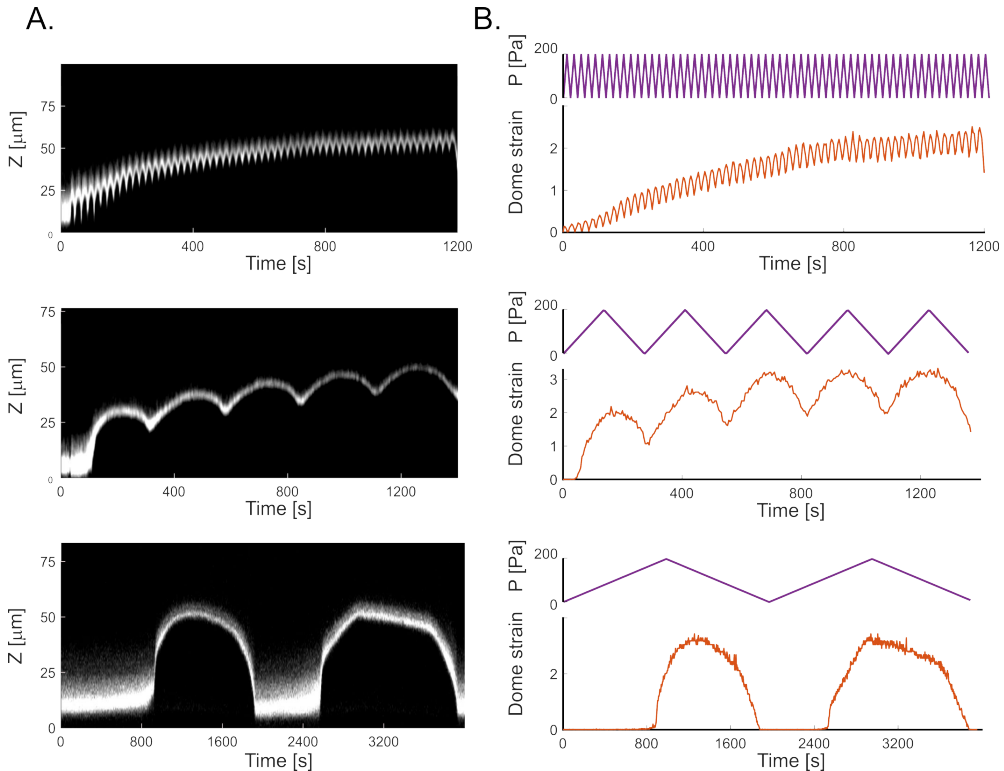


**Figure 7.5: Dynamic response of Epithelia:** (A) The XZ plane images and kymographs of domes subjected to cyclic pressure between 0 to 200 Pa with rates of 20, 1.5, and 0.2  $\text{Pa/s}$ . The kymographs generated along the midsection of the domes indicated by yellow dotted lines. These indicate the evolution of height of the domes with respect to time. (B) The strain response of domes to cyclic pressure with different rates. Magenta represents pressure and red represents strain with respect to time. For A, B,  $n = 7$  domes for 20  $\text{Pa/s}$ ,  $n = 8$  for 1.5  $\text{Pa/s}$ , and  $n = 7$  for 0.2  $\text{Pa/s}$ .

In the slowest loading experiments, consisting of two cycles of 2000 s, we observed that the domes did not form at lower pressures. As discussed earlier, the domes remained attached until a pressure of 100–150 Pa was attained, beyond which they underwent rapid inflation, leading to high strains of 200–350 %. A clear phase-shift was visible between pressure and strain. In contrast with the previous two cases, the

second cycle did not reach a higher strain as compared to the first one (see Fig. 7.5 B bottom). In these experiments, cells were able to stretch four times their original area and return to the original size at the end of each cycle.

These experiments clearly demonstrated the rate-dependent response of the domes, with faster rates resulting in lower strains and progressive strain accumulation and slower rates allowing for reversibly large deformations. Several features such the remanent strain after a cycle, its ratcheting behavior, the existence of limit cycles, or the phase-shift are suggestive of a viscoelastic material response. We further examine this response next with the help of a computational model.

## 7.6 Active gel tissue model

Viscoelasticity has been invoked to interpret mechanical measurements of cells and tissues in a variety of contexts, and experimental setups (Pullarkat *et al.*, 2007), including individual cell-cell junctions (Clément *et al.*, 2017), single cells (Fischer-Friedrich *et al.*, 2016, Wottawah *et al.*, 2005), or cell monolayers (Fernandez *et al.*, 2007, Khalilgharibi *et al.*, 2019). In all these examples, experimental curves such as those in Figure 7.5 are fitted by variants of phenomenological rheological models, which may include the short-time power-law rheology measured at cellular and tissue scales (Bonfanti *et al.*, 2020, Khalilgharibi *et al.*, 2019, Pullarkat *et al.*, 2007). However, because MOLI allows us to simultaneously measure tissue rheology and image dome and cellular shape in 3D, we sought to pair this device with a computational model that more realistically describes epithelial domes as compared to the common 1D rheological models. Furthermore, the connection between the mechanics of cell monolayers and the structure and dynamics of sub-cellular load-bearing structures, such as the actin or the intermediate filament cytoskeletons is increasingly understood (Duque *et al.*, 2023, Khalilgharibi *et al.*, 2019, Latorre *et al.*, 2018). These proteins and their dynamics can be visualized and perturbed pharmacologically or optogenetically within MOLI.

For these reasons, we established a close collaboration between the author of the present thesis and Adam Ouzeri, simultaneously developing a theoretical and computational thesis. The main idea of the model is summarized next, and we refer to Adam Ouzeri's forthcoming thesis in the same doctoral program for further details. The model geometrically describes the tissue as a collection of individual cells in 3D defined by triangulations of their bounding surfaces, very much like a vertex model

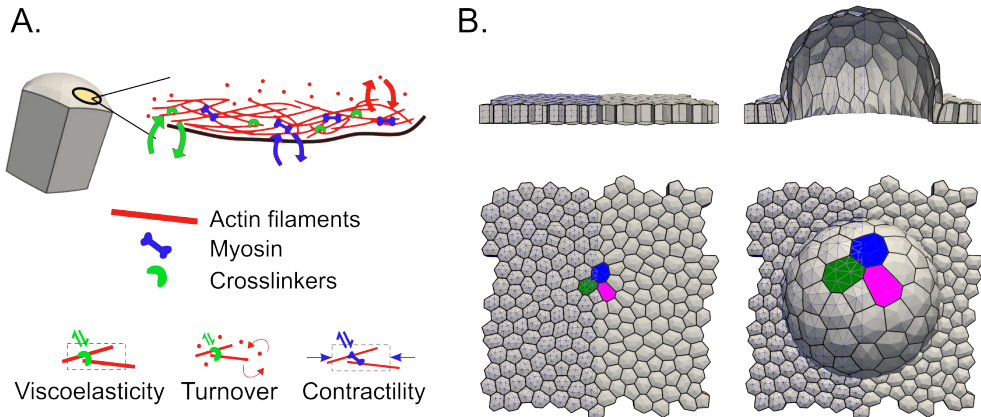


**Figure 7.6: Active gel tissue model:** (A) The cell is modeled as an active gel of cortex, which mainly comprises three aspects: viscoelasticity of the network, turnover dynamics, and active contractility. (B) These cells can be assembled into a tissue that can be used to perform in-silico experiments. An example of this is the digital dome being inflated, color is highlighting individual cells increasing their area.

with curved faces (Alt *et al.*, 2017, Pérez-González *et al.*, 2021). However, rather than describing the mechanics of the system using surface tensions, springs or dashpots, it aims to connect tissue mechanics and sub-cellular cytoskeletal dynamics, Figure 7.6 A.

Focusing on the cortical actin cytoskeleton as a major determinant of epithelial mechanics (Duque *et al.*, 2023, Khalilgharibi *et al.*, 2019, Latorre *et al.*, 2018), we describe this active interface using the framework of active gel theory (Prost *et al.*, 2015). Active gels provide a coarse-grained continuum description of the actin cortex. In a minimal active gel model of the actin cortex, stresses in the gel have a viscous component capturing the stress relaxation as transient crosslinkers turnover, and an active and density-dependent component capturing contractility due to myosin motors. Cortical materials are advected by the flow, and also polymerize and depolymerize. These models can be enriched to account for multiple cytoskeletal components, for the signaling networks that control their behavior, for their nematic or polar architecture, or for the elastic stresses supported at short time-scales. These models have successfully explained a number of biological behaviors including amoeboid motion of single cells (Callan-Jones and Voituriez, 2013) or the formation of supracellular actin patterns (Hannezo *et al.*, 2015), and can be improved by comparison with controlled experiments and with agent-based discrete simulations (Cortes *et al.*, 2020).

The tissue model considered here describes each cellular surface in the cell monolayer as an active gel interface. Cell volume is kept constant. The modeling framework can be systematically improved by including other mechanical modules of epithelial cells and their interactions, such as cell-volume regulation, intermediate filaments, cell-cell adhesions, the nucleus, or the plasma membrane. Here, in addition to the active gel surfaces, we include an unspecific mechanical barrier to excessive cellular stretch or compression that becomes active at large strains to capture the tissue strain-stiffening in tension, e.g. due to intermediate filaments (Duque *et al.*, 2023, Latorre *et al.*, 2018), and the expected stiffening in compression due to nuclear resistance.

The active gel model used here describes the cortex in terms of its shape and of its thickness or cortical areal density  $\rho$ , governed by a mass conservation equation accounting for advection, polymerization and depolymerization, which maintains a cortical thickness at steady-state. When deformed rapidly, the crosslinked actin filament network behaves like an elastic network of semi-flexible filaments, which we describe with a hyperelastic model characterized by Lamé parameters  $(\lambda, \mu)$ . Consequently, upon deformation, it can store elastic energy at short timescales. At longer timescales, the network dynamically reorganizes, dissipating the stored elastic energy and relaxing elastic stresses. For instance, the unbinding of a crosslinker in a deformed network will release elastic energy into the frictional environment and re-bind in a partially relaxed network. The dissipation of elastic stresses is represented by viscosity coefficient  $\eta$ . Mathematically, the model keeps track of the metric tensor as a multidimensional generalization of the resting length of the network, which evolves over time driven by elastic stresses. The contractile active tension in the network  $\gamma$  is hypothesized to be isotropic and proportional to cortical thickness as  $\gamma(\rho) = \xi\rho$ , with proportionality constant  $\xi$ .

Hence, in a steady-state, cortical density is uniform, elastic and viscous stresses vanish, and we are left with uniform surface tensions as in a conventional vertex model. Out-of-equilibrium, the dynamics of the tissue, and in particular its shape and mechanical behavior, are then direct consequences of the active gel surface dynamics assembled into a monolayer of cells with constant volume, Figure 7.6. In particular, three timescales emerge from the theoretical framework:

1. Turnover timescale  $t_{to} = 1/k_d$
2. Viscoelastic timescale  $t_{ve} = \eta/\lambda$
3. Viscoactive timescale  $t_{va} = \eta/\xi$

The turnover timescale is given by the depolymerization rate  $k_d$ . The viscoelastic timescale is a ratio of the viscous remodeling coefficient to the Lamé parameters, representing elasticity. Lastly, the viscoactive timescale is the ratio of the viscous remodeling coefficient to the coefficient of active tension. For instance, at time-scales smaller than  $t_{to}$ , cortical stretching or compression leads to deformation-induced changes in cortical thickness, which dissipate over time because of turnover. Likewise, at time-scales smaller than  $t_{ve}$ , the cortex behaves like an elastic interface whereas at times much larger than  $t_{ve}$  it flows like a viscous fluid.

Using this model, a virtual representation of a cell monolayer can be generated with specific boundary conditions. In particular, we can create a cell monolayer with regions that lack basal attachment to the substrate, which can be inflated into domes under pressure application, similar to the experimental setup, Figure 7.6 B. These simulations will be referred to as "digital domes" in subsequent discussions. By employing this model and comparing the results with the experimental data, we can effectively understand and investigate the biomechanical properties of epithelial tissues, specifically the contribution of the viscoelasticity of the actin cortex.

## 7.7 Active viscoelasticity of the epithelia

In this section, we interpret the experimental results within the context of the active gel tissue model. Consider an example where the tissue is step stretched biaxially. The actual area of apical and basal faces changes instantly, and becomes larger than the resting length. Consistent with volume conservation, lateral faces also change in area, and also in shape. Hence the cortex as an elastic network stores recoverable strain energy. However, as cross-links and filaments turnover, this energy dissipates. In the model, the metric tensor evolves over time in such a way that the resting area (and shape for lateral surfaces) progressively becomes equal to the actual area (shape), thus relaxing over time the elastic stresses (see Fig. 7.7 A). We call this time-dependent stresses associated with the relaxation of the metric tensor viscoelastic. On top of these stresses, the cortex sustains active stresses, which are also time-dependent because they are proportional to cortical density, and the step stretch instantly dilutes apical and basal faces and concentrates lateral faces, which then recover the steady-state thickness due to turnover. The net effect of such active viscoelastic behavior of individual faces on the tension of a tissue made of identical cells is shown in Figure 7.7 B. This figure depicts the stress relaxation dynamics of the tissue.

However, as discussed earlier, MOLI does not naturally probe a strain-controlled mechanical ensemble. Thus, simulations were conducted to mirror the experimental conditions. Upon subjecting the digital dome to constant pressure, consistent with our previous experimental observations, the digital dome reached a steady state strain while experiencing a reduction in tissue thickness as the cells stretched, Figures 7.8 A and 7.6 B. The remodeling of the cortex dissipates the viscoelastic stress and increases the active tension. At steady state, only the active tension remains balancing the externally applied pressure. The simulations show that the time to reach the steady state is mainly driven by the viscoelastic timescales. During such dynamics, the digital domes also produced the non-monotonous tension-strain relations observed experimentally, Figure 7.8 B.

To map the steady-state constitutive relation, we first quasi-statically increased pressure to obtain the blue curve in Figure 7.8 B. We then mirrored the experimental procedure by subjecting the digital domes to pressure steps, and then letting the

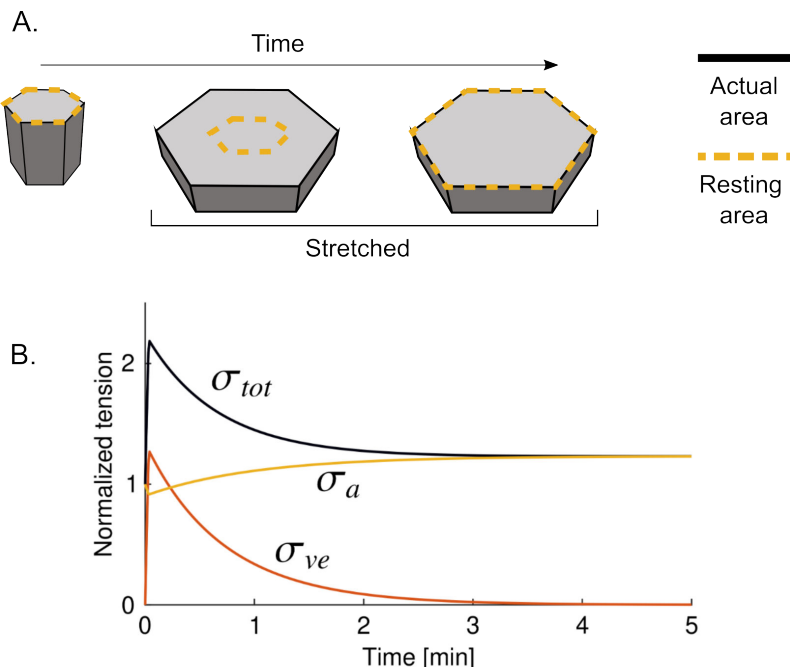


**Figure 7.7: Active viscoelastic response after step deformation:** (A) Illustration of a resting and actual area of a cell in a tissue during stretching. (B) Evolution of total tissue tension (black), viscoelastic stress (red), and active tension (yellow) in response to step deformation.

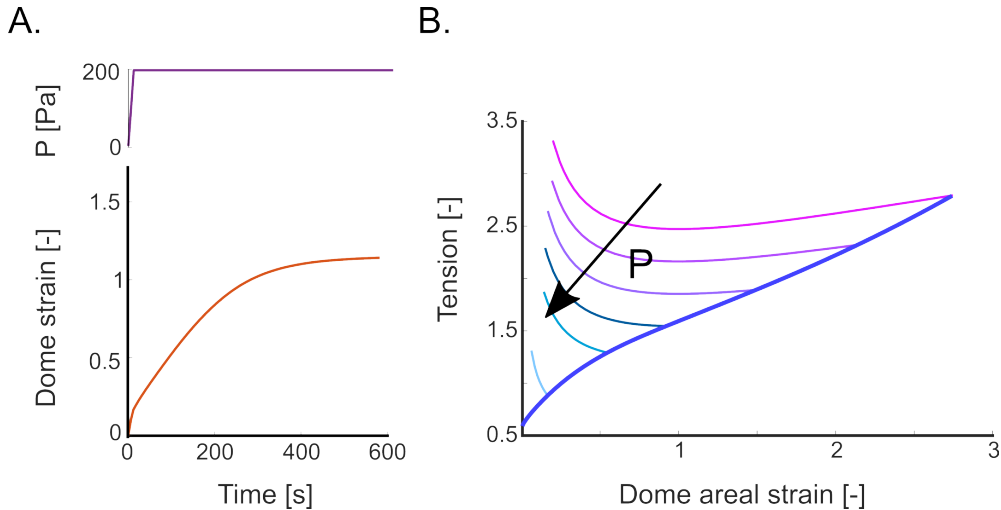


**Figure 7.8: Material response of the digital domes:** (A) When subjected to constant pressure, as in experiments, the digital dome inflated and reached a steady state. (B) These simulations also produced non-monotonic tension strain curves for different pressures, all leading to a steady state. The blue curve is the result of a quasi-static increase of pressure, which traces the locus of steady-state points obtained in long isobaric simulations. Tension reported here is non dimensional.

system reach a steady state. We found that these tension-strain pairs at steady state for different pressures retrace the blue quasi-static curve in Figure 7.8 B. This curve displays characteristics similar to those observed experimentally. The strain-stiffening at high strains can be attributed to the barrier mechanism introduced to limit high strains, which we did not attempt to fit to experimental measurements.

The effect of the remodeling timescale is particularly noticeable in cyclic stretching experiments. When digital domes are subjected to a cyclic pressure at rates that are slower than cortical dynamics, then the cortex remains close to steady state during cellular deformations. Hence, the stored elastic energy is rapidly dissipated as the strain increases, and the cortical thickness does not change significantly as turnover has time to restore the steady-state thickness. We observed that the resting area in the digital dome almost overlapped with the actual area (see Fig. 7.9 B bottom). This slow rate of 0.2 Pa/s provides cells with sufficient time to remodel and dissipate viscoelastic stresses. Viscoelastic and turnover timescales in simulations are around 10-30 s, which means that over a period of 2000 s, the dome stretches to considerably large strains of 250-300 % and returns to its original flat state.

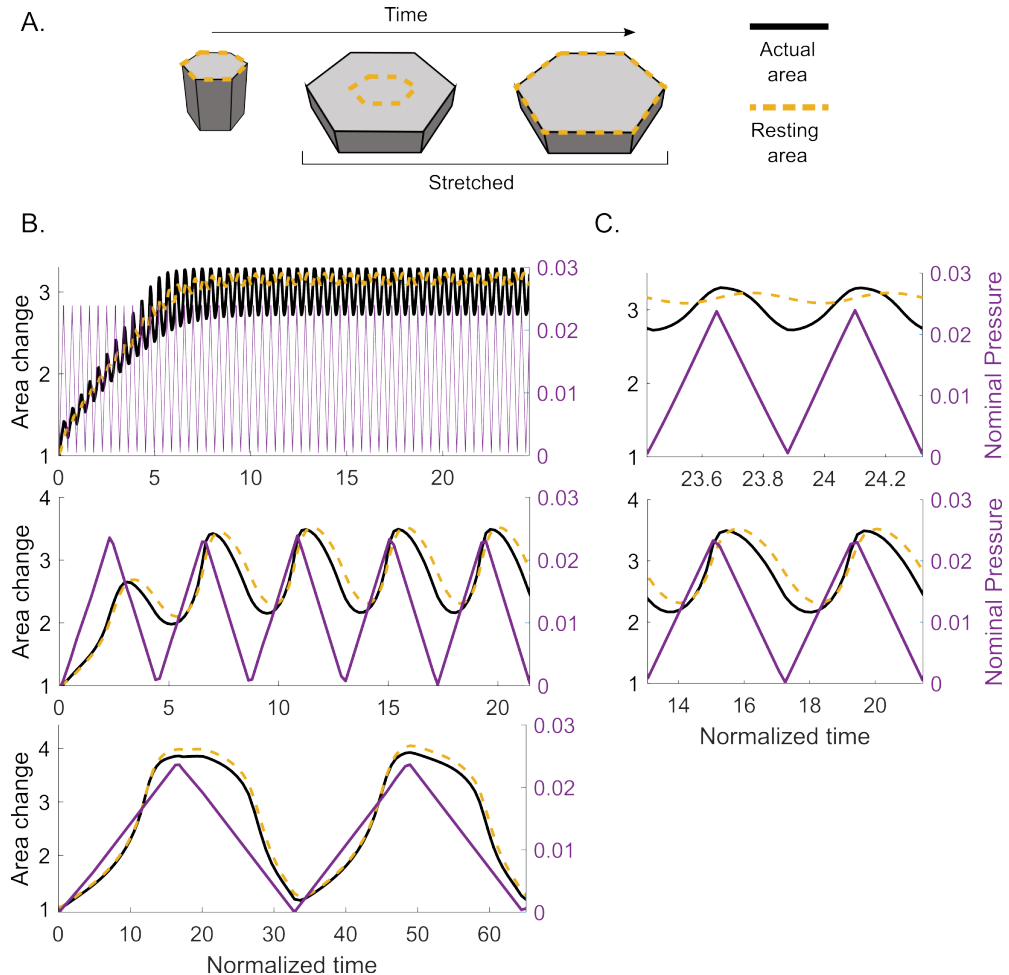


**Figure 7.9: Evolution of Resting and Actual Cell Areas in Response to Cyclic Pressure:** (A) Illustration of resting and actual cell areas in a monolayer during stretching. (B) Fold area change relative to the initial area, with three rows of panels showing the evolution of area change over normalized time. Digital domes were subjected to cycles with three different time intervals: 20 s (top), 266 s (middle), and 2000 s (bottom). (C) Inset of the last two cycles in the case of fast and moderate rates.

In contrast, when cells in a dome are subjected to cyclic pressure at rates faster than cortical dynamics, they accumulate strains due to insufficient time to dissipate viscoelastic stress. In this case, the actual area changes more rapidly than the viscoelastic and turnover timescales permit (see Fig. 7.9 B top). Consequently, along with the change in the actual area, the resting area also changes, but at a slower pace.

During deflation, the resting area decreases but cannot decrease completely before the next inflation cycle begins, causing the tissue to stretch further in a ratcheting behavior reported in individual cell junctions (Clément *et al.*, 2017). Eventually, a limit cycle is reached, wherein cells stably oscillate between two strains, and the resting area oscillates as well, but at a smaller amplitude (see Fig. 7.9 B top).

To sum up, the active gel model explains the material response of epithelial tissue depending on the rate at which pressure is applied. The concept of resting area enables us to interpret that slower rates allow for cell remodeling and dissipation of viscoelastic stress, while faster rates result in strain accumulation due to insufficient time for dissipation. This active viscoelastic behavior is the outcome of timescales associated with cortical remodeling.

## 7.8 Summary and Discussion

In this chapter, we investigated the mechanics of epithelial tissue by applying pressure at varying rates. Initially, we applied a constant pressure of 200 Pa, which led to the dynamic inflation of domes eventually reaching a steady state in strain. Due to the spherical geometry of the tissue and Laplace's law, we observed a non-monotonous tension-strain curve in response to the constant pressure. We identified such curves as an intrinsic feature of the isobaric mechanical ensemble with fixed footprint area, natural with MOLI. This understanding allowed us to trace steady-state tension strain curves from the steady-states at different pressures, and found constitutive relations with increasing tension with respect to strains at lower values, but appearing to plateau at higher strains.

Furthermore, our measurements showed that the domes accumulated strain through the cycles when probed with fast-changing pressure and reached a limit cycle in later cycles. However, when stretched slowly, the domes reached higher strains without accumulating strain at the end of the cycle. To understand the behavior of epithelial tissue, we used a modeling and computational framework, which explains the tissue mechanical response from the active viscoelasticity of the cell cortex (Ouzeri and Arroyo, 2023). The digital dome studies highlighted the interplay of different timescales, which are the reflection of the interaction between cortical turnover, crosslinker dynamics, and network reorganization.

Previous research has approached the viscoelastic rheology of cell monolayers using minimal rheological models involving springs and dashpots. One particularly

interesting model was developed by Khalilgharibi *et al.* (2019), which characterizes the response of a suspended monolayer to stretch and demonstrates that the dynamics are similar to that of a single cell, due to the role of the actomyosin cortex. They used a model with two springs in parallel, one of which can change its resting length dynamically. The model explains the relaxation of the monolayer, as the active contractility of the cortex changes the resting length of the active spring, which closely relates to our "resting area" concept.

Another study by Clément *et al.* (2017) found that viscoelastic dissipation could explain the shortening or elongation of cell junctions in *Drosophila* embryos. They demonstrated that the dissipation occurs at the minute timescale, which coincides with myosin pulses, and that actin turnover plays a key role in this dissipation. These pulses have a ratchet-like mechanical effect that drives junction shortening and causes tissue folding. This ratcheting effect is reminiscent of the cyclic stretching at faster rates, where cells stretch more and more every cycle. Similar to the authors of the study, we explain the strain accumulation by incomplete dissipation of viscoelastic stress due to deformation faster than the remodeling timescale. The multi-cellular model used here recovers these phenomenologies and relates them to cytoskeletal dynamics. More importantly, it is applicable to more general situations in which the cellular deformation are heterogeneous, as further discussed in the next chapter.

Regarding molecular components, although we did not use pharmacological treatments, the MOLI system can accommodate the introduction of drugs. Various components in the actin network enable cortical tension modulation through pharmacological interventions that target specific molecular targets (Cartagena-Rivera *et al.*, 2016). For instance, Latrunculin depolymerizes the actin network, while Blebbistatin decreases cortical tension by inhibiting myosin activity. Conversely, Calyculin-A enhances contractility by accelerating Myosin II phosphorylation. In future experiments, these pharmacological interventions could be used to identify the molecular pathways involved in the tissue's mechanical response.

Our experimental system focused on probing the response of suspended tissues at short timescales (minutes), which correspond to the timescale of actomyosin network remodeling. We did not observe any cellular rearrangement, extrusion, or division at this timescale in our system, except for rare exceptions. Long-term experiments were not performed, as they were outside the scope of this study due to the suspected involvement of other cytoskeletal components, such as intermediate filaments. Latorre *et al.* (2018) observed the activation of intermediate filaments

in extremely stretched cells (>300%) and proposed that this reorganization caused restiffening, preventing cells from stretching excessively. This observation motivated the strain-limiting mechanism imposed in our model.

Latorre *et al.* (2018) also demonstrated heterogeneity in cell stretching, attributed to a mechanism of active superelasticity. However, in our experiments, we did not observe the coexistence of stretched and super-stretched cells. This might be due to the relatively shorter timescales in our experiments compared to long-term and pulsating deformation of spontaneous domes.

A recently published study (Duque *et al.*, 2023) shows that strain stiffening at very large strains is dependent on the strain and strain rates. The tissue stiffens at higher strains, but for higher strain rates, the stiffening is more pronounced. They demonstrated that this response is due to the supracellular network of intermediate filaments. Because in MOLI we do not control strain directly but rather pressure, it is not straightforward to map our results and those in this study. However, it is possible in principle to control strain and strain rate by a feedback mechanism. We further note that in the model, we did not include any rate-dependence in the strain stiffening as proposed by Duque *et al.* (2023), but it can be easily incorporated as mechanistic and quantitative understanding of this process becomes available.

Having established the correspondence of our computational model and experiments in MOLI, which depicts the epithelium as an active viscoelastic material, we will harness in the next chapter this understanding to control dome shape transformations.

# **Chapter 8**

## **Epithelial Buckling: Transforming Domes into Folds**

### **8.1 Introduction**

Epithelial structures in biology exhibit a diverse range of shapes and sizes, including curved or folded forms. Understanding these structures can be complicated, particularly in the context of developmental biology. Interestingly, the etymology of the terms "development" and "complicated" provides insight into the importance of folding and unfolding processes. "Development" comes from the Old French word "*desvelopemens*," meaning "unfolding," which describes the morphogenesis of an organism. In contrast, "complicated" comes from the Latin word "*com-plicare*," meaning "folded together," which is fitting for describing the emergence of complex, folded structures in epithelial tissues.

By utilizing the MOLI tool, we can create 3D epithelial structures by inflating domes, thereby transforming a planar monolayer into a curved configuration. In this chapter, we will discuss how these structures can be made even more *complicated*.

### **8.2 Rapid deflation produces a buckling instability**

In the previous chapter, we discovered that domes subjected to constant pressure gradually inflate and eventually reach a steady state. Employing a computational framework, we interpreted that stretching induces viscoelastic stress and active

tension in the tissue. To achieve a steady state, cytoskeletal remodeling dissipates viscoelastic stress, and active tension increases to counterbalance the external pressure. Consequently, the epithelial tissue exhibits the characteristics of an active viscoelastic material.

Due to this active viscoelasticity, we observed that in cyclic pressure experiments with rates faster than remodeling timescales, the tissue deflates slower than the pressure decreases. This leads to strain accumulation in subsequent cycles. Based on these findings, we wondered if starting from an inflated dome at steady state, a rapid deflation at rates faster than viscoelastic relaxation may lead to compressive membrane tension in the tissue. To achieve negative tension, according to Laplace's law it is necessary to apply a negative pressure or suction. Compressive tension of slender structures is known to lead to buckling instabilities, by which the thin material layer relaxes compression by large out-of-plane displacements. Indeed, following the rapid deflation, the large resting area of the inflated tissue may not fit into the fixed footprint area. The excess area of the tissue would then be accommodated by the formation of folds following a buckling instability. Interestingly, because deflating domes rapidly stick to the substrate, Fig. 7.5, these buckling patterns may remain imprinted in the tissue for long times following the cortical relaxation times.

Although this argument is reasonable, and buckling has been produced by compressing suspended monolayers (Wyatt *et al.*, 2020), our monolayers are very tense, with cells very far from their tensionless aspect ratio, to start with. Furthermore, in addition to the viscoelastic stresses mentioned above that lead to compressive contributions upon fast deflation, the cell monolayer is also subjected to positive surface tension due to contractility, and previous work suggests that surface tension hinders buckling (Le Merrer *et al.*, 2012) although even rapidly deflating fluid bubbles may wrinkle (Oratis *et al.*, 2020).

To test this hypothesis, we used the computational model, can track the mechanical effects of deflation at both tissue and individual cell scales. We subjected digital domes at a steady state with 200 Pa pressure to deflation at a negative pressure of -50 Pa in 6 s (fast) and 600 s (slow). Simulations showed that slow deflation, slower than the remodeling timescales, allowed the tissue to continuously deflate without buckling before reaching negative pressure. However, when the tissue was deflated faster than cortical remodeling, viscoelastic stresses were not dissipated, and the digital dome buckled, producing folds (see Fig. 8.1).

During rapid deflation, when negative pressure is applied to the positively curved

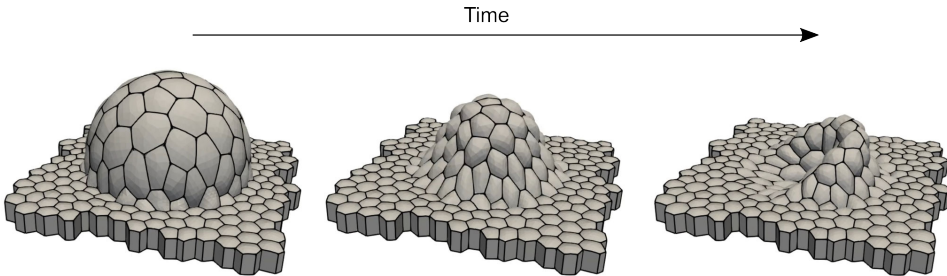


**Figure 8.1: Digital dome undergoing buckling:** A digital dome at a steady state is rapidly deflated to a negative pressure of  $-50\text{Pa}$ . Three snapshots show the buckling process.

dome, tissue tension becomes negative in accordance with Laplace's law. This results in compressive stress in the tissue, causing the dome's uniform curvature to become irregular, which is a hallmark of buckling instability (see Fig. 8.1). This is similar to the buckling of a thin plate subjected to in-plane compression, where compressive stress surpassing a critical threshold result in out-of-plane deformations.

To experimentally validate the simulation results, we designed experiments to identify the effect of hold and deflation timescales on buckling. The pressure profiles were decided as follows (see Fig. 8.2):

1. Initiate a linear increase in pressure from 0 to 200 Pa over a period of 10 seconds.
2. Apply constant pressure for varying hold times, chosen based on the timescales associated with actomyosin cytoskeletal remodeling (6, 60, and 600 s).
3. Decrease the pressure to -50 Pa at varying deflation rates (0.2, 2, 20, and 200 Pa/s) which correspond to deflation times (1250, 125, 12.5, and 1.25 s).

We conducted experiments for all conditions and quantified the fraction of domes that underwent buckling. We relied on qualitative characterization of buckling events, assuming that a smooth and continuous curvature of the monolayer indicated the absence of buckling. Our results demonstrated that at the fastest deflation of 1.25 s, buckling occurred for all hold times, ranging from 6 s to 600 s, confirming the hypothesis that rapid deflation causes buckling (see Fig. 8.3 A-B). In contrast, slow deflation in 1250s rarely led to buckling, irrespective of the hold time (see Fig. 8.3 C-D). This suggests, as the model predicted, that the tissue can effectively remodel its cytoskeleton and adapt to drastic changes in area, avoiding buckling during slow deflation.

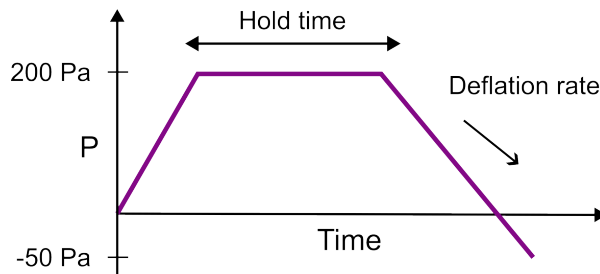


**Figure 8.2: Buckling protocol:** The pressure is increased to 200Pa for inflating the dome, and then the dome is given different amounts of time (hold time) to remodel before being deflated to -50Pa at different rates (deflation rate) to observe whether the dome buckles or not.

Our findings indicate that domes subjected to a 6 s hold time attained smaller strains at the end of the hold time compared to those with a 600 s hold time, consistent with the results from domes subjected to constant pressure (see Fig. 8.3 F). We found that domes tested with longer hold times had a higher fraction of buckling domes, even for moderately slow deflation (125 s). A diagram depicting the results demonstrates the relationship between hold time, deflation rate, and the likelihood of buckling. The trend shows that as hold time increases, buckling becomes more likely at faster deflation rates (refer to Fig. 8.3 E). Therefore, the dome's susceptibility to buckling is influenced by the interplay between hold time, which permits cytoskeletal remodeling at constant pressure and the progressive increase of the resting area, and deflation rate, which represents the timescale at which the tissue is compressed.

Furthermore, we observed a wide variety of transient folds in the inflated buckling dome, which depended on the hold time. Buckling domes subjected to short hold times and fast deflation exhibited minor kinks in the folds, while others subjected to long hold times and fast deflation showed drastic changes in curvature (see Fig. 8.3 A-B).

To sum up, we experimentally validated the predictions made by the computational model that buckling in domes is a consequence of deflation being faster than cortical dynamics. In the next section, we image the buckling tissue at a higher resolution for closer look at transient folds.

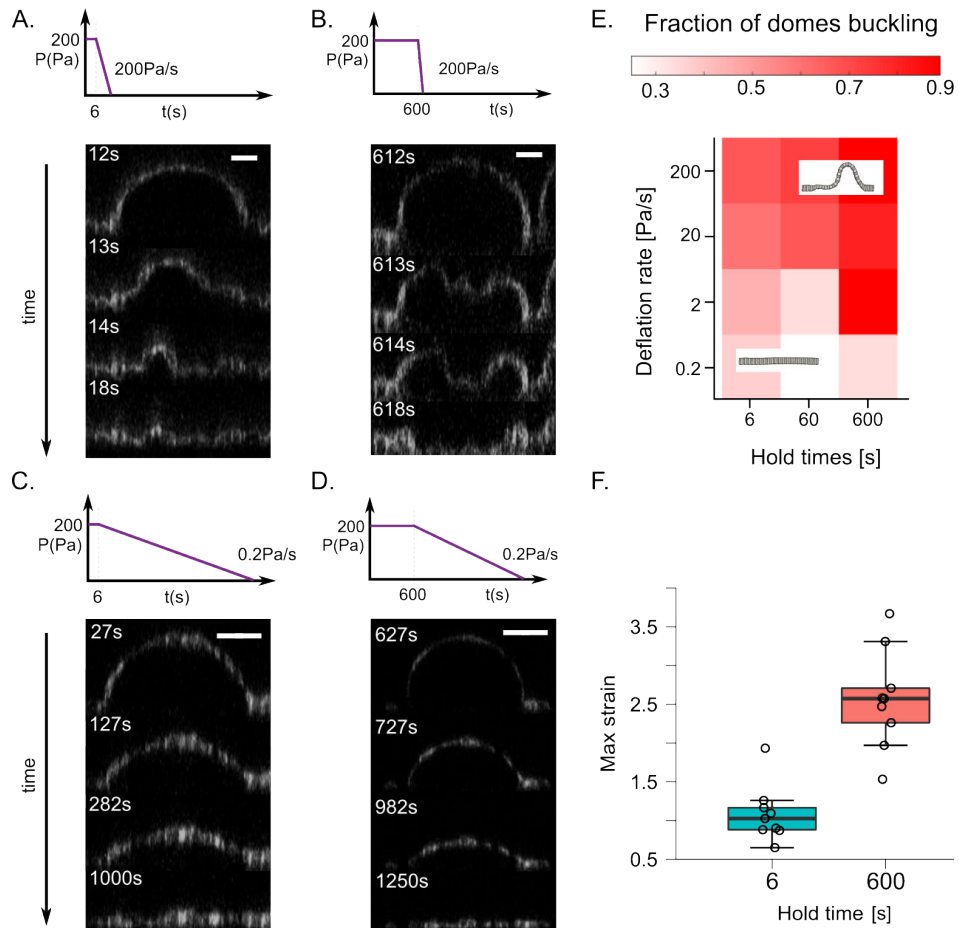


**Figure 8.3: Buckling conditions:** (A-D) Representative montages of dome deflation for experiments and model at different deflation rates of 200 and 0.2 Pa/s after holding pressure constant of 200 Pa for 6 and 600 s. Scale bars are 20  $\mu\text{m}$  for XZ. (E) Diagram representing fraction of domes buckling for different deflation rates and hold time. Showing the optimum conditions for the buckling. (F) The maximum strain achieved is lower for 6s hold time compared to 600s conditions.

### 8.3 Multiscale buckling

The observation of tissue buckling was evident in the confocal line scan images. However, individual junctions are also active viscoelastic thin sheets themselves, and it has been shown that rapid contractions during morphogenesis can lead to junctional buckling (Sumi *et al.*, 2018). To examine the dynamical shape transformation during rapid deflation at multiple scales, we adapted a variation of MOLI for use with light sheet microscopy. The higher resolution 3D images of the dome revealed a variety of cell thicknesses, with thicker regions caused by the bulging of the nucleus and thin regions at the cell periphery (see Fig. 8.4 C).

To further investigate the phenomenon of buckling, we repeated the experiments described in the previous section, with a deflation rate of 200 Pa/s and a hold time of 600 s. Observations under the light sheet microscope revealed additional features beyond tissue-scale buckling, including folds at cellular and subcellular scales. Upon closer inspection, we classified three levels of buckling: tissue, cellular, and subcellular.

At the tissue scale, buckling was apparent, with cells collectively transitioning from a uniform curvature to a distorted shape (see Fig. 8.4 A). At this level, we also observed folds occurring at the junctions between cells (see Fig. 8.4 B). At shorter length scales, we observed individual cells undergoing buckling (see Fig. 8.4 C).

In many instances, we observed buckling at even shorter length scales, which we refer to as subcellular buckling, as the folds in the membrane were distinct from the cell-level buckling. Localized folds and ruffles occurred in the thinnest parts of the stretched cells, where the membrane folded at shorter wavelengths (see Fig. 8.4 E). Interestingly, these folds occurred on both the apical and basal sides of the cells.

Epithelial cells have their membrane attached to the cortex through membrane-cortex attachment proteins such as ezrin, radixin, and moesin. This led us to assume that the subcellular buckling observed in our experiments is due to actin cortex buckling. To confirm this, we imaged the actin cortex while the dome was undergoing buckling using SPY actin staining, which showed that the actin cortex followed the exact shape of the membrane during buckling (see Fig. 8.4 G).

Moreover, we found that while some domes were not buckling at the tissue scale, they were still exhibiting buckling at the cell or subcellular level (see Fig. 8.4 D F). Furthermore, we found instances of simultaneous buckling at multiple length scales (refer to Fig. 8.4 H), indicating that these categories are not mutually exclusive.

In summary, our observations of tissue buckling, cellular buckling, and subcel-

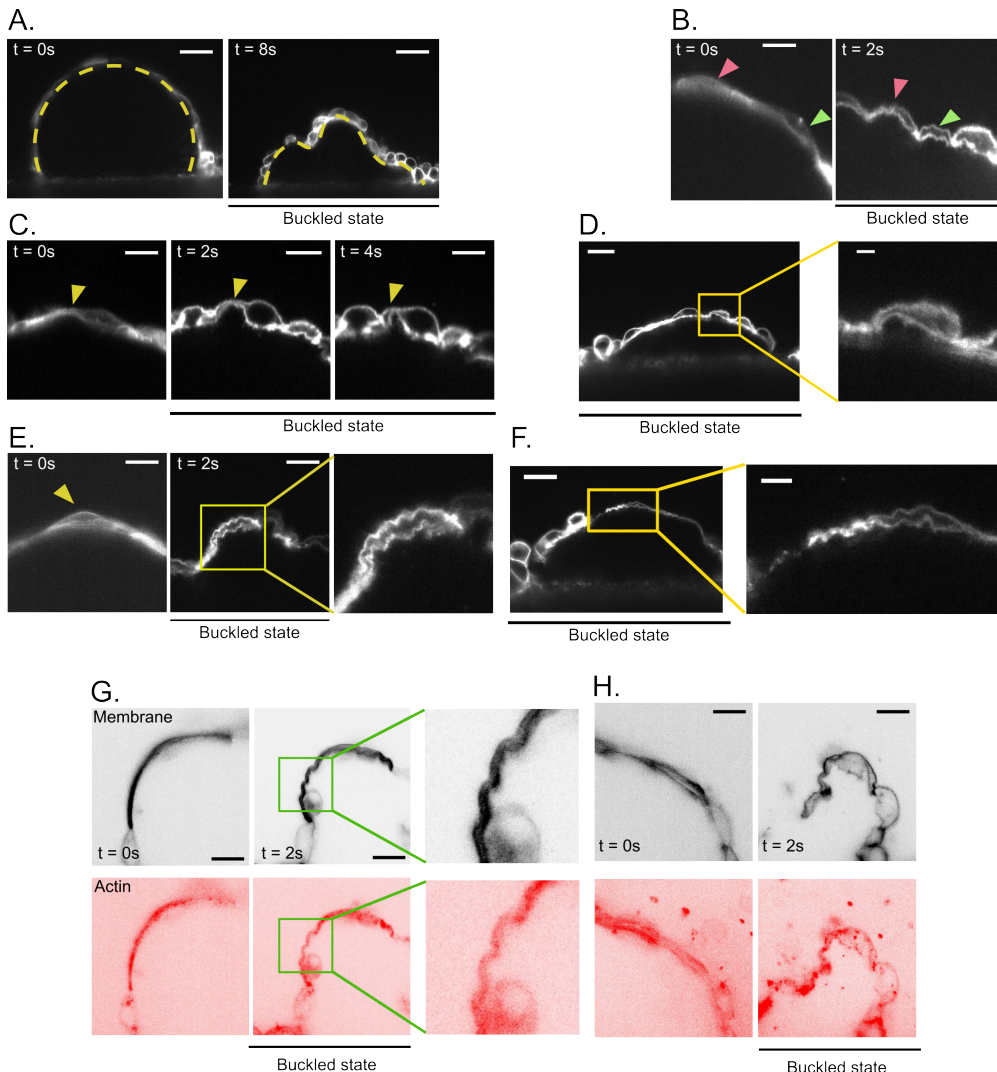


**Figure 8.4: Multiscale buckling:** (A) Midsection of a tissue dome undergoing buckling, with dotted yellow lines representing tissue curvature. Scalebar is 20 $\mu$ m. (B) Buckling event at the cell junction where cells buckle at a shorter length scale. (C) Localized subcellular buckling in a single cell with varying thickness from the nucleus to the periphery. (D) Buckling at the cellular level but not at the tissue level. Scalebar is 20 $\mu$ m. (E) Subcellular buckling resulting in the formation of ruffles at short wavelengths (inset). Scalebar is 5 $\mu$ m. (F) Buckling occurring at the subcellular level. Scalebar is 20 $\mu$ m with an inset scalebar of 5 $\mu$ m. (G) Cross-sections of the membrane and actin in cells undergoing subcellular buckling. Scalebar is 5 $\mu$ m. (H) Region of tissue undergoing buckling at multiple length scales. Scalebar is 5 $\mu$ m for (C,E,G,H).

lular buckling provide new insights into the mechanics of epithelial tissues. The hierarchical architecture of these biological interfaces is mirrored by a hierarchy of buckling scales. Each of these buckling scales provide distinct mechanisms to release compressive stresses in cortical surfaces.

## 8.4 Generating epithelial folds

In this section, we explored the formation of epithelial folds after deflation. During deflation, we observed the tissue making contact with the substrate in certain regions first, leading to the formation of folds in the regions where it made contact last (see Fig. 8.6 A-C). To investigate if there was any pattern to these folds, we examined buckling of spherical domes of different sizes. Indeed, larger domes result in more slender structures, known to exhibit more intricate buckling patterns. Our observations revealed two types of folding patterns emerging: accumulation along the periphery and folds in the middle (see Fig. 8.5).

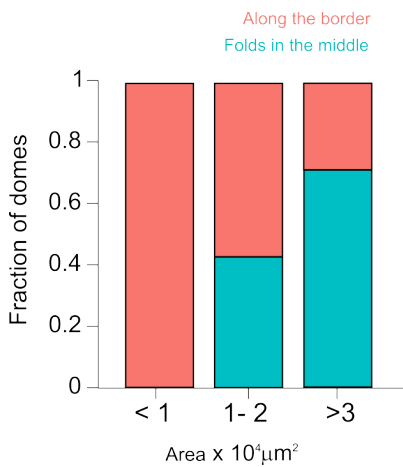


**Figure 8.5:**  
**Buckling patterns:**

Buckling patterns observed in differently sized digital domes. The domes were grouped into three size categories and two categories based on location of folds (along the border and in the middle). We found that larger domes are more likely to buckle into a network of folds compared to smaller ones.

For smaller domes with a footprint diameter smaller than 110 μm, we repeatedly observed that most of the buckling resulted in an accumulation around the periphery (see Fig. 8.6 A). The confocal time-lapse from the base gave the impression of an annular structure, but three-dimensional imaging of the folds revealed a crescent-shaped fold, taller on one side than the other. For larger domes with a footprint diameter greater than 300 μm, we observed instances of domes forming a network of folds in the middle, with multiple folds connecting each other by forming junctions (see Fig. 8.6 C). Finally, for intermediate-sized domes, we observed a mixture of accumula-

tion and folds, although the proportion of folds along the periphery decreased (see Fig. 8.5 ).

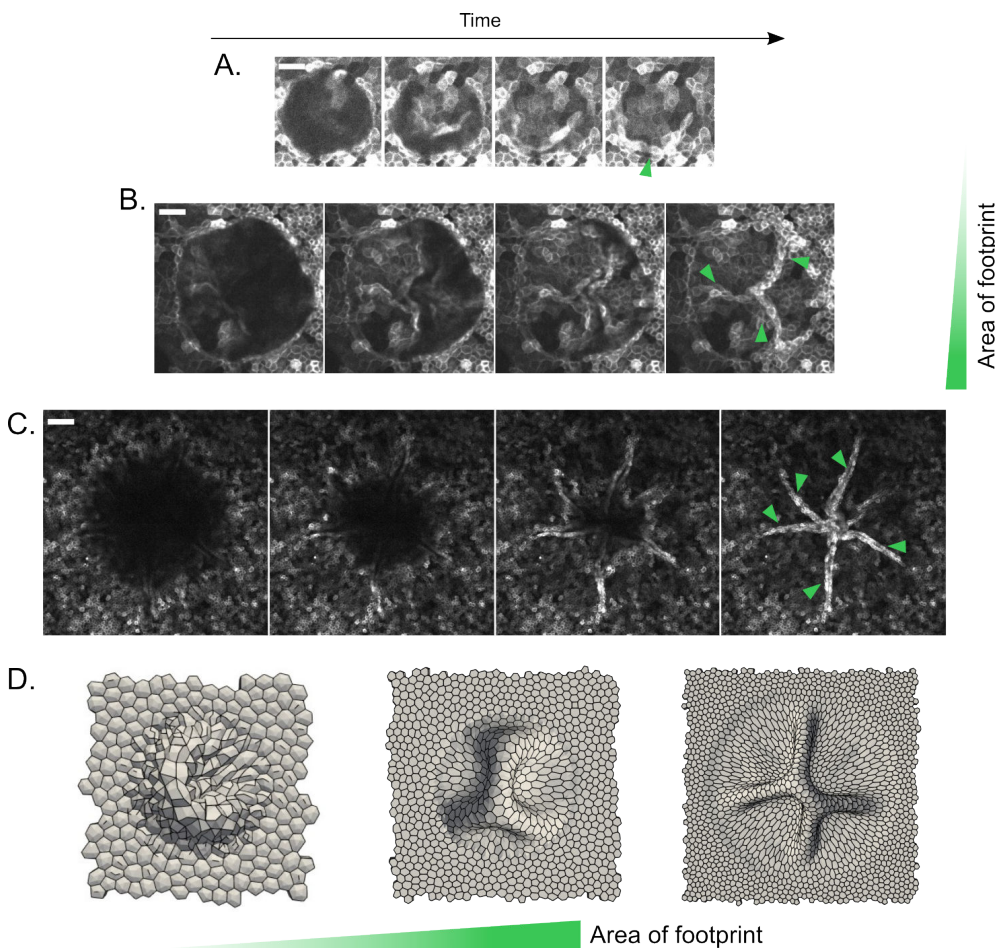


**Figure 8.6: Buckling patterns in spherical domes of varied size:** Representative examples of digital domes undergoing buckling with time-lapse of their basal cross-section (A-C). In the first frame, the onset of buckling is visible where the dome makes contact in the middle. Subsequent frames show more of the fold coming into view, and when the dome completely deflates, a fold is formed (indicated by the green arrow). Panel (D) shows the final outcome of buckling for digital domes of different sizes. Scale bar is  $20\mu m$

We also observed the same folding patterns in the digital domes when performing the same deflation experiments (see Fig. 8.6 D). Larger digital domes produced more radial folds, and smaller ones formed an accumulation on the side. Intermediate-sized digital domes showed a mixture of both patterns. Our findings suggest that the folding patterns may be governed by the size and shape of the dome. In the next section, we will attempt to control the folds by controlling the footprint shape.

## 8.5 Forming predictable folds

In this section, we explore the formation of predictable folds by deflating epithelial domes. While size provides some degree of control on the buckling pattern of spherical domes, because of their high symmetry and the characteristic symmetry-breaking of buckling patterns, the geometry of the resulting folds is very difficult to control. To break symmetry and guide buckling, we generated large digital domes of the same footprint area but with distinct geometries, including an ellipsoidal and a triangular shape. Remarkably, we found that the digital domes buckled into predictable patterns, with the ellipsoidal shape forming a line along the major axis and the triangular shape forming a Y-shaped network of folds.

To test the dependence of shape and size on folds, we conducted experiments using MOLI with ellipsoidal domes of varying sizes. Our observations revealed that larger ellipsoidal domes buckle into a fold along their major axis, just like digital domes, while smaller ellipsoidal domes produced a similar peripheral accumulation as spherical domes (see Fig 8.7 A). This suggests that only larger domes, regardless of their shape, possess the capability to produce folds in the middle.

Furthermore, we found that triangular domes buckled into a Y-shaped network of folds that resembled the pattern observed in digital domes (see Fig 8.7 D). The timelapse of buckling indicated that the vertices of the triangular domes pushed the buckling along the medians of the triangle (see Fig 8.7 C).

We observed that the folds exhibited variability in terms of stability, with some dissipating into a monolayer while others remaining intact and even forming attachments with each other. These folded structures were stable for several hours and could be imaged for over 12 hours (see Fig 8.7 E-F). Interestingly, when immediately inflated, these folds would unfurl into a smooth dome again.

Our results suggest that the MOLI system could provide a novel way of generating epithelial folds, with potential applications in tissue engineering. These results

demonstrate that by controlling a few mechanical parameters such as geometry and pressure, it is possible to harness active viscoelasticity and buckling to program epithelial folds.

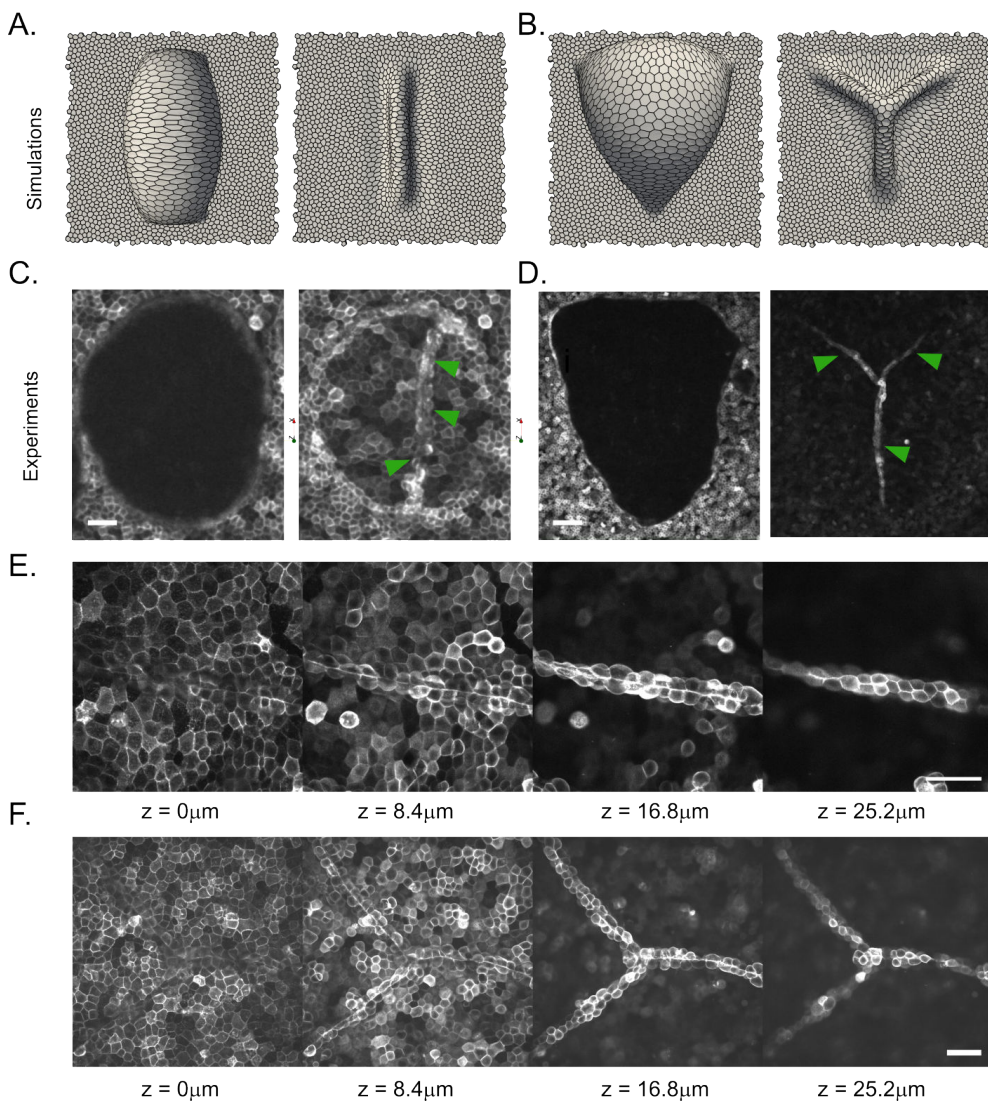


**Figure 8.7: Controlling the patterns of fold:** A-B Simulations show digital models of ellipsoidal and triangular domes buckled into line and Y-shaped junctions. C-D Experimental results confirm the simulation findings. E-F Confocal z-stack images show the folds in the case of a line and Y-shaped junction. Scale bar is  $50\mu\text{m}$ .

## 8.6 Summary and Discussion

In this chapter, we investigated the buckling response of epithelial tissue to deflation and its relationship with actin remodeling timescales. We utilized our device to generate domes from flat monolayers and observed buckling occurring at various scales, from the tissue level down to the actin cortex of individual cells. Our results revealed that buckling is triggered when deflation occurs more rapidly than actin can remodel. We also explored the patterns of folding that emerge from differently sized and shaped domes and proposed a novel method of creating controlled folds from planar monolayers. With the aid of computational models, we demonstrated the engineering potential of the dome system to produce structured folds by manipulating footprint geometry and pressure.

The prevalence of mechanical instabilities in biological systems is well established, and buckling in MDCK epithelial monolayers has been observed through various methods, including growth in confinement or direct compression (Trushko *et al.*, 2020, Wyatt *et al.*, 2020). Wyatt *et al.* demonstrated that uniaxial compression beyond 35% strain can cause epithelial monolayers to buckle out of plane, and active contractility can recover the deformation within tens of seconds depending on the degree of compression. These buckles were essentially one-dimensional, whereas our study allows us to examine the much more challenging situation of biaxial buckling. We further provides mechanistic insights into the buckling process and its implications for tissue architecture at multiple scales, which has not been previously explored.

Our results highlight the hierarchical structure of epithelial tissue, which is composed of various components that sustain deformations and forces at different levels. The actin cytoskeleton plays a crucial role in defining the shape of cells and tissues at multiple scales (Clarke and Martin, 2021). A cell monolayer can be viewed as an assembly of cells with their own surface tension and material properties, implying that a material with different length scales would buckle at different length scales. The conditions under which a tissue releases compressive stresses at a given scale and the biological consequences remain to be understood.

The short-wavelength folds resulting from subcellular buckling are an intriguing aspect to consider. It is important to note that actin buckling is not a novel phenomenon, and minimal models of actin filaments with myosin motors on a lipid membrane have demonstrated that myosin-induced contraction leads to actin filament buckling (Costa *et al.*, 2002, Murrell and Gardel, 2012, Wang and Qian, 2019). Re-

searchers have also reported multiple modes of buckling and wrinkling in membrane-actin droplets, depending on the thickness (Kusters *et al.*, 2019). Interestingly, they found that thin shells undergo buckling and produce wrinkles in the membrane but not in actin, indicating the possibility of different modes of buckling within a cell, which is closely related to what we observed in our experiments. In the future, faster 3D confocal imaging could enable further quantitative analysis of these transient folds.

Our findings on tissue-scale buckling can be related to modes of buckling in thin shells. Our computational model suggests that the cortex behaves like a hyperelastic material at short timescales, as in our case, where the tissues are deflated at a rapid rate. Analogous results can be expected if we repeated the experiment with elastic shells. Elastic shell buckling exhibits similar aspects, including the folds and patterns that emerge when different sized shells buckle. Localized defects engineered in the shells can also influence the sensitivity of buckling pressure (Lee *et al.*, 2016). We speculate that the non-uniform thickness of the cells, with thicker regions near the nucleus and thinner regions at the edges, provide the defects in thin shell geometry that result in localized folds. Future studies that quantify the relationship between the shell thickness and the emergence of folds may shed light on the precise mechanisms underlying the formation of subcellular folds in our experiments.

The slenderness, defined as the ratio of dome radius to thickness, provides a guide to understanding the different modes of buckling. Shells with high slenderness ratios are expected to exhibit higher modes of buckling compared to thicker shells. However, our experiments go beyond mere understanding of the system and demonstrate that we can program folds by controlling two parameters: geometry and pressure. For non-spherical domes, anisotropic stresses are observed along the axes of the elliptical footprint for ellipsoidal domes (Marín-Llauradó *et al.*, 2022). These stresses can orient the folding in a particular direction to generate a programmed fold, such as Y junctions on the sides of a rectangular footprint. A recent study has shown that confining elastic shells in smaller areas produces orderly wrinkles that depend on the curvature of the shell, which can be predicted by analytical solutions (Tobasco *et al.*, 2022). We note however that the predicted orientations of folds are orthogonal to those in our domes, highlighting the subtlety of predicting wrinkle patterns. Further advances in understanding the geometric and mechanical rules that control wrinkling patterns, combined with our experimental results, may offer insights into future tissue engineering applications.

In summary, this thesis presents a novel experimental system that facilitates the generation of epithelial domes and their subsequent transformation into folds by deflation. Our findings reveal that the timescales of actomyosin cytoskeleton remodeling are critical in this transformation process. Through the manipulation of epithelial geometry and deflation rate, we demonstrate that it is possible to engineer epithelial folds with desired geometry. The results of our study may have important implications for tissue engineering and the development of new techniques for controlling epithelial architecture.

# **Chapter 9**

# **Conclusions and Future Perspectives**

## **9.1 Conclusions**

The main conclusions of this study are as follows:

1. We have developed a microfluidics-based system for generating 3D epithelia using micropatterning technique PRIMO to create a non-adhesive region from which epithelial monolayers can detach and inflate into a dome.
2. Using the MOLI technique, we probed the mechanics of epithelial domes subjected to constant pressure and found that the dome reaches a steady state after five minutes of applying pressure. These experiments revealed a non-monotonic tension-strain response due to geometric constraints.
3. The constitutive response of the epithelial tissue showed that the domes exhibit an initial increase in tension with strain, tending to a tensional plateau at high strains, consistent with earlier studies demonstrating superelastic behavior in epithelia.
4. Dynamic material testing of domes with varying inflation/deflation rates demonstrated that the epithelium behaves as an active viscoelastic material.
5. We developed a complementary model to understand the different timescales involved in the tissue stretching process.

6. Rapid deflation to -50 Pa, faster than the remodeling timescales, leads to buckling instability.
7. Buckling occurs at multiple length scales, from the subcellular level to the tissue level, with differing characteristic lengths of the folds. The shortest folds occur at the membrane cortex level and the longest at the tissue scale.
8. Different sized spherical domes create different patterns. Smaller domes buckle into a fold along their periphery, while larger ones tend to create a network of folds in the center.
9. Folds can be programmed by controlling the shape of the dome. Elliptical domes produce a fold along the major axis, while triangular domes produce a Y-shaped network in the middle.

## 9.2 Future Perspectives

The experiments and theory presented in this thesis focus on the active viscoelasticity of tissues and the generation of folds using buckling instability. However, this experimental setup has implications for several projects within our research group.

For example, the current experiments only examined short timescales (<10-30 minutes) and focused solely on the actin cytoskeleton. Investigating the role of other cytoskeletal components, such as intermediate filaments, would be of great interest. Past studies have shown that intermediate filaments are critical in tissue re-stiffening. My colleague, Tom Golde, is currently using MOLI to study intermediate filament networks.

In addition, we are also utilizing the MOLI device to study a variety of different tissues, including stem-cell tissues, cancer tissue, and organoids. This could enable us to investigate the interplay between geometry, pressure, and cell fate. The inverted cell culture method we use also allows for high-resolution imaging. Two-channel system provides a conducive environment for maintaining complex culture conditions as well as allow for co-culture possibilities.

For the mechanobiology community, our setup is particularly appealing because, when the domes are stretched beyond 100%, the nucleus becomes compressed, which triggers various mechanotransduction pathways. We could easily examine the role of the nucleus and different mechanosensitive proteins when subjected to deformation. Additionally, we could use pharmacological treatments to alter tissue tension and understand the specific molecular pathways involved in maintaining tissue shape.

At the molecular scale, we could also investigate focal adhesions during delamination. Our experimental system delaminates tissue from the substrate, which presents an opportunity to study cell-substrate adhesion using protein patterning and live-cell imaging with focal adhesion markers. Furthermore, experiments conducted over longer timescales could allow us to explore the mechanics of cell-cell junctions and cellular rearrangements in response to prolonged stretching.

I must note the tissue hydraulic aspect, which has been largely overlooked in this thesis. Specifically, we have not extensively explored the trans-epithelial flow due to its negligible effect on our timescale. However, recent studies have demonstrated that the epithelial tissue can function as an active mechano-biological pump, generating its own pressure gradient over longer timescales. Thus, it would be worthwhile to investigate the role of fluid transport under controlled pressure in our microfluidic

system.

Through my work with this system, I have identified numerous promising directions for future research. One particularly intriguing project, led by Thomas Wilson, involves the implementation of concepts such as shape changing, self-healing, and flexible epithelia in the creation of biohybrid devices. Our initial approach will involve the construction of a microfluidic chip, where the channels are composed of epithelial tissues that can be manipulated using optogenetic tools to open or close specific segments, akin to valves. This endeavor will enable us to generate novel synthetic epithelial tissue systems and develop a more comprehensive understanding of the underlying physical principles driving morphogenesis.

# **Part III**

# **Appendices**



# Appendix A

## Methods and Materials

### A.1 Fabrication of microfluidic devices

Polydimethylsiloxane (PDMS) gels (Sylgard PDMS kit, Dow Corning) were used to make the microfluidic devices. PDMS was synthesized by mixing the curing agent and elastomer in 1:9 weight ratio. This mixture was centrifuged for 2min at 900rpm to remove air bubbles. The unpolymerized PDMS was poured into a mold or spun to obtain the desired shape.

There are four parts to the device (figgg). First is the top block, a thick PDMS block with four inlets and one channel for the application of hydraulic pressure. The second is a  $200\mu m$  thin PDMS layer with a  $1.2mm$  diameter hole in the center with a  $400nm$  porous membrane (Polycarbonate filtration membrane  $0.4\mu m$ , Whatman membranes) attached to it. The third is another  $200\mu m$  thin PDMS layer with a channel for seeding the cells. Lastly, all these PDMS parts are attached to, the fourth part, a glass-bottomed 35mm dish ( $35mm$ , no.1.5# coverslip thickness, Cellvis).

The top block was made using replica molding in a 3D printed mold. This mold was 3D printed with vat polymerization and a digital light processing 3D printer (Solus DLP 3D Printer with SolusProto resin). The mold's surface was then silanized using Trichlorosilane (Trichloro(1H,1H,2H,2H-perfluorooctyl) silane, Merck) for preventing adhesion with unpolymerized PDMS. PDMS was poured into the mold and degassed for one hour. PDMS is cured with a hot plate at  $100^\circ C$  for  $30min$ . Once cured, PDMS is removed, cut into devices, and punched with  $1.5mm$ .  $200\mu m$  thin PDMS layers were made by spin coating  $4.5ml$  unpolymerized PDMS on a  $15cm$  dish at  $500rpm$  for  $1min$ . These dishes were incubated in an oven at  $80^\circ C$  to polymerize for  $12hr$ . These

thin sheets were cut into the parts of devices using a Silhouette cutting machine (Silhouette Cameo 4, Silhouette America). The sheets were attached to a Silhouette cutting mat and then Silhouette software was fed with the pattern of the device layers. A sharp cutting tool in the machine cut the PDMS along the pattern. These cut PDMS were peeled off with help of 70% ethanol.

These devices are assembled with the aid of ozone plasma cleaner (PCD-002-CE, Harrick Plasma). Glass bottomed dishes and thin PDMS layers with cell channels were treated for 1min under plasma. Then bonded together by placing the layers in contact for 2hr at 80°C. Similarly, the top block and thin membrane with porous membrane were also bonded. These layers were later bonded together again using plasma cleaner.

## A.2 Patterning protein on the device

The devices were filled with 96% ethanol for removing air bubbles. Then, devices are treated with 5% v/v (3-aminopropyl) triethoxysilane (Merck) diluted in 96% ethanol for 3min and rinse three times with 96% ethanol. Later the devices were filled with MilliQ water to remove ethanol traces. PRIMO (Alveole Lab) was used to pattern adhesion-promoting protein. For this setup, devices were incubated with PLL (Poly-L-lysine solution, Merck) for 1hr, subsequently with SVA PEG (50mg/ml in 8.24pH HEPES) for 30min, and rinsed with HEPES. Before using PRIMO, devices were filled with a photoinitiator. Desired protein pattern was loaded into the PRIMO software (Leonardo, Alveole Lab).

PRIMO uses a microscope to shine the laser in the specific region according to the loaded pattern to cut PEG chains. After the PRIMO process, the samples were rinsed with phosphate-buffered saline (PBS, Merck). Then the samples were filled with fibronectin and fibrinogen (100 $\mu$ g/ml Fibronectin in 2% Far-red fibrinogen solution in 1X PBS) solution for 5min. Then samples were rinsed again with 1X PBS. Fibrinogen labels the fibronectin with Far-red signal to image the coated protein pattern and allows for tracking the position of the domes. The PRIMOed samples can be stored at 4°C for two to three days before seeding cells.

### A.3 Cell culture in the device

To image cell shape and tissue structure Madin-Darby Canine Kidney (MDCK) cells expressing CIBN-GFP-CAAX were used for the experiments. CIBN-GFP-CAAX labels the plasma membrane. These cells were cultured in Dulbecco's Modified Eagle Medium (DMEM, Gibco ThermoFisher) with 10% v/v fetal bovine serum (FBS, Gibco, ThermoFisher), L-glutamine (ThermoFisher), 100 $\mu$ g/ml streptomycin and penicillin. Cells were incubated at 37°C with a 5% CO<sub>2</sub> condition.

Before seeding cells in the device, it is filled with a cell culture medium. Cells are trypsinized and diluted at a concentration of 25 – 30 × 10<sup>6</sup> cells/ml. The cell channel of the device is filled with 30 $\mu$ l of cell solution and incubated for cell adhesion. After one hour of incubation, devices are rinsed with media to remove unattached cells. Devices were kept 24hr in the incubation for the growth of a monolayer before the experiment. It is important to note that the inverted epifluorescence microscope is needed to see the cells. The bright-field microscope can not be used for visualizing cells because of the porous membrane.

### A.4 Staining actin with SPY-actin

To observe the dynamics of the cortex, we used SPY555-actin (Spirochrome), a bright dye optimized for quick labeling of F-actin in live cells with low background. To prepare the 1000x solution, we added 50 $\mu$ l of anhydrous DMSO to the stock SPY555-actin. We then added 1 $\mu$ l of the 1000x solution to 999 $\mu$ l of cell culture medium. The resulting solution was introduced into the microfluidic chips and left in the incubator for 2 hours before imaging.

### A.5 Fabrication method for the Light-Sheet MOLI device

The devices used with the light-sheet microscope consisted of a single PDMS block bonded to a glass microscope slide (76 × 26mm, RS Components BPB016). The blocks were made using a 3D printed mold (Ultimaker 3 with Ultimaker PLA Printer Filament 1616). PDMS was mixed, centrifuged, degassed, and cured as described above for the normal devices. Once cured, the PDMS was removed, cut into individual devices and punched with a 1.5mm biopsy punch. The PDMS blocks were then attached glass slides using a thin layer of unpolymerized PDMS, that was coated onto the glass slides

using a spatula. The devices were then kept on a hotplate at 100°C for 30min to allow the PDMS bonding to fully cure. The 400nm porous membranes were then attached to the devices. The edges of the membrane were carefully dipped into unpolymerized PDMS, before being placed flat on the top of the device. Particular care was taken to ensure the center of the membrane over the punched pressure-application hole remained free of PDMS. The devices were then kept at 65°C for an hour to allow the PDMS bonding to fully cure.

## A.6 Device protein patterning and cell culture in Light-Sheet device

The light-sheet devices were protein patterned and cell cultured using the same methods and steps as outlined above for the normal devices, with the one minor addition of the use of a simple PDMS and glass cap for a few critical steps. The porous membrane for pressure application, and thus the site of protein patterning and cell seeding, for the light-sheet devices is exposed and on the top side of the devices. This mostly allowed for easy application of reagents as a droplet could be applied and aspirated directly.

However for the more sensitive steps in the procedure, a simple PDMS and glass device was used to create a temporary covered channel over the porous membrane to regulate the procedure and ensure the treatment of the devices was highly standardized. Specifically, the cap was used for the application of photoinitiator during PRIMO, and for the application of cell solution during cell attachment. The caps were fabricated using  $2\text{cm} \times 2\text{cm}$  squares of a  $400\mu\text{m}$  thick PDMS layer, with a keyhole shape cut in from the side. Each PDMS piece was then stuck to a 18mm diameter coverslip (18mm, 1# Cover glasses circular, Marienfeld 0111580) using the surface tension of the liquid. The experimental apparatus and measurements for the light-sheet devices were the same as the normal devices as outlined above.

## A.7 Application and measurement of the pressure

The pressure is applied via hydrostatic forces similar to the previous studies (Choudhury *et al.*, 2022b, Palmer *et al.*, 2021). The two channels in the chip were separated by the porous membrane. Cells are on the bottom side of the membrane. The pressure in the channel (top side of the membrane) is used to inflate the structures on the

top. This channel has one inlet and one outlet for removing bubbles. The inlet is connected to a  $35\text{ml}$  reservoir of cell culture medium (in a  $50\text{ml}$  falcon tube) by tubing (PTFE Tubing 1/16inch OD for Microfluidics, Darwin microfluidics) and the outlet is connected to a shutoff valve (Microfluidic Sample Injection / Shut-off Valve, Darwin microfluidics). Once bubbles are removed, closing the valve would apply the pressure on the basal side of the cells according to the difference between the height of the fluid level. All tubings are connected to the chip with a steel insert (Stainless steel 90deg Bent PDMS Couplers, Darwin microfluidics). We are able to find zero by matching the height of the device to the liquid and air interface in the reservoir. This is confirmed with the experiments, where on applying pressure domes form but on slow reduction in pressure to zero causes domes to deflate.

## A.8 Confocal Microscopy

For timelapse imaging of domes at a larger time interval ( $> 1$  min), an inverted Nikon microscope with a spinning disk confocal unit (CSU-W1, Yokogawa) was used with Nikon 40x, 20x, and 10x air lenses. For shorter time intervals ( $< 10$  s), a Zeiss LSM880 inverted confocal microscope was used with laser scanning mode. Fast imaging was enabled by imaging a single line in the middle of the dome.

## A.9 Light-sheet microscopy

The imaging of the light-sheet devices was done with a dual-illumination inverted Selective Plane Illumination Microscope (diSPIM) (QuVi SPIM, Luxendo, Brucker) with Nikon 40x immersion lenses (Nikon CFI Apo 40x W 0.8 NA NIR water immersion objective). For the buckling experiments, only single objective illumination and detection was used for the fast imaging of  $2\text{s}/frame$ .

## A.10 Quantification of the dome areal strain and tension

As mentioned earlier, the domes were imaged in 3D with confocal microscopy. We used ImageJ to manually section the dome in the middle in the YZ plane, XZ plane is a plane parallel to the monolayer, with Reslice function along the Z axis. This section was used to calculate the height ( $h$ ), radius of curvature ( $R$ ), and base radius ( $a$ ). Strain

( $\epsilon$ ) and tension ( $\sigma$ ) were calculated as,

$$\epsilon = \frac{h^2}{a^2}, \quad \text{and} \quad \sigma = \frac{\Delta PR}{2}.$$

The raw data was extracted in ImageJ and then MATLAB was used to compute and plot the strain and tension.

## A.11 Analysis of the kymographs

For cyclic pressure or buckling experiments, the domes were imaged at low resolution and high noise levels to capture fast dynamics. The previous method of manually quantifying each time point is not feasible. Thus, we used the ImageJ function of the Reslice function along the time axis. We resliced it along the Y-time axis in the middle of the dome, such that we get a kymograph of height as a function of time. Also, we performed the reslicing along the XT axis at the plane of the monolayer, such that we get the kymograph of the base radius with respect to time. These kymographs were in form of images save manually with ImageJ.

A custom-built MATLAB code was used to digitize the kymographs, where maximum intensity along each time was considered as the current dome height position. The first 30s of the experiment pressure is zero, so the unstretched monolayer position is determined from those time points. Dome height is calculated with the difference between the current position and the initial position. Base radius is calculated similarly by subtracting two sides. The radius of curvature is calculated using the relation between the base and height of the dome as

$$R = (h^2 + a^2)/2h.$$

## A.12 Qualitative analysis of the buckling event

Whether domes are buckling or not was determined manually checking every frame during the deflation. If dome maintains the smooth circular geometry in XZ plane during the deflation, we mark the dome as “not buckling”. However, if the dome has a visual discontinuity in the curvature or a kink it is then considered to be “buckling”.

Imaging the fast events in XY plane was done in an ad hoc manner. To capture the folds, the dome as imaged closer to the apical surface of the monolayer. The type of fold was determined by carefully observing the way which monolayer makes contact

with the imaging plane. If there is one point of contact in the center and spreads outwards, it is considered as accumulation along the periphery. In case where there are multiple points of contact and they all join in the middle, it is considered as a network of folds.



# **Appendix B**

## **MOLI Protocol**

### **B.1 Device Fabrication**

#### **B.1.1 Main Block Fabrication**

1. Place the empty 3D printed mold on hot plate at 100°C for 1 hour.
2. Mix around 20 ml of PDMS (Sylgard kit) at a 1:9 ratio.
3. Pour PDMS into a 50ml centrifuge tube, and weight out another of equal mass of water.
4. Centrifuge for 3 mins at 900rpm.
5. Fill the mold with 12ml of PDMS.
6. Place the mold with PDMS into a desiccator for 1 hour or until there are no bubbles remaining.
7. Then place the mold on a hot plate at 100°C for 30 mins, until it is polymerised and solid to touch with tweezers.
8. Carefully cut the PDMS block out from the mold and place it into a dish with the pattern side up.
9. Repeat Steps 5 to 8 to create more blocks and then with any remaining PDMS, fill the mold with a small amount and set it on the hot plate 100°C, so as to keep the mold clean.
10. Punch four holes in the devices with the 1.5mm biopsy punch.
11. Cut out the individual devices with the scalpel.

12. Store devices with the pattern facing up in a dish.

### B.1.2 Membrane Fabrication

1. Meanwhile, prepare around 10ml of PDMS at a ratio of 2:8. Centrifuge as in Steps 3 and 4 in the previous section.
2. Using a syringe, measure 4ml of PDMS into a large petri dish.
3. Use the nitrogen gun to remove bubbles and evenly spread the PDMS across the dish, whilst not letting it touch the sides.
4. Leave the dish on a level surface at room temperature for at least 2 hours to allow the PDMS to coat evenly.
5. Place in the oven at 80°C for an hour (or 60°C for 2 hours).
6. Follow section 1.2 to cut the membranes.

#### B.1.2.1 Silhouette Cutting Method

7. Cut the biggest rectangle possible in the PDMS membrane with scalpel.
8. Use a bit of 90% ethanol to peel off the membrane from the dish.
9. Place the membrane on the silhouette cutting mat. Make sure to have membrane completely dry before placing it.
10. Press the membrane against the mat to get rid of all the bubbles and making adhesion with the mat more secure.
11. Load the cutting mat in the Silhouette machine.
12. Open cutting pattern in the silhouette software.
13. Select the cut settings:
  - *Material = Vinyl*
  - *Depth = 10*
  - *Speed = 5*
14. Make sure the PDMS is at a correct location corresponding to the drawings.
15. Press ‘Send to silhouette machine’.
16. During the cutting process, be aware of pieces of PDMS delaminating and getting stuck in the machine.
17. After the successful cutting, unload the cutting mat.

18. Remove all the small PDMS and holes before then peeling off the actual layers and storing them in a dish.

## B.2 Plasma Bonding

### B.2.1 First Bonding

1. Items needed in the clean room:
  - PDMS blocks and membranes
  - Glass bottom dishes
  - Scalpel
  - Tweezers
  - Cutting mat
2. Have a hot plate next to the plasma cleaner at 100°C with cloth on top.
3. Plasma clean a large dish with the top blocks and the middle layers. Use the high setting for 30 seconds.
4. Combine the block and membrane (so as to create an enclosed channel with a central hole). Make sure to line up holes and apply a lot of pressure to the PDMS.
5. Flip over the blocks (membrane side up) in the dish, and place on the hot plate.
6. Place the bottom channel layers into the lids of the glass bottom dishes, with two membranes per lid.
7. Plasma clean the layers and glass bottom dishes the same as Step 4.
8. Holding each dish at arms length, spray it with ethanol so that it gets very lightly coated, and then attach a membrane to the centre of the dish. Apply some pressure and ensure that there are no bubbles but do not apply too much force as the glass bottoms of the dishes are fragile.
9. Put the lids onto the dishes and place them onto the hot plate.
10. Once plasma area is cleaned, place the samples into the oven at 80°C. Leave for a minimum of 2 hours.

### B.2.2 Second Bonding

1. Cut any protruding parts of the membrane from the bonded PDMS blocks, and then cut the corners off to create an octagonal shape.
2. Cut 400nm porous membrane disks into small pieces of around 4mm × 4mm (9 pieces per sheet). Store these between layers of a cloth in a large petri dish.
3. Mix around 20ml of PDMS and put small amount (<2ml) into a petri dish.
4. On the underside of the glass bottom dishes, mark the edges of the bonded channel with a pen.
5. Return to clean room with devices, membranes and unpolymerised PDMS.
6. Have a hot plate at 100°C.
7. Hold a piece of paper with tweezers, slightly dip one edge of the paper into the wet PDMS and remove excess by placing it on a cloth.
8. Gently, paint the wet PDMS onto the middle layer around the hole with paper. Be cautious of using too much PDMS might result in blockage on the hole.
9. Place the porous membranes over the central hole of the PDMS block and press down the edges gently.
10. Similar to the first bonding, place the blocks into the glass bottom dish lids with two per lid.
11. Plasma clean the blocks and glass bottom dishes, following the same specifications as Step 4 in Section 2.1.
12. Bond the blocks and dishes by placing the blocks porous membrane side up on your finger and align the channel using the pen marks as a guide. Ensure that the holes are lined up and the two enclosed channels are perpendicular. Press the PDMS block on the cloth to ensure attachment.
13. Put lids onto the dishes and place them onto the hot plate.
14. Once plasma area is cleaned, return with the samples and place them into the oven at 80°C.
15. After 30 mins, use a 20ml syringe to pour PDMS around the base of the devices for a better seal, covering the remainder of the glass base.
16. Return the devices to the oven and leave for a minimum of 2 hours.

## B.3 PRIMO

### B.3.1 PRIMO Preparation

1. Wash the devices with ethanol. Pipette 80 $\mu$ L of 70% ethanol thought each channel, ensuring that it only emerges from the opposite hole, and that there are no bubbles in the channels. Aspirate off the excess.
2. Repeat this with MilliQ water or PBS.
3. Pour a few drops of MilliQ water around the edge of the device to reduce evaporation.
4. Fill each channels with 80 $\mu$ L of PLL.
5. Leave at room temperature for 1 hour.
6. After 50 mins, create SVAPEG solution (will require 80 $\mu$ L per device so scale accordingly):
  - Accurately measure around 20mg of SVAPEG powder.
  - Add 20 $\times$  the amount of HEPES buffer solution to the powder (400 $\mu$ L for 20mg of powder).
  - Mix well, ensuring all powder is included. Do this immediately before using.
  - Using a desiccator, store the SVAPEG powder under argon, sealed with para-film and in a vacuum bag.
7. Pipette 40 $\mu$ L of HEPES buffer solution into each channel and aspirate the excess.
8. Soon after mixing the SVAPEG solution, fill each channel with 40 $\mu$ L of it.
9. Leave for 30 mins at room temperature or overnight at 4°C, with enough MilliQ water around them to prevent them becoming dry.

### B.3.2 PRIMO Protocol

1. Prepare the fibronectin solution (will require 40 $\mu$ L per device):
  - Combine 20 $\mu$ L of fibrinogen [FGN] with 980 $\mu$ L of of PBS.
  - Filter the solution with 0.22  $\mu$ m filter.
  - Take 600  $\mu$ L of the mixture and add 60  $\mu$ L of fibronectin [FN]. Discard leftovers.

- Store in the ice.
2. Add 40 µL of photo-inhibitor to the lower channel of the devices. Do this in batches of three or four.
  3. Preform PRIMO:
    - Use the PRIMO enabled microscope.
    - Focus on porous membrane, which will be when it appears darkest.
    - Find boundary of the 1.2mm hole and match 1200µm circle.
    - Select ‘Scan’ and then ‘Lock’.
    - Select ‘µPattern’ and load template.
    - Select *Lines = 4* and *Dose = 500*.
    - Set Spacing to the negative of the ‘Find Size Height’ ( $-1223\mu\text{m}$ ), but adjust to get the best pattern match.
    - Turn off both ‘Eye’ Icons on the left side.
    - Select ‘Forward’ in lower-right corner of screen and wait for the process to complete, which should be around 17 mins.
  4. After PRIMO is complete, pipette 80µL of PBS into each channel and aspirate excess.
  5. Then pipette 40µL of FN solution (from Step 1) into the lower channel. Do this in batches of three or four.
  6. After exactly 5 mins (important to be accurate), wash all channels with PBS twice.
  7. Place a few drops of MiliQ water around the devices and store in fridge at 4°C.  
Note that cells must be seeded with 2 days of PRIMO completion.

## B.4 Cell Seeding

1. Warm media and trypsin in the cell culture bath.
2. Treat all devices with UV for 15 mins using the fume hood (‘Disinfect’ → ‘UV’). Ensure all lids are opened.
3. Detach cells from the flask using 3ml trypsin, as normally done in cell passing.
4. While cells are in the oven detaching, get two 15ml vials and fill one with media.

5. Aspirate the top of the devices and fill all channels with media (from vial). Aspirate the excess.
6. After removing cells from the oven, mix with 7ml of media.
7. Using a Neubauer Chamber, count the number of cells in the sample.
8. Meanwhile, fill the other 15ml vial with the rest of the cell culture and centrifuge for 3.5 mins at 1000rpm.
9. Aspirate away the media from the vial, leaving only the cells at the bottom.
10. Add new media, such that the sample is diluted to 25-30 million cells per ml.
11. Pipette 35mL of culture into the lower channel of each device. Always mix the cells in the vial with reverse pipetting between samples and quickly aspirate off the excess. Put a few drop of media on top and around each device.
12. Flip tray over and place in the incubator.
13. After 1 hour, flip the devices back round and aspirate any media off the device tops.
14. Quickly pipette 200 $\mu$ L of media into the device lower channels to remove unattached cells, while aspirating off the excess media.
15. Put a few drops of fresh media on top of the devices to slow evaporation.
16. Using a microscope, check the devices. Use the CY5 channel to check for a pattern, and the GFP channel for a uniform layer of cells.
17. Rinse devices again with media and place a large droplet on top of the devices such that when the lids are replaced, a ‘column’ of media is formed.
18. Place in the incubator again (the correct way up) and leave overnight.

## B.5 Experiment

1. Warm up two reservoirs of CO<sub>2</sub> media (one of around 35ml and one of around 10ml) for around 30 mins.
2. Then place the reservoirs in a desiccator for 30 mins (with lids unscrewed).
3. Clean tubing with PBS.
4. Connect the translation to both power and the computer. Place the 35ml of media in the stage holder.

5. Connect vacuum and open to 200psi. Tape tubes into place around the microscope.
6. Open stage control software *ZABER*, and move stage to where the level of the media is the same as that of the devices.
7. Move condenser as high as possible and connect pressure stage tubing to one of the upper-channel device outlets. Use the vacuum to ensure the full tube is filled with media before connecting, as it is important that there are no bubbles in the tubing or device.
8. Connect the vacuum T-device to the other upper-channel device outlet.
9. Slowly lift the media reservoir out of the stage until domes start to appear in patterned areas. Return reservoir to stage.
10. Using stage software, re-form domes and identify the best one(s) for imaging.
11. Perform the experiment of choice.
12. After experiment, disconnect everything and clean tubing with ethanol and PBS.

# Bibliography

- Are All Fish the Same Shape If You Stretch Them? The Victorian Tale of On Growth and Form. <https://writings.stephenwolfram.com/2017/10/are-all-fish-the-same-shape-if-you-stretch-them-the-victorian-tale-of-on-growth-and-form/>.
- Animal Tissues. Covering Epithelium. Atlas of Plant and Animal Histology. [https://mmegias.webs.uvigo.es/02-english/guiada\\_a\\_revestimiento.php](https://mmegias.webs.uvigo.es/02-english/guiada_a_revestimiento.php).
- The 100-Year-Old Challenge to Darwin That Is Still Making Waves in Research. *Nature* **544**, 138 (2017a).
- A Ton for Thompson's Tome. *Nature Physics* **13**, 315 (2017b).
- Adriaen Backer Wikipedia. Dutch: Anatomische Les van Dr. Frederik Ruysch Anatomy Lesson by Prof. Frederik Ruysch.Label QS:Lnl,"Anatomische Les van Prof. Frederik Ruysch.". (1670).
- B. Alberts. *Molecular Biology of the Cell*. sixth edition ed. (Garland Science, Taylor and Francis Group, New York, NY, 2015).
- S. Alt, P. Ganguly, and G. Salbreux. Vertex Models: From Cell Mechanics to Tissue Morphogenesis. *Philosophical Transactions of the Royal Society B: Biological Sciences* **372**, 20150520 (2017).
- D. Ambrosi, M. Ben Amar, C. J. Cyron, A. DeSimone, A. Goriely, J. D. Humphrey, and E. Kuhl. Growth and Remodelling of Living Tissues: Perspectives, Challenges and Opportunities. *Journal of The Royal Society Interface* **16**, 20190233 (2019).
- Z. U. Arif, M. Y. Khalid, W. Ahmed, and H. Arshad. A Review on Four-Dimensional (4D) Bioprinting in Pursuit of Advanced Tissue Engineering Applications. *Bio-printing* **27**, e00203 (2022).

- L. Balasubramaniam, A. Doostmohammadi, T. B. Saw, G. H. N. S. Narayana, R. Mueller, T. Dang, M. Thomas, S. Gupta, S. Sonam, A. S. Yap, Y. Toyama, R.-M. Mège, J. M. Yeomans, and B. Ladoux. Investigating the Nature of Active Forces in Tissues Reveals How Contractile Cells Can Form Extensile Monolayers. *Nature Materials* **20**, 1156 (2021).
- G. Bao and S. Suresh. Cell and Molecular Mechanics of Biological Materials. *Nature Materials* **2**, 715 (2003).
- D. Bartolo, G. Degré, P. Nghe, and V. Studer. Microfluidic Stickers. *Lab on a Chip* **8**, 274 (2008).
- C. Blanch-Mercader, V. Yashunsky, S. Garcia, G. Duclos, L. Giomi, and P. Silberzan. Turbulent Dynamics of Epithelial Cell Cultures. *Physical Review Letters* **120**, 208101 (2018).
- S. Blonski, J. Aureille, S. Badawi, D. Zaremba, L. Pernet, A. Grichine, S. Fraboulet, P. M. Korczyk, P. Recho, C. Guilluy, and M. E. Dolega. Direction of Epithelial Folding Defines Impact of Mechanical Forces on Epithelial State. *Developmental Cell* **56**, 3222 (2021).
- A. Bonfanti, J. Fouchard, N. Khalilgharibi, G. Charras, and A. Kabla. A unified rheological model for cells and cellularised materials. *Royal Society Open Science* **7**, 190920 (2020). <https://royalsocietypublishing.org/doi/pdf/10.1098/rsos.190920>.
- J. R. Bourke, T. Matainaho, G. J. Huxham, and S. W. Manley. Cyclic AMP-stimulated Fluid Transport in the Thyroid: Influence of Thyroid Stimulators, Amiloride and Acetazolamide on the Dynamics of Domes in Monolayer Cultures of Porcine Thyroid Cells. *Journal of Endocrinology* **115**, 19 (1987).
- V. Braga. Spatial Integration of E-cadherin Adhesion, Signalling and the Epithelial Cytoskeleton. *Current Opinion in Cell Biology Cell Dynamics*. **42**, 138 (2016).
- J. A. Brassard, M. Nikolaev, T. Hübscher, M. Hofer, and M. P. Lutolf. Recapitulating Macro-Scale Tissue Self-Organization through Organoid Bioprinting. *Nature Materials* **20**, 22 (2021).
- K. A. Breau, M. T. Ok, I. Gomez-Martinez, J. Burclaff, N. P. Kohn, and S. T. Magness. Efficient Transgenesis and Homology-Directed Gene Targeting in Monolayers

- of Primary Human Small Intestinal and Colonic Epithelial Stem Cells. *Stem Cell Reports* **17**, 1493 (2022).
- T. M. Brown and E. Fee. Rudolf Carl Virchow. *American Journal of Public Health* **96**, 2104 (2006).
- A. Brugués, E. Anon, V. Conte, J. H. Veldhuis, M. Gupta, J. Colombelli, J. J. Muñoz, G. W. Brodland, B. Ladoux, and X. Trepaut. Forces Driving Epithelial Wound Healing. *Nature Physics* **10**, 683 (2014).
- D. M. Bryant and K. E. Mostov. From Cells to Organs: Building Polarized Tissue. *Nature Reviews Molecular Cell Biology* **9**, 887 (2008).
- A. Callan-Jones and R. Voituriez. Active gel model of amoeboid cell motility. *New Journal of Physics* **15**, 025022 (2013).
- S. Calzolari, J. Terriente, and C. Pujades. Cell Segregation in the Vertebrate Hindbrain Relies on Actomyosin Cables Located at the Interhombomeric Boundaries. *The EMBO Journal* **33**, 686 (2014).
- G. Cameron. Secretory Activity of the Choroid Plexus in Tissue Culture. *The Anatomical Record* **117**, 115 (1953).
- O. Campàs, T. Mammoto, S. Hasso, R. A. Sperling, D. O'Connell, A. G. Bischof, R. Maas, D. A. Weitz, L. Mahadevan, and D. E. Ingber. Quantifying Cell-Generated Mechanical Forces within Living Embryonic Tissues. *Nature Methods* **11**, 183 (2014).
- A. X. Cartagena-Rivera, J. S. Logue, C. M. Waterman, and R. S. Chadwick. Actomyosin Cortical Mechanical Properties in Nonadherent Cells Determined by Atomic Force Microscopy. *Biophysical Journal* **110**, 2528 (2016).
- L. Casares, R. Vincent, D. Zalvidea, N. Campillo, D. Navajas, M. Arroyo, and X. Trepaut. Hydraulic Fracture during Epithelial Stretching. *Nature Materials* **14**, 343 (2015).
- K. E. Cavanaugh, M. F. Staddon, S. Banerjee, and M. L. Gardel. Adaptive Viscoelasticity of Epithelial Cell Junctions: From Models to Methods. *Current Opinion in Genetics & Development* **63**, 86 (2020).

- G. Y. Cederquist, J. J. Asciolla, J. Tchieu, R. M. Walsh, D. Cornacchia, M. D. Resh, and L. Studer. Specification of Positional Identity in Forebrain Organoids. *Nature Biotechnology* **37**, 436 (2019).
- M. Cetera, G. R. Ramirez-San Juan, P. W. Oakes, L. Lewellyn, M. J. Fairchild, G. Tanentzapf, M. L. Gardel, and S. Horne-Badovinac. Epithelial Rotation Promotes the Global Alignment of Contractile Actin Bundles during Drosophila Egg Chamber Elongation. *Nature Communications* **5**, 5511 (2014).
- C. J. Chan and T. Huiragi. Integration of Luminal Pressure and Signalling in Tissue Self-Organization. *Development* **147**, dev181297 (2020).
- C. J. Chan, M. Costanzo, T. Ruiz-Herrero, G. Mönke, R. J. Petrie, M. Bergert, A. Díz-Muñoz, L. Mahadevan, and T. Huiragi. Hydraulic Control of Mammalian Embryo Size and Cell Fate. *Nature* **571**, 112 (2019).
- H. F. Chan, R. Zhao, G. A. Parada, H. Meng, K. W. Leong, L. G. Griffith, and X. Zhao. Folding Artificial Mucosa with Cell-Laden Hydrogels Guided by Mechanics Models. *Proceedings of the National Academy of Sciences* **115**, 7503 (2018).
- M. I. Choudhury, M. A. Benson, and S. X. Sun. Trans-Epithelial Fluid Flow and Mechanics of Epithelial Morphogenesis. *Seminars in Cell & Developmental Biology* Special Issue: Human Embryogenesis by Naomi Moris and Marta Shahbazi / Special Issue: Luminogenesis and Hydraulics in Development by Chii Jou Chan. **131**, 146 (2022a).
- M. I. Choudhury, Y. Li, P. Mistriotis, A. C. N. Vasconcelos, E. E. Dixon, J. Yang, M. Benson, D. Maity, R. Walker, L. Martin, F. Koroma, F. Qian, K. Konstantopoulos, O. M. Woodward, and S. X. Sun. Kidney Epithelial Cells Are Active Mechano-Biological Fluid Pumps. *Nature Communications* **13**, 2317 (2022b).
- D. N. Clarke and A. C. Martin. Actin-Based Force Generation and Cell Adhesion in Tissue Morphogenesis. *Current Biology* **31**, R667 (2021).
- R. Clément, B. Dehapiot, C. Collinet, T. Lecuit, and P.-F. Lenne. Viscoelastic Dissipation Stabilizes Cell Shape Changes during Tissue Morphogenesis. *Current Biology* **27**, 3132 (2017).
- C. Collinet and T. Lecuit. Programmed and Self-Organized Flow of Information during Morphogenesis. *Nature Reviews Molecular Cell Biology* **22**, 245 (2021).

- C. Collinet, M. Rauzi, P.-F. Lenne, and T. Lecuit. Local and Tissue-Scale Forces Drive Oriented Junction Growth during Tissue Extension. *Nature Cell Biology* **17**, 1247 (2015).
- A. Cont, T. Rossy, Z. Al-Mayyah, and A. Persat. Biofilms Deform Soft Surfaces and Disrupt Epithelia. *eLife* **9**, e56533 (2020).
- D. B. Cortes, M. Gordon, F. Nédélec, and A. S. Maddox. Bond Type and Discretization of Nonmuscle Myosin II Are Critical for Simulated Contractile Dynamics. *Biophysical Journal* **118**, 2703 (2020).
- K. D. Costa, W. J. Hucker, and F. C.-P. Yin. Buckling of Actin Stress Fibers: A New Wrinkle in the Cytoskeletal Tapestry. *Cell Motility* **52**, 266 (2002).
- M. Deforet, V. Hakim, H. G. Yevick, G. Duclos, and P. Silberzan. Emergence of Collective Modes and Tri-Dimensional Structures from Epithelial Confinement. *Nature Communications* **5**, 3747 (2014).
- C. J. Demers, P. Soundararajan, P. Chennampally, G. A. Cox, J. Briscoe, S. D. Collins, and R. L. Smith. Development-on-Chip: In Vitro Neural Tube Patterning with a Microfluidic Device. *Development* **143**, 1884 (2016).
- L. Deng, X. Trepaut, J. P. Butler, E. Millet, K. G. Morgan, D. A. Weitz, and J. J. Fredberg. Fast and Slow Dynamics of the Cytoskeleton. *Nature Materials* **5**, 636 (2006).
- J. Dervaux and M. B. Amar. Mechanical Instabilities of Gels. *Annual Review of Condensed Matter Physics* **3**, 311 (2012).
- C. A. Dessalles, C. Ramón-Lozano, A. Babataheri, and A. I. Barakat. Luminal Flow Actuation Generates Coupled Shear and Strain in a Microvessel-on-Chip. *Biofabrication* **14**, 015003 (2021).
- M. E. Dolega, M. Delarue, F. Ingremeau, J. Prost, A. Delon, and G. Cappello. Cell-like Pressure Sensors Reveal Increase of Mechanical Stress towards the Core of Multicellular Spheroids under Compression. *Nature Communications* **8**, 14056 (2017).
- A. Ducuing and S. Vincent. The Actin Cable Is Dispensable in Directing Dorsal Closure Dynamics but Neutralizes Mechanical Stress to Prevent Scarring in the Drosophila Embryo. *Nature Cell Biology* **18**, 1149 (2016).

- O. Dudin, A. Ondracka, X. Grau-Bové, A. A. Haraldsen, A. Toyoda, H. Suga, J. Bråte, and I. Ruiz-Trillo. A Unicellular Relative of Animals Generates a Layer of Polarized Cells by Actomyosin-Dependent Cellularization. *eLife* **8**, e49801 (2019).
- R. Dulbecco and S. Okada. Differentiation and Morphogenesis of Mammary Cells in Vitro. *Proceedings of the Royal Society of London. Series B. Biological Sciences* **208**, 399 (1980).
- J. G. Dumortier, M. L. Verge-Serandour, A. F. Tortorelli, A. Mielke, L. de Plater, H. Turlier, and J.-L. Maître. Hydraulic Fracturing and Active Coarsening Position the Lumen of the Mouse Blastocyst. *Science* (2019). 10.1126/science.aaw7709.
- J. Duque, A. Bonfanti, J. Fouchard, E. Ferber, A. Harris, A. J. Kabla, and G. T. Charras. Fracture in Living Cell Monolayers. (2023).
- A. Elosegui-Artola, I. Andreu, A. E. M. Beedle, A. Lezamiz, M. Uroz, A. J. Kosmalska, R. Oria, J. Z. Kechagia, P. Rico-Lastres, A.-L. Le Roux, C. M. Shanahan, X. Trepat, D. Navajas, S. Garcia-Manyes, and P. Roca-Cusachs. Force Triggers YAP Nuclear Entry by Regulating Transport across Nuclear Pores. *Cell* **171**, 1397 (2017).
- A. Elosegui-Artola, A. Gupta, A. J. Najibi, B. R. Seo, R. Garry, C. M. Tringides, I. de Lázaro, M. Darnell, W. Gu, Q. Zhou, D. A. Weitz, L. Mahadevan, and D. J. Mooney. Matrix Viscoelasticity Controls Spatiotemporal Tissue Organization. *Nature Materials* , 1 (2022).
- A. Elosegui-Artola, R. Oria, Y. Chen, A. Kosmalska, C. Pérez-González, N. Castro, C. Zhu, X. Trepat, and P. Roca-Cusachs. Mechanical Regulation of a Molecular Clutch Defines Force Transmission and Transduction in Response to Matrix Rigidity. *Nature Cell Biology* **18**, 540 (2016).
- A. J. Engler, S. Sen, H. L. Sweeney, and D. E. Discher. Matrix Elasticity Directs Stem Cell Lineage Specification. *Cell* **126**, 677 (2006).
- P. Fernandez, L. Heymann, A. Ott, N. Aksel, and P. A. Pullarkat. Shear rheology of a cell monolayer. *New Journal of Physics* **9**, 419 (2007).
- P. A. Fernández, B. Buchmann, A. Goychuk, L. K. Engelbrecht, M. K. Raich, C. H. Scheel, E. Frey, and A. R. Bausch. Surface-Tension-Induced Budding Drives Alveologenesis in Human Mammary Gland Organoids. *Nature Physics* **17**, 1130 (2021).

- J. Fierling, A. John, B. Delorme, A. Torzynski, G. B. Blanchard, C. M. Lye, A. Popkova, G. Malandain, B. Sanson, J. Étienne, P. Marmottant, C. Quilliet, and M. Rauzi. Embryo-Scale Epithelial Buckling Forms a Propagating Furrow That Initiates Gastrulation. *Nature Communications* **13**, 3348 (2022).
- J. Firmin, N. Ecker, D. R. Danon, V. B. Lange, H. Turlier, C. Patrat, and J.-L. Maître. Mechanics of Human Embryo Compaction. (2022).
- E. Fischer-Friedrich, Y. Toyoda, C. J. Cattin, D. J. Müller, A. A. Hyman, and F. Jülicher. Rheology of the Active Cell Cortex in Mitosis. *Biophysical Journal* **111**, 589 (2016).
- D. A. Fletcher and R. D. Mullins. Cell Mechanics and the Cytoskeleton. *Nature* **463**, 485 (2010).
- I. C. Fortunato and R. Sunyer. The Forces behind Directed Cell Migration. *Biophysica* **2**, 548 (2022).
- J. Fouchard, T. P. J. Wyatt, A. Proag, A. Lisica, N. Khalilgharibi, P. Recho, M. Suzanne, A. Kabla, and G. Charras. Curling of Epithelial Monolayers Reveals Coupling between Active Bending and Tissue Tension. *Proceedings of the National Academy of Sciences* **117**, 9377 (2020).
- F. Gallaire and P.-T. Brun. Fluid Dynamic Instabilities: Theory and Application to Pattern Forming in Complex Media. *Philosophical Transactions of the Royal Society A: Mathematical, Physical and Engineering Sciences* **375**, 20160155 (2017).
- N. Gjorevski, M. Nikolaev, T. E. Brown, O. Mitrofanova, N. Brandenberg, F. W. DelRio, F. M. Yavitt, P. Liberali, K. S. Anseth, and M. P. Lutolf. Tissue Geometry Drives Deterministic Organoid Patterning. *Science* (2022). 10.1126/science.aaw9021.
- N. Gjorevski, N. Sachs, A. Manfrin, S. Giger, M. E. Bragina, P. Ordóñez-Morán, H. Clevers, and M. P. Lutolf. Designer Matrices for Intestinal Stem Cell and Organoid Culture. *Nature* **539**, 560 (2016).
- B. G. Godard and C.-P. Heisenberg. Cell Division and Tissue Mechanics. *Current Opinion in Cell Biology Cell Dynamics*. **60**, 114 (2019).
- P. Gómez-Gálvez, P. Vicente-Munuera, S. Anbari, J. Buceta, and L. M. Escudero. The Complex Three-Dimensional Organization of Epithelial Tissues. *Development* **148**, dev195669 (2021).

- M. Gómez-González, E. Latorre, M. Arroyo, and X. Trepat. Measuring Mechanical Stress in Living Tissues. *Nature Reviews Physics* **2**, 300 (2020).
- M. Good and X. Trepat. Cell Parts to Complex Processes, from the Bottom Up. *Nature* **563**, 188 (2018).
- N. Gorfinkel and A. Martinez Arias. The Cell in the Age of the Genomic Revolution: Cell Regulatory Networks. *Cells & Development Quantitative Cell and Developmental Biology*. **168**, 203720 (2021).
- F. Graner and D. Riveline. ‘The Forms of Tissues, or Cell-aggregates’: D’Arcy Thompson’s Influence and Its Limits. *Development* **144**, 4226 (2017).
- P. Guillamat, C. Blanch-Mercader, G. Pernollet, K. Kruse, and A. Roux. Integer Topological Defects Organize Stresses Driving Tissue Morphogenesis. *Nature Materials* **21**, 588 (2022).
- C. Guillot and T. Lecuit. Mechanics of Epithelial Tissue Homeostasis and Morphogenesis. *Science* **340**, 1185 (2013).
- C. F. Guimarães, L. Gasperini, A. P. Marques, and R. L. Reis. The Stiffness of Living Tissues and Its Implications for Tissue Engineering. *Nature Reviews Materials* **5**, 351 (2020).
- H. Guo, M. Swan, and B. He. Optogenetic Inhibition of Actomyosin Reveals Mechanical Bistability of the Mesoderm Epithelium during Drosophila Mesoderm Invagination. *eLife* **11**, e69082 (2022).
- J. H. Gutzman, E. Graeden, I. Brachmann, S. Yamazoe, J. K. Chen, and H. Sive. Basal Constriction during Midbrain–Hindbrain Boundary Morphogenesis Is Mediated by Wnt5b and Focal Adhesion Kinase. *Biology Open* **7**, bio034520 (2018).
- J. Guyon, P.-O. Strale, I. Romero-Garmendia, A. Bikfalvi, V. Studer, and T. Daubon. Co-Culture of Glioblastoma Stem-like Cells on Patterned Neurons to Study Migration and Cellular Interactions. *Journal of Visualized Experiments* , 62213 (2021).
- S. L. Haigo and D. Bilder. Global Tissue Revolutions in a Morphogenetic Movement Controlling Elongation. *Science* **331**, 1071 (2011).
- C. Halley. Public Dissection Was a Gruesome Spectacle. <https://daily.jstor.org/public-dissection-gruesome-spectacle/> (2019).

- E. Hannezo, B. Dong, P. Recho, J.-F. Joanny, and S. Hayashi. Cortical instability drives periodic supracellular actin pattern formation in epithelial tubes. *Proceedings of the National Academy of Sciences* **112**, 8620 (2015).
- E. Hannezo and C.-P. Heisenberg. Rigidity Transitions in Development and Disease. *Trends in Cell Biology* **32**, 433 (2022).
- A. K. Harris, P. Wild, and D. Stopak. Silicone Rubber Substrata: A New Wrinkle in the Study of Cell Locomotion. *Science* **208**, 177 (1980).
- A. R. Harris, L. Peter, J. Bellis, B. Baum, A. J. Kabla, and G. T. Charras. Characterizing the Mechanics of Cultured Cell Monolayers. *Proceedings of the National Academy of Sciences* **109**, 16449 (2012).
- M. Hatzfeld, R. Keil, and T. M. Magin. Desmosomes and Intermediate Filaments: Their Consequences for Tissue Mechanics. *Cold Spring Harbor Perspectives in Biology* **9**, a029157 (2017).
- Q. He, T. Okajima, H. Onoe, A. Subagyo, K. Sueoka, and K. Kurabayashi-Shigetomi. Origami-Based Self-Folding of Co-Cultured NIH/3T3 and HepG2 Cells into 3D Microstructures. *Scientific Reports* **8**, 4556 (2018).
- N. C. Heer and A. C. Martin. Tension, Contraction and Tissue Morphogenesis. *Development* **144**, 4249 (2017).
- P. Helm, M. F. Beg, M. I. Miller, and R. L. Winslow. Measuring and Mapping Cardiac Fiber and Laminar Architecture Using Diffusion Tensor MR Imaging. *Annals of the New York Academy of Sciences* **1047**, 296 (2005).
- M. Hofer and M. P. Lutolf. Engineering Organoids. *Nature Reviews Materials* **6**, 402 (2021).
- G. A. Holzapfel. *Nonlinear Solid Mechanics: A Continuum Approach for Engineering* (Wiley, 2000).
- G. A. Holzapfel, R. W. Ogden, and S. Sherifova. On Fibre Dispersion Modelling of Soft Biological Tissues: A Review. *Proceedings of the Royal Society A: Mathematical, Physical and Engineering Sciences* **475**, 20180736 (2019).

- N. S. Houssin, J. B. Martin, V. Coppola, S. O. Yoon, and T. F. Plageman. Formation and Contraction of Multicellular Actomyosin Cables Facilitate Lens Placode Invagination. *Developmental Biology* **462**, 36 (2020).
- A. J. Hughes, H. Miyazaki, M. C. Coyle, J. Zhang, M. T. Laurie, D. Chu, Z. Vavrušová, R. A. Schneider, O. D. Klein, and Z. J. Gartner. Engineered Tissue Folding by Mechanical Compaction of the Mesenchyme. *Developmental Cell* **44**, 165 (2018).
- D. Huh, B. D. Matthews, A. Mammoto, M. Montoya-Zavala, H. Y. Hsin, and D. E. Ingber. Reconstituting Organ-Level Lung Functions on a Chip. *Science* **328**, 1662 (2010).
- J. D. Humphrey. *Cardiovascular Solid Mechanics* (Springer New York, New York, NY, 2002).
- J. D. Humphrey, E. R. Dufresne, and M. A. Schwartz. Mechanotransduction and Extracellular Matrix Homeostasis. *Nature Reviews Molecular Cell Biology* **15**, 802 (2014).
- D. E. Ingber. From Mechanobiology to Developmentally Inspired Engineering. *Philosophical Transactions of the Royal Society B: Biological Sciences* **373**, 20170323 (2018).
- S. Ishida-Ishihara, M. Akiyama, K. Furusawa, I. Naguro, H. Ryuno, T. Sushida, S. Ishihara, and H. Haga. Osmotic Gradient Induces Stable Dome Morphogenesis on Extracellular Matrix. *Journal of Cell Science* , jcs.243865 (2020).
- T. Ishiguro, H. Ohata, A. Sato, K. Yamawaki, T. Enomoto, and K. Okamoto. Tumor-Derived Spheroids: Relevance to Cancer Stem Cells and Clinical Applications. *Cancer Science* **108**, 283 (2017).
- K. Ishihara and E. M. Tanaka. Spontaneous Symmetry Breaking and Pattern Formation of Organoids. *Current Opinion in Systems Biology* • Big Data Acquisition and Analysis • Development and Differentiation. **11**, 123 (2018).
- E. Izquierdo, T. Quinkler, and S. De Renzis. Guided Morphogenesis through Optogenetic Activation of Rho Signalling during Early Drosophila Embryogenesis. *Nature Communications* **9**, 2366 (2018).

- S. Jalal, S. Shi, V. Acharya, R. Y.-J. Huang, V. Viasnoff, A. D. Bershadsky, and Y. H. Tee. Actin Cytoskeleton Self-Organization in Single Epithelial Cells and Fibroblasts under Isotropic Confinement. *Journal of Cell Science* **132**, jcs220780 (2019).
- F. Jülicher, S. W. Grill, and G. Salbreux. Hydrodynamic Theory of Active Matter. *Reports on Progress in Physics* **81**, 076601 (2018).
- E. Karzbrun, A. H. Khankhel, H. C. Megale, S. M. K. Glasauer, Y. Wyle, G. Britton, A. Warmflash, K. S. Kosik, E. D. Siggia, B. I. Shraiman, and S. J. Streichan. Human Neural Tube Morphogenesis in Vitro by Geometric Constraints. *Nature* **599**, 268 (2021).
- E. Karzbrun, A. Kshirsagar, S. R. Cohen, J. H. Hanna, and O. Reiner. Human Brain Organoids on a Chip Reveal the Physics of Folding. *Nature Physics* **14**, 515 (2018).
- J. Z. Kechagia, J. Ivaska, and P. Roca-Cusachs. Integrins as Biomechanical Sensors of the Microenvironment. *Nature Reviews Molecular Cell Biology* **20**, 457 (2019).
- M. Kelkar, P. Bohec, and G. Charras. Mechanics of the Cellular Actin Cortex: From Signalling to Shape Change. *Current Opinion in Cell Biology* **66**, 69 (2020).
- N. Khalilgharibi, J. Fouchard, N. Asadipour, R. Barrientos, M. Duda, A. Bonfanti, A. Yonis, A. Harris, P. Mosaffa, Y. Fujita, A. Kabla, Y. Mao, B. Baum, J. J. Muñoz, M. Miodownik, and G. Charras. Stress Relaxation in Epithelial Monolayers Is Controlled by the Actomyosin Cortex. *Nature Physics* **15**, 839 (2019).
- D. Khoromskaia and G. Salbreux. Active Morphogenesis of Patterned Epithelial Shells. *eLife* **12**, e75878 (2023).
- E. J. Y. Kim, E. Korotkevich, and T. Hiiragi. Coordination of Cell Polarity, Mechanics and Fate in Tissue Self-organization. *Trends in Cell Biology* **28**, 541 (2018).
- R. J. Klebe, A. Grant, G. Grant, and P. Ghosh. Cyclic-AMP Deficient MDCK Cells Form Tubules. *Journal of Cellular Biochemistry* **59**, 453 (1995).
- P. Kollmannsberger and B. Fabry. Linear and Nonlinear Rheology of Living Cells. *Annual Review of Materials Research* **41**, 75 (2011).
- A. P. Kourouklis and C. M. Nelson. Modeling Branching Morphogenesis Using Materials with Programmable Mechanical Instabilities. *Current Opinion in Biomedical*

- Engineering Tissue Engineering and Regenerative Medicine / Biomaterials.* **6**, 66 (2018).
- A. Kumar, J. K. Placone, and A. J. Engler. Understanding the Extracellular Forces That Determine Cell Fate and Maintenance. *Development* **144**, 4261 (2017).
- R. Kusters, C. Simon, R. L. D. Santos, V. Caorsi, S. Wu, J.-F. Joanny, P. Sens, and C. Sykes. Actin Shells Control Buckling and Wrinkling of Biomembranes. *Soft Matter* **15**, 9647 (2019).
- A. Labernadie and X. Trepat. Sticking, Steering, Squeezing and Shearing: Cell Movements Driven by Heterotypic Mechanical Forces. *Current Opinion in Cell Biology* **54**, 57 (2018).
- B. Ladoux and R.-M. Mège. Mechanobiology of Collective Cell Behaviours. *Nature Reviews Molecular Cell Biology* **18**, 743 (2017).
- E. Latorre, S. Kale, L. Casares, M. Gómez-González, M. Uroz, L. Valon, R. V. Nair, E. Garreta, N. Montserrat, A. del Campo, B. Ladoux, M. Arroyo, and X. Trepat. Active Superelasticity in Three-Dimensional Epithelia of Controlled Shape. *Nature* **563**, 203 (2018).
- M. Le Merrer, D. Quéré, and C. Clanet. Buckling of Viscous Filaments of a Fluid under Compression Stresses. *Phys. Rev. Lett.* **109**, 064502 (2012).
- T. Lecuit, P.-F. Lenne, and E. Munro. Force Generation, Transmission, and Integration during Cell and Tissue Morphogenesis. *Annual Review of Cell and Developmental Biology* **27**, 157 (2011).
- A. Lee, F. López Jiménez, J. Marthelot, J. W. Hutchinson, and P. M. Reis. The Geometric Role of Precisely Engineered Imperfections on the Critical Buckling Load of Spherical Elastic Shells. *Journal of Applied Mechanics* **83**, 111005 (2016).
- S. E. Leggett, A. M. Hruska, M. Guo, and I. Y. Wong. The Epithelial-Mesenchymal Transition and the Cytoskeleton in Bioengineered Systems. *Cell Communication and Signaling* **19**, 32 (2021).
- J. Leighton. BRIEF HISTORY OF ACTIVE TRANSPORT IN CULTURE. *Annals of the New York Academy of Sciences* **372**, 352 (1981).

- J. Leighton, Z. Brada, L. W. Estes, and G. Justh. Secretory Activity and Oncogenicity of a Cell Line (MDCK) Derived from Canine Kidney. *Science* **163**, 472 (1969).
- P.-F. Lenne and V. Trivedi. Sculpting Tissues by Phase Transitions. *Nature Communications* **13**, 664 (2022).
- J. E. Lever. Regulation of Dome Formation in Differentiated Epithelial Cell Cultures. *Journal of Supramolecular Structure* **12**, 259 (1979).
- H. Liang and L. Mahadevan. The Shape of a Long Leaf. *Proceedings of the National Academy of Sciences* **106**, 22049 (2009).
- A. J. Lomakin, C. J. Cattin, D. Cuvelier, Z. Alraies, M. Molina, G. P. F. Nader, N. Srivastava, P. J. Sáez, J. M. García-Arcos, I. Y. Zhitnyak, A. Bhargava, M. K. Driscoll, E. S. Welf, R. Fiolka, R. J. Petrie, N. S. De Silva, J. M. González-Granado, N. Manel, A. M. Lennon-Duménil, D. J. Müller, and M. Piel. The Nucleus Acts as a Ruler Tailoring Cell Responses to Spatial Constraints. *Science* **370**, eaba2894 (2020).
- M. Luciano, S.-L. Xue, W. H. De Vos, L. Redondo-Morata, M. Surin, F. Lafont, E. Hannezo, and S. Gabriele. Cell Monolayers Sense Curvature by Exploiting Active Mechanics and Nuclear Mechanoadaptation. *Nature Physics* **17**, 1382 (2021).
- K. MacCord. Epithelium. (2012).
- E. Mailand, E. Özeliç, J. Kim, M. Rüegg, O. Chaliotis, J. Märki, N. Bouklas, and M. S. Sakar. Tissue Engineering with Mechanically Induced Solid-Fluid Transitions. *Advanced Materials* **34**, 2106149 (2022).
- A. Malandrino, M. Mak, R. D. Kamm, and E. Moeendarbary. Complex Mechanics of the Heterogeneous Extracellular Matrix in Cancer. *Extreme Mechanics Letters* **21**, 25 (2018).
- A. M. Marchiando, W. V. Graham, and J. R. Turner. Epithelial Barriers in Homeostasis and Disease. *Annual Review of Pathology: Mechanisms of Disease* **5**, 119 (2010).
- A. Marín-Llauradó, S. Kale, A. Ouza, R. Sunyer, A. Torres-Sánchez, E. Latorre, M. Gómez-González, P. Roca-Cusachs, M. Arroyo, and X. Trepat. Mapping Mechanical Stress in Curved Epithelia of Designed Size and Shape. (2022).

- Y. Maroudas-Sacks, L. Garion, L. Shani-Zerbib, A. Livshits, E. Braun, and K. Keren. Topological Defects in the Nematic Order of Actin Fibres as Organization Centres of Hydra Morphogenesis. *Nature Physics* **17**, 251 (2021).
- A. C. Martin, M. Kaschube, and E. F. Wieschaus. Pulsed Contractions of an Actin–Myosin Network Drive Apical Constriction. *Nature* **457**, 495 (2009).
- G. Martínez-Ara, N. Taberner, M. Takayama, E. Sandaltzopoulou, C. E. Villava, M. Bosch-Padrós, N. Takata, X. Trepat, M. Eiraku, and M. Ebisuya. Optogenetic Control of Apical Constriction Induces Synthetic Morphogenesis in Mammalian Tissues. *Nature Communications* **13**, 5400 (2022).
- M. Matejčić and X. Trepat. Buckling Up from the Bottom. *Developmental Cell* **54**, 569 (2020).
- M. Matejčić and X. Trepat. Mechanobiological Approaches to Synthetic Morphogenesis: Learning by Building. *Trends in Cell Biology* (2022). 10.1016/j.tcb.2022.06.013.
- A. F. Mertz, Y. Che, S. Banerjee, J. M. Goldstein, K. A. Rosowski, S. F. Revilla, C. M. Niessen, M. C. Marchetti, E. R. Dufresne, and V. Horsley. Cadherin-Based Intercellular Adhesions Organize Epithelial Cell–Matrix Traction Forces. *Proceedings of the National Academy of Sciences* **110**, 842 (2013).
- H. A. Messal, S. Alt, R. M. M. Ferreira, C. Gribben, V. M.-Y. Wang, C. G. Cotoi, G. Salbreux, and A. Behrens. Tissue Curvature and Apicobasal Mechanical Tension Imbalance Instruct Cancer Morphogenesis. *Nature* **566**, 126 (2019).
- E. Moeendarbary, L. Valon, M. Fritzsche, A. R. Harris, D. A. Moulding, A. J. Thrasher, E. Stride, L. Mahadevan, and G. T. Charras. The Cytoplasm of Living Cells Behaves as a Poroelastic Material. *Nature Materials* **12**, 253 (2013).
- M. R. Mofrad. Rheology of the Cytoskeleton. *Annual Review of Fluid Mechanics* **41**, 433 (2009).
- A. Mongera, M. Pochitaloff, H. J. Gustafson, G. A. Stooke-Vaughan, P. Rowghanian, S. Kim, and O. Campàs. Mechanics of the Cellular Microenvironment as Probed by Cells in Vivo during Zebrafish Presomitic Mesoderm Differentiation. *Nature Materials* **22**, 135 (2023).

- B. Monier, M. Gettings, G. Gay, T. Mangeat, S. Schott, A. Guarner, and M. Suzanne. Apico-Basal Forces Exerted by Apoptotic Cells Drive Epithelium Folding. *Nature* **518**, 245 (2015).
- R. Morizane and J. V. Bonventre. Generation of Nephron Progenitor Cells and Kidney Organoids from Human Pluripotent Stem Cells. *Nature Protocols* **12**, 195 (2017).
- J. M. Muncie, N. M. E. Ayad, J. N. Lakins, X. Xue, J. Fu, and V. M. Weaver. Mechanical Tension Promotes Formation of Gastrulation-like Nodes and Patterns Mesoderm Specification in Human Embryonic Stem Cells. *Developmental Cell* **55**, 679 (2020).
- A. Munjal, E. Hannezo, T. Y. C. Tsai, T. J. Mitchison, and S. G. Megason. Extracellular Hyaluronate Pressure Shaped by Cellular Tethers Drives Tissue Morphogenesis. *Cell* **184**, 6313 (2021).
- M. P. Murrell and M. L. Gardel. F-Actin Buckling Coordinates Contractility and Severing in a Biomimetic Actomyosin Cortex. *Proceedings of the National Academy of Sciences* **109**, 20820 (2012).
- C. M. Nelson, J. P. Gleghorn, M.-F. Pang, J. M. Jaslove, K. Goodwin, V. D. Varner, E. Miller, D. C. Radisky, and H. A. Stone. Microfluidic Chest Cavities Reveal That Transmural Pressure Controls the Rate of Lung Development. *Development* **144**, 4328 (2017).
- C. M. Nelson, J. L. Inman, and M. J. Bissell. Three-Dimensional Lithographically Defined Organotypic Tissue Arrays for Quantitative Analysis of Morphogenesis and Neoplastic Progression. *Nature Protocols* **3**, 674 (2008).
- C. M. Nelson, R. P. Jean, J. L. Tan, W. F. Liu, N. J. Sniadecki, A. A. Spector, and C. S. Chen. Emergent Patterns of Growth Controlled by Multicellular Form and Mechanics. *Proceedings of the National Academy of Sciences* **102**, 11594 (2005).
- G. Odell, G. Oster, P. Alberch, and B. Burnside. The Mechanical Basis of Morphogenesis. *Developmental Biology* **85**, 446 (1981).
- S. Okuda, N. Takata, Y. Hasegawa, M. Kawada, Y. Inoue, T. Adachi, Y. Sasai, and M. Eiraku. Strain-Triggered Mechanical Feedback in Self-Organizing Optic-Cup Morphogenesis. *Science Advances* **4**, eaau1354 (2018).

- A. T. Oratis, J. W. M. Bush, H. A. Stone, and J. C. Bird. A new wrinkle on liquid sheets: Turning the mechanism of viscous bubble collapse upside down. *Science* **369**, 685 (2020). <https://www.science.org/doi/pdf/10.1126/science.aba0593>.
- D. Oriola, M. Marin-Riera, K. Anlaş, N. Gritti, M. Sanaki-Matsumiya, G. Aalderink, M. Ebisuya, J. Sharpe, and V. Trivedi. Arrested Coalescence of Multicellular Aggregates. *Soft Matter* **18**, 3771 (2022).
- M. Osterfield, C. A. Berg, and S. Y. Shvartsman. Epithelial Patterning, Morphogenesis, and Evolution: Drosophila Eggshell as a Model. *Developmental Cell* **41**, 337 (2017).
- A. Ouzeri and M. Arroyo. Theory of Multiscale Epithelial Mechanics under Stretch: From Active Gels to Vertex Models. (2023).
- T. G. Oyama, K. Oyama, H. Miyoshi, and M. Taguchi. 3D Cell Sheets Formed via Cell-Driven Buckling-Delamination of Patterned Thin Films. *Materials & Design* **208**, 109975 (2021).
- Ö. Özgürç, L. de Plater, V. Kapoor, A. F. Tortorelli, A. G. Clark, and J.-L. Maître. Cortical Softening Elicits Zygotic Contractility during Mouse Preimplantation Development. *PLOS Biology* **20**, e3001593 (2022).
- A. Pal, V. Restrepo, D. Goswami, and R. V. Martinez. Exploiting Mechanical Instabilities in Soft Robotics: Control, Sensing, and Actuation. *Advanced Materials* **33**, 2006939 (2021).
- M. E. Pallarès, I. Pi-Jaumà, I. C. Fortunato, V. Grazu, M. Gómez-González, P. Roca-Cusachs, J. M. de la Fuente, R. Alert, R. Sunyer, J. Casademunt, and X. Trepat. Stiffness-Dependent Active Wetting Enables Optimal Collective Cell Durotaxis. *Nature Physics* , 1 (2022).
- M. A. Palmer, B. A. Nerger, K. Goodwin, A. Sudhakar, S. B. Lemke, P. T. Ravindran, J. E. Toettcher, A. Košmrlj, and C. M. Nelson. Stress Ball Morphogenesis: How the Lizard Builds Its Lung. *Science Advances* **7**, eabk0161 (2021).
- K. H. Palmquist, S. F. Tiemann, F. L. Ezzeddine, S. Yang, C. R. Pfeifer, A. Erzberger, A. R. Rodrigues, and A. E. Shyer. Reciprocal Cell-ECM Dynamics Generate Supracellular Fluidity Underlying Spontaneous Follicle Patterning. *Cell* **185**, 1960 (2022).

- J.-A. Park, J. H. Kim, D. Bi, J. A. Mitchel, N. T. Qazvini, K. Tantisira, C. Y. Park, M. McGill, S.-H. Kim, B. Gweon, J. Notbohm, R. Steward Jr, S. Burger, S. H. Randell, A. T. Kho, D. T. Tambe, C. Hardin, S. A. Shore, E. Israel, D. A. Weitz, D. J. Tschumperlin, E. P. Henske, S. T. Weiss, M. L. Manning, J. P. Butler, J. M. Drazen, and J. J. Fredberg. Unjamming and Cell Shape in the Asthmatic Airway Epithelium. *Nature Materials* **14**, 1040 (2015).
- C. Pérez-González, R. Alert, C. Blanch-Mercader, M. Gómez-González, T. Kolodziej, E. Bazellieres, J. Casademunt, and X. Trepat. Active Wetting of Epithelial Tissues. *Nature Physics* **15**, 79 (2019).
- C. Pérez-González, G. Ceada, F. Greco, M. Matejčić, M. Gómez-González, N. Castro, A. Menendez, S. Kale, D. Krndija, A. G. Clark, V. R. Gannavarapu, A. Álvarez-Varela, P. Roca-Cusachs, E. Batlle, D. M. Vignjevic, M. Arroyo, and X. Trepat. Mechanical Compartmentalization of the Intestinal Organoid Enables Crypt Folding and Collective Cell Migration. *Nature Cell Biology* **23**, 745 (2021).
- P. Popowicz, J. Kurzyca, and S. Popowicz. “Dome-curve” – Three Size Classes of Domes of MDCK Epithelial Monolayer. *Experimental pathology* **29**, 147 (1986).
- S. Porazinski, H. Wang, Y. Asaoka, M. Behrndt, T. Miyamoto, H. Morita, S. Hata, T. Sasaki, S. F. G. Krens, Y. Osada, S. Asaka, A. Momoi, S. Linton, J. B. Miesfeld, B. A. Link, T. Senga, A. Castillo-Morales, A. O. Urrutia, N. Shimizu, H. Nagase, S. Matsuura, S. Bagby, H. Kondoh, H. Nishina, C.-P. Heisenberg, and M. Furutani-Seiki. YAP Is Essential for Tissue Tension to Ensure Vertebrate 3D Body Shape. *Nature* **521**, 217 (2015).
- L. S. Prahl, C. M. Porter, J. Liu, J. M. Viola, and A. J. Hughes. Independent Control over Cell Patterning and Adhesion on Hydrogel Substrates for Tissue Interface Mechanobiology. (2022).
- J. Prost, F. Jülicher, and J.-F. Joanny. Active gel physics. *Nature Physics* **11**, 111 (2015).
- P. A. Pullarkat, P. A. Fernández, and A. Ott. Rheological properties of the Eukaryotic cell cytoskeleton. *Physics Reports* **449**, 29 (2007). nonequilibrium physics: From complex fluids to biological systems III. Living systems.
- P. Roca-Cusachs, V. Conte, and X. Trepat. Quantifying Forces in Cell Biology. *Nature Cell Biology* **19**, 742 (2017).

- G. Salbreux and F. Jülicher. Mechanics of Active Surfaces. *Physical Review E* **96**, 032404 (2017).
- P. Samal, C. van Blitterswijk, R. Truckenmüller, and S. Giselbrecht. Grow with the Flow: When Morphogenesis Meets Microfluidics. *Advanced Materials* **31**, 1805764 (2019).
- S. Sances, R. Ho, G. Vatine, D. West, A. Laperle, A. Meyer, M. Godoy, P. S. Kay, B. Mandefro, S. Hatata, C. Hinojosa, N. Wen, D. Sareen, G. A. Hamilton, and C. N. Svendsen. Human iPSC-Derived Endothelial Cells and Microengineered Organ-Chip Enhance Neuronal Development. *Stem Cell Reports* **10**, 1222 (2018).
- T. B. Saw, W. Xi, B. Ladoux, and C. T. Lim. Biological Tissues as Active Nematic Liquid Crystals. *Advanced Materials* **30**, 1802579 (2018).
- B. Schamberger, A. Roschger, R. Ziege, K. Anselme, M. B. Amar, M. Bykowski, A. P. G. Castro, A. Cipitria, R. Coles, R. Dimova, M. Eder, S. Ehrig, L. M. Escudero, M. E. Evans, P. R. Fernandes, P. Fratzl, L. Geris, N. Gierlinger, E. Hannezo, A. Iglič, J. J. K. Kirkensgaard, P. Kollmannsberger, Ł. Kowalewska, N. A. Kurniawan, I. Papantonioiu, L. Pieuchot, T. H. V. Pires, L. Renner, A. Sageman-Furnas, G. E. Schröder-Turk, A. Sengupta, V. R. Sharma, A. Tagua, C. Tomba, X. Trepat, S. L. Waters, E. Yeo, C. M. Bidan, and J. W. C. Dunlop. Curvature in Biological Systems: Its Quantification, Emergence and Implications across the Scales. *Advanced Materials* , e2206110 (2022).
- M. F. Schliffka and J.-L. Maître. Stay Hydrated: Basolateral Fluids Shaping Tissues. *Current Opinion in Genetics & Development* Developmental Mechanisms, Patterning and Evolution. **57**, 70 (2019).
- F. Schöck and N. Perrimon. Molecular Mechanisms of Epithelial Morphogenesis. *Annual Review of Cell and Developmental Biology* **18**, 463 (2002).
- X. Serra-Picamal, V. Conte, R. Vincent, E. Anon, D. T. Tambe, E. Bazellieres, J. P. Butler, J. J. Fredberg, and X. Trepat. Mechanical Waves during Tissue Expansion. *Nature Physics* **8**, 628 (2012).
- F. Serwane, A. Mongera, P. Rowghanian, D. A. Kealhofer, A. A. Lucio, Z. M. Hockenberry, and O. Campàs. In Vivo Quantification of Spatially Varying Mechanical Properties in Developing Tissues. *Nature Methods* **14**, 181 (2017).

- G. Shah, K. Thierbach, B. Schmid, J. Waschke, A. Reade, M. Hlawitschka, I. Roeder, N. Scherf, and J. Huisken. Multi-Scale Imaging and Analysis Identify Pan-Embryo Cell Dynamics of Germ-layer Formation in Zebrafish. *Nature Communications* **10**, 5753 (2019).
- A. Shellard and R. Mayor. Collective Durotaxis along a Self-Generated Stiffness Gradient in Vivo. *Nature* **600**, 690 (2021).
- A. E. Shyer, A. R. Rodrigues, G. G. Schroeder, E. Kassianidou, S. Kumar, and R. M. Harland. Emergent Cellular Self-Organization and Mechanosensation Initiate Follicle Pattern in the Avian Skin. *Science* **357**, 811 (2017).
- A. E. Shyer, T. Tallinen, N. L. Nerurkar, Z. Wei, E. S. Gil, D. L. Kaplan, C. J. Tabin, and L. Mahadevan. Villification: How the Gut Gets Its Villi. *Science* **342**, 212 (2013).
- J. Sidhaye and C. Norden. Concerted Action of Neuroepithelial Basal Shrinkage and Active Epithelial Migration Ensures Efficient Optic Cup Morphogenesis. *eLife* **6**, e22689 (2017).
- E. Sollier, C. Murray, P. Maoddi, and D. D. Carlo. Rapid Prototyping Polymers for Microfluidic Devices and High Pressure Injections. *Lab on a Chip* **11**, 3752 (2011).
- A. E. Stanton, X. Tong, and F. Yang. Extracellular Matrix Type Modulates Mechanotransduction of Stem Cells. *Acta Biomaterialia* **96**, 310 (2019).
- A. Stokkermans, A. Chakrabarti, K. Subramanian, L. Wang, S. Yin, P. Moghe, P. Steenbergen, G. Mönke, T. Hiiragi, R. Prevedel, L. Mahadevan, and A. Ikmi. Muscular Hydraulics Drive Larva-Polyp Morphogenesis. *Current Biology* **32**, 4707 (2022).
- A. Stokkermans, A. Chakrabarti, L. Wang, P. Moghe, K. Subramanian, P. Steenbergen, G. Mönke, T. Hiiragi, R. Prevedel, L. Mahadevan, and A. Ikmi. Ethology of Morphogenesis Reveals the Design Principles of Cnidarian Size and Shape Development. (2021).
- L. Sui, S. Alt, M. Weigert, N. Dye, S. Eaton, F. Jug, E. W. Myers, F. Jülicher, G. Salbreux, and C. Dahmann. Differential Lateral and Basal Tension Drive Folding of Drosophila Wing Discs through Two Distinct Mechanisms. *Nature Communications* **9**, 4620 (2018).

- A. Sumi, P. Hayes, A. D'Angelo, J. Colombelli, G. Salbreux, K. Dierkes, and J. Solon. Adherens Junction Length during Tissue Contraction Is Controlled by the Mechanosensitive Activity of Actomyosin and Junctional Recycling. *Developmental Cell* **47**, 453 (2018).
- R. Sunyer, V. Conte, J. Escribano, A. Elosegui-Artola, A. Labernadie, L. Valon, D. Navajas, J. M. García-Aznar, J. J. Muñoz, P. Roca-Cusachs, and X. Trepat. Collective Cell Durotaxis Emerges from Long-Range Intercellular Force Transmission. *Science* **353**, 1157 (2016).
- Z. A. Syed, A.-L. Bougé, S. Byri, T. M. Chavoshi, E. Tång, H. Bouhin, I. F. van Dijk-Härd, and A. Uv. A Luminal Glycoprotein Drives Dose-Dependent Diameter Expansion of the *Drosophila Melanogaster* Hindgut Tube. *PLOS Genetics* **8**, e1002850 (2012).
- T. Tallinen, J. Y. Chung, F. Rousseau, N. Girard, J. Lefèvre, and L. Mahadevan. On the Growth and Form of Cortical Convolutions. *Nature Physics* **12**, 588 (2016).
- D. T. Tambe, C. Corey Hardin, T. E. Angelini, K. Rajendran, C. Y. Park, X. Serra-Picamal, E. H. Zhou, M. H. Zaman, J. P. Butler, D. A. Weitz, J. J. Fredberg, and X. Trepat. Collective Cell Guidance by Cooperative Intercellular Forces. *Nature Materials* **10**, 469 (2011).
- W. Tang, A. Das, A. F. Pegoraro, Y. L. Han, J. Huang, D. A. Roberts, H. Yang, J. J. Fredberg, D. N. Kotton, D. Bi, and M. Guo. Collective Curvature Sensing and Fluidity in Three-Dimensional Multicellular Systems. *Nature Physics* **18**, 1371 (2022).
- C. Tanner, D. Frambach, and D. Misfeldt. Transepithelial Transport in Cell Culture. A Theoretical and Experimental Analysis of the Biophysical Properties of Domes. *Biophysical Journal* **43**, 183 (1983).
- D. W. Thompson. *On Growth and Form*. repr ed. (Univ. Pr, Cambridge, 1979).
- S. Tili, E. Gauquelin, B. Li, O. Cardoso, B. Ladoux, H. Delanoë-Ayari, and F. Graner. Collective Cell Migration without Proliferation: Density Determines Cell Velocity and Wave Velocity. *Royal Society Open Science* **5**, 172421 (2018).

- I. Tobasco, Y. Timounay, D. Todorova, G. C. Leggat, J. D. Paulsen, and E. Katifori. Exact Solutions for the Wrinkle Patterns of Confined Elastic Shells. *Nature Physics* **18**, 1099 (2022).
- C. Tomba, V. Luchnikov, L. Barberi, C. Blanch-Mercader, and A. Roux. Epithelial Cells Adapt to Curvature Induction via Transient Active Osmotic Swelling. *Developmental Cell* **57**, 1257 (2022).
- N. Torras, M. García-Díaz, V. Fernández-Majada, and E. Martínez. Mimicking Epithelial Tissues in Three-Dimensional Cell Culture Models. *Frontiers in Bioengineering and Biotechnology* **6** (2018).
- A. Torres-Sánchez, M. Kerr Winter, and G. Salbreux. Tissue Hydraulics: Physics of Lumen Formation and Interaction. *Cells & Development Quantitative Cell and Developmental Biology*. **168**, 203724 (2021).
- C. Trentesaux, T. Yamada, O. D. Klein, and W. A. Lim. Harnessing Synthetic Biology to Engineer Organoids and Tissues. *Cell Stem Cell* **30**, 10 (2023).
- X. Trepat and E. Sahai. Mesoscale Physical Principles of Collective Cell Organization. *Nature Physics* **14**, 671 (2018).
- A. Trushko, I. Di Meglio, A. Merzouki, C. Blanch-Mercader, S. Abuhattum, J. Guck, K. Alessandri, P. Nassoy, K. Kruse, B. Chopard, and A. Roux. Buckling of an Epithelium Growing under Spherical Confinement. *Developmental Cell* **54**, 655 (2020).
- J. D. Valentich, R. Tchao, and J. Leighton. Hemicyst Formation Stimulated by Cyclic AMP in Dog Kidney Cell Line MDCK. *Journal of Cellular Physiology* **100**, 291 (1979).
- M. Valet, E. D. Siggia, and A. H. Brivanlou. Mechanical Regulation of Early Vertebrate Embryogenesis. *Nature Reviews Molecular Cell Biology* **23**, 169 (2022).
- V. D. Varner, J. P. Gleghorn, E. Miller, D. C. Radisky, and C. M. Nelson. Mechanically Patterning the Embryonic Airway Epithelium. *Proceedings of the National Academy of Sciences* **112**, 9230 (2015).
- S. R. K. Vedula, M. C. Leong, T. L. Lai, P. Hersen, A. J. Kabla, C. T. Lim, and B. Ladoux. Emerging Modes of Collective Cell Migration Induced by Geometrical Constraints. *Proceedings of the National Academy of Sciences* **109**, 12974 (2012).

- J. V. Veenvliet, P.-F. Lenne, D. A. Turner, I. Nachman, and V. Trivedi. Sculpting with Stem Cells: How Models of Embryo Development Take Shape. *Development* **148**, dev192914 (2021).
- V. Venturini, F. Pezzano, F. Català Castro, H.-M. Häkkinen, S. Jiménez-Delgado, M. Colomer-Rosell, M. Marro, Q. Tolosa-Ramon, S. Paz-López, M. A. Valverde, J. Weghuber, P. Loza-Alvarez, M. Krieg, S. Wieser, and V. Ruprecht. The Nucleus Measures Shape Changes for Cellular Proprioception to Control Dynamic Cell Behavior. *Science* **370**, eaba2644 (2020).
- S. Vianello and M.P. Lutolf. Understanding the Mechanobiology of Early Mammalian Development through Bioengineered Models. *Developmental Cell* **48**, 751 (2019).
- T. Vignaud, L. Blanchoin, and M. Théry. Directed Cytoskeleton Self-Organization. *Trends in Cell Biology* Special Issue – Synthetic Cell Biology. **22**, 671 (2012).
- R. Virchow, F. Chance, J. Goodsir, K. C. London, and P. I. of Berlin. *Cellular Pathology as Based upon Physiological and Pathological Histology; Twenty Lectures Delivered in the Pathological Institute of Berlin during the Months of February, March, and April, 1858* (John Churchill, London, 1860) pp. 1–546.
- A. Voss-Böhme. Multi-Scale Modeling in Morphogenesis: A Critical Analysis of the Cellular Potts Model. *PLOS ONE* **7**, e42852 (2012).
- K. Wagh, M. Ishikawa, D. A. Garcia, D. A. Stavreva, A. Upadhyaya, and G. L. Hager. Mechanical Regulation of Transcription: Recent Advances. *Trends in Cell Biology* **31**, 457 (2021).
- D. A. C. Walma and K. M. Yamada. The Extracellular Matrix in Development. *Development* **147**, dev175596 (2020).
- Y. Wang and J. Qian. Buckling of Filamentous Actin Bundles in Filopodial Protrusions. *Acta Mechanica Sinica* **35**, 365 (2019).
- A. Warmflash, B. Sorre, F. Etoc, E. D. Siggia, and A. H. Brivanlou. A Method to Recapitulate Early Embryonic Spatial Patterning in Human Embryonic Stem Cells. *Nature Methods* **11**, 847 (2014).
- C. M. Waters, E. Roan, and D. Navajas. Mechanobiology in Lung Epithelial Cells: Measurements, Perturbations, and Responses. *Comprehensive Physiology* **2**, 1 (2012).

- Q. Wen and P. A. Janmey. Polymer Physics of the Cytoskeleton. *Current Opinion in Solid State and Materials Science* **15**, 177 (2011).
- H. H. Wensink, J. Dunkel, S. Heidenreich, K. Drescher, R. E. Goldstein, H. Löwen, and J. M. Yeomans. Meso-Scale Turbulence in Living Fluids. *Proceedings of the National Academy of Sciences* **109**, 14308 (2012).
- S. Wolfram. The Scientist Who Cracked Biological Mysteries With Math | Backchannel. *Wired* (2017).
- F. Wottawah, S. Schinkinger, B. Lincoln, R. Ananthakrishnan, M. Romeyke, J. Guck, and J. Käs. Optical Rheology of Biological Cells. *Phys. Rev. Lett.* **94**, 098103 (2005).
- N. A. Wright and R. Poulsom. Omnis Cellula e Cellula Revisited: Cell Biology as the Foundation of Pathology. *The Journal of Pathology* **226**, 145 (2012).
- T. Wyatt, B. Baum, and G. Charras. A Question of Time: Tissue Adaptation to Mechanical Forces. *Current Opinion in Cell Biology* Cell Architecture. **38**, 68 (2016).
- T. P. J. Wyatt, J. Fouchard, A. Lisica, N. Khalilgharibi, B. Baum, P. Recho, A. J. Kabla, and G. T. Charras. Actomyosin Controls Planarity and Folding of Epithelia in Response to Compression. *Nature Materials* **19**, 109 (2020).
- T. P. J. Wyatt, A. R. Harris, M. Lam, Q. Cheng, J. Bellis, A. Dimitracopoulos, A. J. Kabla, G. T. Charras, and B. Baum. Emergence of Homeostatic Epithelial Packing and Stress Dissipation through Divisions Oriented along the Long Cell Axis. *Proceedings of the National Academy of Sciences* **112**, 5726 (2015).
- W. Xi, T. B. Saw, D. Delacour, C. T. Lim, and B. Ladoux. Material Approaches to Active Tissue Mechanics. *Nature Reviews Materials* **4**, 23 (2018).
- T. Yeung, P. C. Georges, L. A. Flanagan, B. Marg, M. Ortiz, M. Funaki, N. Zahir, W. Ming, V. Weaver, and P. A. Janmey. Effects of Substrate Stiffness on Cell Morphology, Cytoskeletal Structure, and Adhesion. *Cell Motility* **60**, 24 (2005).
- H. G. Yevick, P. W. Miller, J. Dunkel, and A. C. Martin. Structural Redundancy in Supracellular Actomyosin Networks Enables Robust Tissue Folding. *Developmental Cell* **50**, 586 (2019).

- J. C. Yu and R. Fernandez-Gonzalez. Local Mechanical Forces Promote Polarized Junctional Assembly and Axis Elongation in Drosophila. *eLife* **5**, e10757 (2016).
- F. Zampieri, M. Coen, and G. Gabbiani. The Prehistory of the Cytoskeleton Concept. *Cytoskeleton* **71**, 464 (2014).
- L. Zhang, Y. Xiang, H. Zhang, L. Cheng, X. Mao, N. An, L. Zhang, J. Zhou, L. Deng, Y. Zhang, X. Sun, H. A. Santos, and W. Cui. A Biomimetic 3D-Self-Forming Approach for Microvascular Scaffolds. *Advanced Science* **7**, 1903553 (2020).

“... If you want knowledge, you must take part in the practice of changing reality. If you want to know the taste of a pear, you must change the pear by eating it yourself...”

毛泽东

